AN ABSTRACT OF THE THESIS OF

Kunal H. Kate for the degree of Master of Science in Material Science presented on December 13, 2012.

Title: Models for Predicting Powder-Polymer Properties and Their Use in Injection Molding Simulations of Aluminum Nitride.

Abstract approved:

_____

Sundar V. Atre

Powder injection molding (PIM) is widely used to manufacture complex-shaped ceramic and metal components in high production volumes. In order to design and fabricate PIM components, it is important to know a number of material properties at different powder-polymer compositions. In this thesis, several predictive models for estimating rheological, thermal and mechanical properties as a function of powder-polymer mixtures were evaluated using experimental data obtained from the literature. Based on this survey, models were selected for predicting rheological, thermal and mechanical properties for aluminum nitride-polymer mixtures at various volume fractions of powder using experimental measurements of unfilled and filled polymers. The material properties were estimated for two aluminum nitride powder-polymer mixtures and used in mold-filling simulations. These results will provide new perspectives and design tools for identifying useful material compositions, component geometry attributes, and process parameters while eliminating expensive and time-consuming trial-and-error practices prevalent in PIM.

Models for Predicting Powder-Polymer Properties and Their Use in Injection Molding Simulations of Aluminum Nitride

by.

Kunal H. Kate

A THESIS

submitted to

Oregon State University

in partial fulfillment of
the requirements for the
degree of

Master of Science

Presented December 13, 2012
Commencement June 2013

Master of Science thesis of Kunal H. Kate presented on December 13, 2012.

APPROVED:

Major Professor, representing Material Science

Director of the Material Science Program

Dean of the Graduate School

I understand that my thesis will become part of the permanent collection of Oregon State University libraries. My signature below authorizes release of my thesis to any reader upon request.

_____

Kunal H. Kate, Author

ACKNOWLEDGEMENTS

I would like to acknowledge the endless amount of help I received from my advising professor Sundar V. Atre for the patient guidance, encouragement and advice he has provided throughout my time as his student. I have been extremely lucky to have a supervisor who cared so much about my work, and who responded to my questions and queries so promptly. This work would have not been possible without the guidance, inputs and comments I received from Dr. Ravi K. Enneti of Global Tungsten Powder throughout my research.

I am very thankful to Dr. John Simonsen for guiding me through the use of torque rheometry and for his support to my research. I would like to thank Dr. Skip Rochefort in allowing me to use his laboratory and in helping me better understand rheological properties, which played an important role in this research. In addition I would like to thank Dr. Valmikanathan Onbattuvelli, Dr. Seong Jin Park and Dr. Randall M. German with their invaluable guidance throughout the research.

Finally, I thank my lab mates Renee Martin and Juergen Lenz for their constant support and fruitful discussions I have had with them.

CONTRIBUTION BY AUTHORS

I was involved in design, data collection, writing and interpretation of data for Chapters 2 Chapter 3 and Chapter 4. Dr. Sundar V. Atre and Dr. Ravi K. Enneti were also involved in design data collection, interpretation and writing of Chapter 2, Chapter 3 and Chapter 4. Dr. Valmikanathan P. Onbattuvelli, Dr. Seong Jin Park and Dr. Randall M. German assisted in the interpretation of the data.

TABLE OF CONTENTS

Page

1. Introduction....1

2. Predicting Powder-Polymer Mixture Properties for PIM Design....4

2.1. Abstract....4
2.1. Introduction....5
2.3. Experimental Methods....9
2.4. Estimating Properties of Powder-Polymer Mixtures:....9
2.4.1 Density....9
2.4.2 Specific heat....12
2.4.3 Thermal conductivity....16
2.4.4 Coefficient of thermal expansion....18
2.4.5. Elastic and shear modulus....22
2.4.6 Viscosity....28
2.4.8 Specific volume....33
2.5. Conclusions....39
2.6. References....39

3. Measurements of Powder-Polymer Mixture Properties and Their Use in Powder Injection Molding Simulations for Aluminum Nitride....49

3.1 Abstract....49
3.2 Introduction....50
3.3 Experimental Materials and Methods....52
3.4 Estimating Properties of Powder-Polymer Mixtures:....54
3.4.1 Density....54
3.4.2 Specific heat....55
3.4.3 Thermal conductivity....56
3.4.4 Coefficient of thermal expansion....57
3.4.5 Elastic and shear modulus....58
3.4.6 Viscosity....59

TABLE OF CONTENTS (Continued)

Page

3.4.7 Specific volume 62
3.5 Simulation Results 65
3.6 Conclusions 71
3.7 References 71
4. Feedstock Properties And Injection Molding Simulations Of Bimodal Mixtures of Nanoscale and Microscale Aluminum Nitride 74
4.1 Abstract 74
4.2 Introduction 75
4.3 Experimental Materials and Methods 78
4.4 Results and Discussion 80
4.4.1 Properties 80
4.4.2 Simulation Results 92
4.5. Conclusions 99
4.6. References 100
5. Conclusions and Future Work 104
5.1 Conclusions 104
5.2 Future Work 105
5. Bibliography 107
6. Appendices 116
Appendix A1: Properties of Monomodal μ-AlN Feedstock 117
Appendix A2: Properties of Bimodal μ-n AlN Feedstock 124
Appendix A3: Properties of The Multi-Component Binder Mixture Feedstock 132
Appendix B: Procedures for Viscosity Calculations 140
Appendix C: Procedures for PVT Calculations 149
Appendix D: Procedures for Calculations of Coefficient of Determination 157

TABLE OF CONTENTS (Continued)

Page

Appendix E- Procedures for Mold Flow Simulations 162

LIST OF FIGURES

Figure Page

Figure 2.1: Common mold filling defects found in PIM: (A) jetting, (B) short shot, (C) powder-binder separation, and (D) flashing. Models for predicting mixture properties can be used to perform mold-filling simulations that can help select the correct combinations of powders and polymers to be used to fabricate a desired geometry, early during the design cycle. 7

Figure 2.2: Variation in density as a function of filler content for 3 polymer-powder mixtures: PTFE-TiO_2, PTFE-$BaPr_2Ti_4O_{12}$, and PTFE-$BaSm_2Ti_4O_{12}$, based on the experimental data obtained from Rajesh et al [11]. The lines represent predicted values based on Equation 2.1. 12

Figure 2.3a: Variation in specific heat as a function of filler content for 5 polymer-powder mixtures: PW-Fe, PP-Al, PP-Cu, PP-glass and PP-$BaSO_4$, based on the experimental data obtained from German et al [1], Boudenne et al [8] and Weidenfeller et al [13]. The lines represent predicted values based on Equation 2.3. 15

Figure 2.3b: Variation in specific heat as a function of filler content for PP-Al polymer-powder mixtures based on the experimental data obtained from Weidenfeller et al [13]. The lines represent predicted values using Equations 2.3-2.5 15

Figure 2.4a: Variation in thermal conductivity as a function of filler content for three polymer-powder mixtures: HDPE-BN, HDPE-SiC and PVDF-Al, based on the experimental data obtained from Lee et al [19] and Xu et al [38]. The lines represent predicted values based on Equation 2.10. 19

Figure 2.4b: Variation in thermal conductivity as a function of filler content for HDPE-BN polymer-powder mixtures based on experimental data obtained from Lee et al [19]. The lines show predicted values based on Equations 2.6-2.10. 19

Figure 2.5a: Variation in thermal expansion coefficient as a function of filler content for polymer-powder mixtures: epoxy/Al_2O_3 and PTFE/$Sr_2Ce_2Ti_5O_{16}$ and epoxy/SiO_2, based on the experimental data obtained from Brassell et al [2], Feltham et al [20], McGrath et al [39], and Subodh et al [40]. The lines represent predicted values based on Equation 2.11. 23

Figure 2.5b: Variation in thermal expansion coefficient as a function of filler content for epoxy/SiO_2 based on the experimental and predicted data obtained from Feltham et al [20]. The lines represent predicted values based on Equations 2.11-2.15. 23

Figure 2.6a: Variation in elastic modulus as a function of filler content for 3 polymer-powder mixtures: PLA-hydroxyapatite, epoxy-borosilicate glass and CE-silica based on the experimental data obtained from Balac et al [35], Wu et al [36] and Wooster et al [37]. The lines show the predicted values based on Equation 2.16. 26

LIST OF FIGURES (Continued)

Figure Page

Figure 2.6b: Variation in elastic modulus as a function of filler content for 3 polymer-powder mixtures: PLA-hydroxyapatite, epoxy-borosilicate glass and CE-silica based on the experimental data obtained from Wooster et al [17], Balac et al [21], and Wu et al [22]. The lines represent predicted values based on Equation 2.16.....26

Figure 2.7a: Variation in viscosity as a function of filler content for 3 polymer-powder mixtures: LDPE-Al_2O_3, PB-Al and PB-NH_4ClO_4, based on the experimental data obtained from Zhang et al [27], Arefinia et al [29], and Osman et al [41]. The lines represent predicted values based on Equation 2.28. 31

Figure 2.7b: Variation in viscosity as a function of filler content for LDPE-Al_2O_3, based on the experimental data obtained from Zhang et al [27]. The lines show predicted values based on Equations 25-28. 31

Figure 2.8: Comparison of viscosity with shear rate at 413 K (top) and 433 K (bottom) for different volume fractions of AlN powder, ϕ_p [31]. 33

Figure 2.9: Variation in specific volume as a function of filler content for PP-Al mixtures, based on the experimental data obtained from Boudenne et al [8]. The lines show predicted values based on Equation 2.31.....35

Figure 2.10: PVT behavior for 0 and100 MPa pressures for different volume fractions of AlN powder, ϕ_p [31]. 36

Figure 3.1: Dependence of linear shrinkage on final sintered density and different volume fractions of powder, ϕ_p , using Equation 3.1. 51

Figure 3.2: SEM image of AlN powder used in this study.....52

Figure 3.3: Comparison of viscosity with shear rate at 413 K (top) and 433 K (bottom) for different volume fractions of AlN powder, ϕ_p. 61

Figure 3.4: PVT behavior for 0, 100, and 200 MPa pressures for different volume fractions of AlN powder, ϕ_p. 64

Figure 3.5: Mold geometry used in injection molding simulations: a) simple heat-sink substrate without fins, and b) heat sink substrate with fins. 65

Figure 3.6A: Progressive filling of the heat sink substrate without fins shown in Figure 5A for 0.51 volume fraction AlN feedstock: (a) 25% fill, (b) 50% fill, (c): 75% fill and (d) 100% fill.....66

LIST OF FIGURES (Continued)

Figure Page

Figure 3.6B: Progressive filling of the heat sink substrate with fins shown in Figure 5B for 0.51 volume fraction AlN feedstock: (a) 25% fill, (b) 50% fill, (c): 75% fill and (d) 100% fill. 66

Figure 3.8: Freeze time for different volume fractions of AlN powder, ϕ_p. 68

Figure 3.9: Peak injection pressure for different volume fractions of AlN powder, ϕ_p.....69

Figure 3.10: Volumetric shrinkage (%) for different volume fractions of AlN powder, ϕ_p. 69

Figure 3.11: Weld-line distribution in the heat-sink geometries without fins (top) and with fins (bottom), at 0.48(a and c) and 0.52 (b and d) volume fractions of AlN powder, ϕ_p...70

Figure 4.1: Dependence of linear shrinkage on final sintered density and different volume fractions of powder, ϕ_p, using Equation 1. 76

Figure 4.2: SEM of bimodal μ-n AlN powder used in the present study. 78

Figure 4.3 shows the shear-rate dependence of viscosity for bimodal μ-n AlN at 413 and 433 K. 83

Figure 4.4: PVT behavior for 0, 100, and 200 MPa pressures for different volume fractions of bimodal μ-n AlN powder. 87

Figure 4.5: Mold geometry used in injection molding simulations: a) simple heat-sink substrate without fins, and b) heat sink substrate with fins. 93

Figure 4.6A: Progressive filling of the heat sink substrate without fins shown in Figure 5A for 0.60 volume fraction bimodal μ-n AlN feedstock: (a) 25% fill, (b) 50% fill, (c): 75% fill and (d) 100% fill.....93

Figure 4.6B: Progressive filling of the heat sink substrate with fins shown in Figure 5B for 0.60 volume fraction bimodal μ-n AlN feedstock: (a) 25% fill, (b) 50% fill, (c): 75% fill and (d) 100% fill 94

Figure 4.7: Part weight for different volume fractions of bimodal μ-n AlN powder. 95

Figure 4.8: Freeze time for different volume fractions of bimodal μ-n AlN powder.....95

Figure 4.9: Peak injection pressure for different volume fractions of bimodal μ-n AlN powder. 96

LIST OF FIGURES (Continued)

Figure Page

Figure 4.10: Variation of clamp force for different volume fractions of bimodal μ-n AlN powder. 97

Figure 4.11: Simulation results of weld lines at 0.52 volume fractions (top) and 0.6 volume fractions (bottom) bimodal μ-n AlN powder for heat sink geometry with and without fin.....98

LIST OF TABLES

Table Page

Table 2.1. Characteristics of an ideal binder system for metal injection molding process [1].....6

Table 2.2. Test equipment and standards used for measuring critical properties of feedstocks 10

Table 2.3. Literature studies on the density of polymer-powder mixtures.....11

Table 2.4. Literature studies on the specific heat of polymer-powder mixtures 13

Table 2.5. Literature studies on the thermal conductivity of polymer-powder mixtures ..17

Table 2.6. Literature studies on the coefficient of thermal expansion of polymer-powder mixtures 20

Table 2.7. Literature studies on the elastic modulus of polymer-powder mixtures 25

Table 2.8. Literature studies on the viscosity of polymer-powder mixtures 29

Table 2.9. Literature studies on the PvT behavior of polymer-powder mixtures.....34

Table 3.1: Comparison of melt and solid densities for different volume fractions of AlN powder, ϕ_p. 55

Table 3.2: Specific heat capacity values at various temperatures for different volume fractions of AlN powder, ϕ_p. 56

Table 3.3: Thermal conductivity for different volume fractions of AlN powder, ϕ_p. 57

Table 3.4: Coefficient of thermal expansion for different volume fractions of AlN powder, ϕ_p. 58

Table 3.5: Elastic and shear modulus values for different volume fractions of AlN powder, ϕ_p. 58

Table 3.6: Cross-WLF constants for different volume fractions of AlN powder, ϕ_p. 60

Table 3.7: Dual-domain Tait constants for different volume fractions of AlN powder, ϕ_p. 63

Table 4.1: Models used in the present study to estimate the feedstock properties. 81

Table 4.2: Descriptions of the symbols used in empirical relations presented in Table 4.1. 82

LIST OF TABLES (Continued)

Table Page

Table 4.3: Cross-WLF constants for different volume fractions of bimodal μ-n AlN powders. 83

Table 4.4: Dual-domain Tait constants for different volume fractions of bimodal μ-n AlN powders. 86

Table 4.5: Comparison of melt and solid densities for different volume fractions of bimodal μ-n AlN powders. 88

Table 4.6: Specific heat capacity values at various temperatures for different volume fractions of bimodal μ-n AlN powders. 89

Table 4.7: Thermal conductivity for different volume fractions of bimodal μ-n AlN powder. 90

Table 4.8: Coefficient of thermal expansion for different volume fractions of bimodal μ-n AlN powder. 91

Table 4.9: Elastic and shear modulus values for different volume fractions of bimodal μ-n AlN powder. 92

LIST OF APPENDIX FIGURES

Figure Page

Figure B.1. Comparison of experimental* and predicted values of viscosity as a function of shear rate. 144

Figure B.2. Solver parameter window in Microsoft Excel 2010. 146

Figure B.3. Selection of solving method and input parameters for calculating n and τ*. 147

Figure B.4. Set convergence value for GRG Nonlinear method. 147

Figure C.1. Specific volume as a function of temperature at 50 MPa pressure. 150

Figure C.2. Volumetric transition temperature as a function of pressure. 151

Figure C.3. Specific volume as a function of temperature for 0.48 volume fraction AlN at 0 MPa pressure. 152

Figure C.4. Solver parameter window in Microsoft Excel 2010. 154

Figure C.5. Selection of solving method and input parameters for calculating b_{3m}, and b_{4m}. 155

Figure C.6. Set convergence value for GRG Nonlinear method. 155

Figure D.1. Solver parameter window in Microsoft Excel 2010. 159

Figure D.2. Selection of solving method and input parameters for calculating ρ_p and ρ_b. 160

Figure D.3. Set convergence value for GRG Nonlinear method. 160

Figure E.1: Mold geometry used in injection molding simulations: a) simple heat-sink substrate without fins, and b) heat sink substrate with fins. 162

Figure E.2. Selecting heat sink geometry for injection molding simulation 163

Figure E.3. Selection from the type of meshes types. 163

Figure E.4. Creating a new project. 163

Figure E.5. Typical layout of Moldflow Insight software after creating a new project. 164

Figure E.6. Generating mesh wizard. 164

Figure E.7. Mesh repair wizard. 165

Figure E.8. Selection of analysis sequence. 165

LIST OF APPENDIX FIGURES (Continued)

Figure Page

Figure E.9. Material selection process. 166

Figure E. 10. Process setting wizard. 166

LIST OF APPENDIX TABLES

Table Page

Table A.1 Feedstock composition of μ- AlN Feedstock. 117

Table A.2 Feedstock composition of μ-n AlN Feedstock 124

Table A.3 Feedstock composition of μ-n AlN Feedstock 132

Table B.1: Experimental values of Cross-WLF coefficients.....140

Table B.2: Calculation of zero shear viscosity for matrix and 0.52 volume fraction of AlN at different shear rates.....141

Table B.3: Calculation of viscosity for matrix and 0.52 volume fraction of AlN for different shear rates and at 413 K.....141

Table B.4: Calculation of maximum volume fraction for each individual temperature at different shear rates.....142

Table B.5: Calculation of viscosity at different shear rates for 413 K using floating ϕ_{max} and Equation B.1 143

Table B.6. Sum of square of difference method for 0.48 volume fractions AlN at 413 K to calculate η_0, n, and τ^* 145

Table B.7. Sum of square of difference method for 0.48 volume fractions AlN at 413 K to calculate D1, A1 and T* 148

Table C.1: Specific volume calculations for different solids loading at 50 MPa pressure. 149

Table C.2. Calculation of Tait constants with the use of SSD and a GRG nonlinear solver. 153

Table D.1. Calculation of R^2 for density values using experimental data from Rajesh et al [1].....157

I dedicate this thesis to

my parents Hemant and Netra Kate who have supported me all the way since the beginning of my studies. Also this thesis is dedicated to Dr. Pawan Khanna for guiding and inspiring me to conduct research.

Models for Predicting Powder-Polymer Properties and Their Use in Injection Molding Simulations of Aluminum Nitride

Chapter 1

Introduction

Powder injection molding (PIM) is useful to economically net-shape complex ceramic and metal components at high production volumes. Complex shapes manufactured using PIM have applications in wide area, for instance medicine, electronics and power generators as shown **Figure 1.1**. In PIM, ceramic or metal powder is compounded with polymer (binder) and used to mold parts with an injection-molding machine, in a manner analogous to the fabrication of conventional thermoplastics. Subsequently, the polymer is removed (debinding) from the molded part and then sintered under controlled time, temperature and atmospheric conditions to get the final part of desired dimensions, density, microstructure and properties.

(A) (B) (C)

Figure 1.1: Complex shapes manufactured by PIM: (A) stainless steel dental implants [1], (B) aluminum heatsinks substrates for light emitting diodes [2], (C) silicon nitride rotors for gas turbine engine [3].

Due to the requirement for several subsequent processing steps after injection molding, it is essential to identify appropriate powder-binder (feedstock) compositions and processing conditions that will result in obtaining parts that are free of defects such as weld-lines, internal stresses, cracks and warpage during the injection molding stage. The optimal amount of binder depends on the particle packing, since filling all of the void space between the particles is necessary to maintain a low viscosity. Thus, factors like the particle size distribution and particle shape influence the optimal binder concentration.

The ratio of powder to binder also depends on the part geometry, process conditions and mold design. When the filler content in the powder-polymer composite is varied a change in the material properties is observed. Many researchers have tried to proposed models to predict material properties of polymer composites at different volume fractions of particulate fillers. As it is not always practical to experimentally obtain the values of these material properties due to time and resource constraints, it is convenient to estimate material properties using various predictive models. The present thesis evaluates predictive models for estimating mixture properties as a function of filler content in the feedstock. The properties were subsequently used to perform mold-filling simulations that help select the correct combinations of powders and polymers to be used to fabricate a desired geometry, early during the PIM design cycle. It is anticipated that these results will provide new perspectives and design tools for identifying useful material compositions, component geometry attributes, and process parameters while eliminating expensive and time-consuming trial-and-error practices prevalent in PIM.

Chapter 2 of the thesis reviews and compares several models for predicting the compositional dependence of thermal, rheological and mechanical properties using experimental data for several powder-polymer mixtures obtained from the literature. In order to minimize the time and expense required to experimentally measure these material properties over a range of compositions, a strategy to predict material properties from a limited number of experiments was evaluated. Using experimentally available literature data, curve fitting of various predictive models was carried out and coefficients of determination were calculated to identify the most suitable predictive models. The literature review presented in the **Chapter 2** has been submitted to *International Materials Reviews*.

Chapter 3 presents the use of predictive models identified in the literature review in **Chapter 2** to estimate a number of physical properties over a range of powder volume fractions for an aluminum nitride feedstock containing a monomodal distribution of sub-micron particles. The predicted properties were used to conduct injection-molding

simulations using the Autodesk Moldflow Insight software. Two heat sink geometries were designed and the simulation results were used to understand the sensitivity of feedstock composition on the injection-molding behavior and defect evolution in aluminum nitride components**.** **Chapter 3** has been published in *JOM* and is currently ranked among the five most-read articles published in this journal in 2012.

Chapter 4 presents the use of predictive models identified in **Chapter 2** to estimate a number of physical properties over a range of powder volume fractions for an aluminum nitride feedstock containing a bimodal distribution of nanoscale and sub-micron particles. The addition of nanoparticles provides a useful route to increase the maximum packing density of powders in the feedstock. The results provide a comparison of the mold filling behavior and defect evolution in the monomodal and bimodal feedstocks as a function of filler content. A research article based on this chapter has been submitted to *Ceramics International* and is currently under editorial review.

Appendix A contains the raw experimental data on the feedstock and binder properties used in conjunction with predictive models for obtaining the results in **Chapters 3** and **4**. **Appendices B, C,** and **D** summarize detailed procedures for model calculations and extraction of curve-fitting parameters. **Appendix E** summarizes procedures for conducting mold-filling simulations using the Autodesk Moldflow Insight software platform.

References

[1] www.wisegeek.com

[2] www.ledcoolers.com

[3] www.kyocera.com

Chapter 2

Predicting Powder-Polymer Mixture Properties for PIM Design

2.1. Abstract

Powder injection molding (PIM) is a high-volume manufacturing technique for fabricating ceramic and metal components that have complex shapes. In PIM design, it is important to know the injection molding behavior at different powder-polymer compositions so as to understand the trade-offs between ease-of-fabrication, process throughput, and part quality at the design stage. A limited database of materials properties at different powder-polymer compositions is a significant challenge that needs to be addressed in order to conduct accurate computer simulations that aid part and mold design in PIM. However, accurate material property measurements can be expensive and time-consuming. In order to resolve these conflicting challenges it is hypothesized that experimental measurements of material properties of a filled polymer at a specific filler content combined with similar measurements of unfilled polymer will be adequate to estimate the dependence of properties on filler content using rule-of-mixture models. To this end, this paper focuses on a literature review of experimental data obtained from measurements of rheological, thermal and mechanical properties for a wide range of powder-polymer mixtures at various filler volume fractions. The experimental data were compared to computed properties using various predictive models. It is anticipated that the current review can be valuable in selecting appropriate predictive models for estimating properties based on the input data requirements for commercially available mold-filling simulation platforms such as Moldflow. The combined protocol can be used to design new materials and component geometries as well as optimize process parameters while eliminating expensive and time-consuming trial-and-error practices prevalent in PIM.

2.1. Introduction

Powder injection molding (PIM) is useful to economically net-shape complex ceramic and metal components at high production volumes. In PIM, ceramic or metal powder is compounded with polymer (binder) and used to mold parts with an injection-molding machine, in a manner analogous to the fabrication of conventional thermoplastics. Subsequently, the polymer is removed (debinding) from the molded part and then sintered under controlled time, temperature and atmospheric conditions to get the final part of desired dimensions, density, microstructure and properties.

Binders play a very crucial role in processing of components by PIM. A binder consists of primary polymer component to which various additives like dispersants, stabilizers, and plasticizers are added. The basic purpose of binders is to assist in shaping of the component during injection molding and to provide strength to the shaped component. Binders act as a medium for shaping and holding the metal particles together till the onset of sintering. The important characteristics of binders are summarized in **Table 2.1**.

Binders are mixed with ceramic or metal powders to make feedstocks that are further used as starting materials for injection molding. Due to the requirement for several subsequent processing steps after injection molding, it is essential to identify appropriate feedstock (powder-binder) compositions and processing conditions that will result in obtaining parts that are free of defects such as weld-lines, internal stresses, cracks and warpage during the injection molding stage. **Figure 2.1** provides examples of some common molding defects. A successful PIM feedstock represents a balanced mixture of powder and binder. Three possible situations can be generalized in considering the ratio of powder to binder in the feedstock. Too little binder results in a loss of homogeneity and trapped air pockets resulting in molding difficulties. Raising the binder concentration results in lowering the viscosity as the mixture adopts a more fluid-like consistency. The critical solids loading is the composition where the particles are packed as tightly as possible without external pressure and all space between the particles is filled with binder. With any more powder (less binder) there is insufficient binder to prevent voids

and molding defects. During debinding, voids contribute to cracking, so a deficiency of binder is unacceptable.

Table 2.1. Characteristics of an ideal binder system for metal injection molding process [1].

Criterion	Desirable characteristic
Powder interaction	low contact angle good adhesion with powder capillary attraction of particles chemically passive with respect to powder
Flow characteristics	low viscosity at the molding temperature low viscosity change during molding increase in viscosity on cooling small molecule to fit between particles
Debinding	degradation temperature above molding and mixing temperatures multiple components with progressive decomposition temperatures and variable properties low residual carbon content after burnout non corrosive and non toxic burnout products
Manufacturing	easily available and inexpensive long shelf life safe and environmentally acceptable not degraded due to cyclic heating high strength and stiffness high thermal conductivity low thermal expansion coefficient soluble in common solvents high lubricity short chain length and no orientation

However, a large excess of binder is unacceptable. Excess binder separates from the powder in molding, leading to flashing (a thin layer of binder between the die pieces) or inhomogeneities in the molded component. Further, a large excess of binder leads to component slumping during debinding, since the particles are not held in place as binder is removed. The critical solids loading corresponds to the particles in point contact, with no voids in the binder.

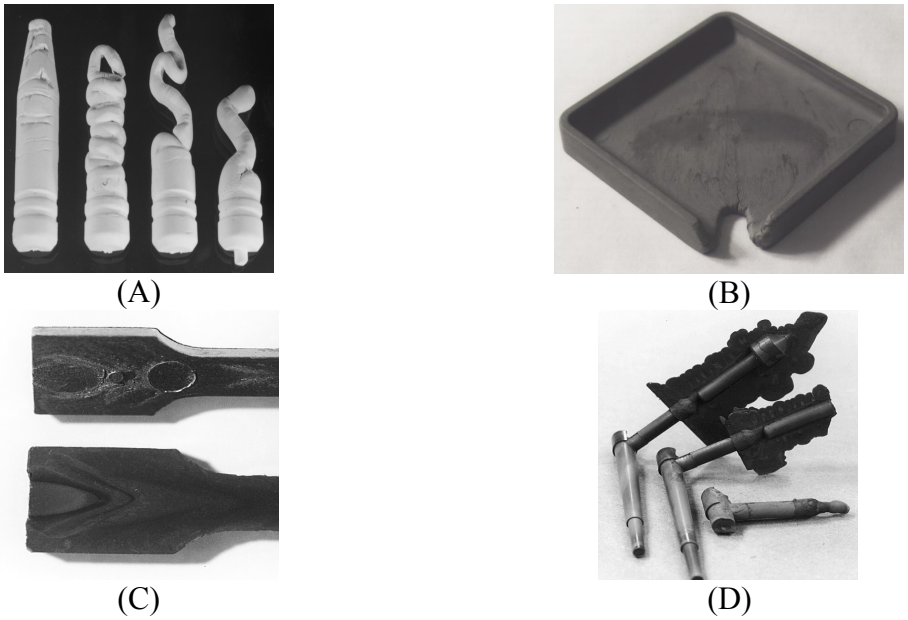

Figure 2.1: Common mold filling defects found in PIM: (A) jetting, (B) short shot, (C) powder-binder separation, and (D) flashing. Models for predicting mixture properties can be used to perform mold-filling simulations that can help select the correct combinations of powders and polymers to be used to fabricate a desired geometry, early during the design cycle.

Molding is usually performed at a solids loading with slightly more binder than that measured at the critical level. At this point the feedstock has sufficiently low viscosity that it can be molded, but exhibits good particle-particle contact to ensure shape preservation during processing. The slight excess of binder over that at the critical solids loading improves the mold-filling behavior. The amount of binder depends on the particle packing, since filling all of the void space between the particles is necessary to maintain a low viscosity. Thus, factors like the particle size distribution and particle shape influence

the optimal binder concentration. The ratio of powder to binder also depends on the part geometry, process conditions and mold design. When the filler content in the powder-polymer composite is varied a change in the material properties is observed [1]. These material properties when measured experimentally help in quantifying material behavior at different volume fractions of powder. Many researchers have tried to put forth mixing rules to predict material properties at different volume fractions of powders [2–9]. As it is not always practical to experimentally obtain the values of these material properties due to time and resource constraints, it is convenient to estimate material properties using various predictive models. The models for predicting mixture properties can subsequently be used to perform mold-filling simulations that can help select the correct combinations of powders and polymers to be used to fabricate a desired geometry, early during the design cycle.

Rules-of-mixtures (ROM) can be used to estimate powder-polymer material property based on assumption that a material property is weighted or volume averaged with matrix or dispersed phases as the basis [10]. The binder (polymer) is considered as matrix phase whereas, filler (powder) as dispersed phase in the powder-polymer composite. Thermal, rheological and mechanical properties can be estimated using ROM, but each of these material properties has a number of ROM associated with it [3], [8], [10]. In order to generalize a particular rule of mixture for a specific material property it is necessary to assess the relative accuracy with which it can estimate the material property. Further, their applicability over the range of powder volume fractions of relevance to PIM need to be studied for different material compositions.

Experimental data that are typically required for powder-polymer mixtures at high volume fractions of powder are limited in the literature and also tend to be expensive to obtain for specific volume fractions of powder. In the present review, empirical models to predict feedstock properties over a compositional range were reviewed and compared with literature data on powder-polymer mixtures. Feedstock properties necessary for performing mold-filling simulations were selected for the present review. It is

anticipated that the experimental techniques and modeling evaluated in this review can be generalized to design new materials, eliminating expensive and time-consuming trial and-error practices prevalent in PIM.

2.3. Experimental Methods

The rheological and thermal properties of a PIM feedstock play a crucial role in the design of parts, mold cavities and process settings. For example the variation of viscosity with shear rate and temperature is useful to analyze the mold filling behavior of the feedstock material. Similarly knowledge of the heat capacity, thermal conductivity and coefficient of thermal expansion of the feedstock is critical to eliminate warpage, weld-lines and shrinkage cracks during solidification and cooling of the component. The degradation properties of the feedstock are critical in developing thermal cycles for successful removal of binders from the injection-molded part. Experimental techniques and standards have been developed to measure these critical properties of a PIM feedstock. A summary of the experimental techniques used for measuring the properties of a PIM feedstock is detailed in **Table 2.2**.

2.4. Estimating Properties of Powder-Polymer Mixtures:

Experimentally determined physical properties of powder-polymer mixtures over a range of volume or weight fractions were compiled from prior studies and compared to properties estimated from various powder-polymer mixture models that have been reported in the literature.

2.4.1 Density

An important difference between plastics injection molding and powder injection molding is the density of the molding material. The optimal filler content in a PIM feedstock depends on differences in polymer attributes, particle size distribution, particle shape, and mixture homogeneity. Accordingly there is a crucial need for process flexibility owing to lot-to-lot variations in powders and binders.

Table 2.2. Test equipment and standards used for measuring critical properties of feedstocks

Property	Equipment	Standard
Rheology (viscosity-shear rate-temperature)	Capillary rheometer, cone and plate rheometer	ASTM D3835
Specific heat	Differential scanning calorimeter (DSC)	ASTM E1269
Melting	Differential scanning calorimeter (DSC)	ASTM D3418
Solidification	Differential scanning calorimeter (DSC)	ASTM D7426
Burnout characteristics	Thermogravimetric analysis (TGA)	ASTM E1131, ASTM E1641
Thermal conductivity	Line source method	ASTM D5930
Pressure-volume-temperature (PvT)	High pressure dilatometer	ASTM D792
Coefficient of thermal expansion	Thermomechanical analyzer (TMA)	ASTM E831
Elastic modulus and Poisson's ratio	Universal testing machine (UTM)	ASTM D638

Small errors in formulating a feedstock cause molding sensitivities because of the rapid viscosity change with solids loading. Since the viscosity of a mixture changes most rapidly with composition near the critical loading, small errors are amplified into large viscosity shifts. The density of a powder-polymer mixture is an important experimental descriptor of the composition of a feedstock.

Several examples of literature reports on experimental measurements of density are summarized in **Table 2.3**. The melt and solid density of powder-polymer mixtures can be estimated using an inverse rule-of-mixtures [3], [4], [10] as given in **Equation 2.1:**

$$\frac{1}{\rho_c} = \frac{X_p}{\rho_p} + \frac{X_b}{\rho_b} \quad (2.1)$$

where, ρ is the density, X is the mass fraction and the subscripts c, b and p stand for the composite, binder and powder respectively.

Table 2.3. Literature studies on the density of polymer-powder mixtures

Ref. No.	Authors	Filler	Median Particle Size of Filler, µm	Matrix	Composition Range
[8]	Boudenne et al	Al	5	PP	10-60 wt.%
[11]	Rajesh et al	TiO_2	4	PTFE	52–72 wt.%
[11]	Rajesh et al	$BaPr_2Ti_4O_{12}$	4	PTFE	52–72 wt.%
[11]	Rajesh et al	$BaSm_2Ti_4O_{12}$	4	PTFE	52–72 wt.%
[42]	Goyal et al	n-Al_2O_3	0.04	PEEK	0-12 vol.%

PP: polypropylene; PTFE: polytetrafluoroethylene; PEEK: polyether ether ketone

Although for manufacturing purposes feedstock formulation is represented by weight, volumetric comparisons are often useful when examining powders of differing densities. The volumetric fractions for powder and binder can be calculated from the mass fraction using **Equation 2:**

$$\phi_p = \frac{\frac{X_p}{\rho_p}}{\frac{X_p}{\rho_p} + \frac{X_b}{\rho_b}} \qquad \phi_b = \frac{\frac{X_b}{\rho_b}}{\frac{X_p}{\rho_p} + \frac{X_b}{\rho_b}} \quad (2.2)$$

where, ϕ_p and ϕ_b are the volume fractions of the powder and binder, respectively.

Experimental data of the density of three powder-polymer mixtures with 50-70 wt.% filler content were obtained from the literature [11] and compared with **Equation 2.1** as shown in **Figure 2.2.** A coefficient of determination (R^2) value exceeding 0.97 indicates the applicability of the model to predict density in highly filled mixtures.

Density versus composition experiments allows determination of the critical solids loading of a feedstock. At this point, the measured density departs from that calculated

using **Equation 2.1**. At high binder concentrations, the experimental mixture density typically follows along the predicted density line. For the pure powder, the particles do not pack to full density. Accordingly, at an intermediate composition the mixture density breaks away from the theoretical line at the critical solids loading; the particles are in their closest packing condition and just enough binder exists to fill the voids between the particles. Differences between the powder packing characteristics determine the critical solids loading. Departures from ideal behavior are also indicative of deficiencies in mixture homogeneity and formation of voids.

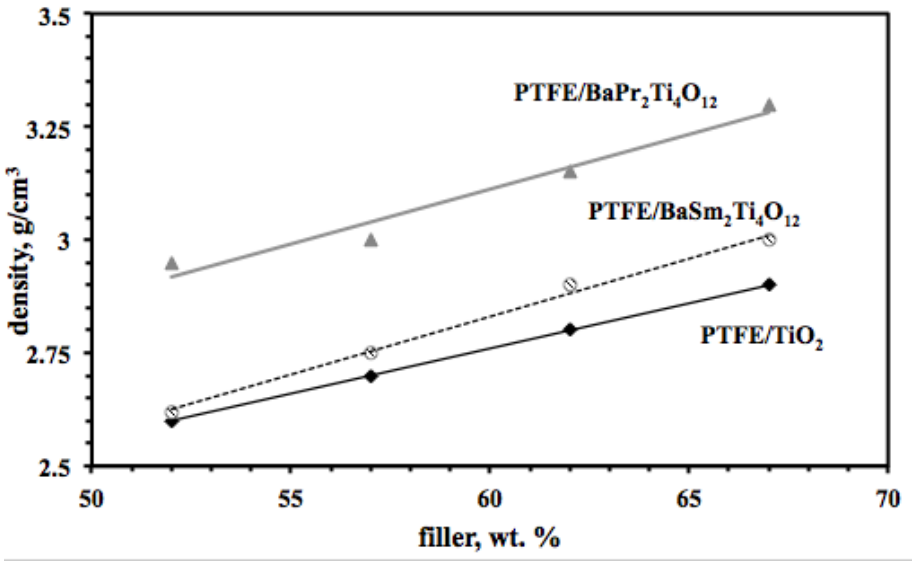

Figure 2.2: Variation in density as a function of filler content for 3 polymer-powder mixtures: PTFE-TiO_2, PTFE-$BaPr_2Ti_4O_{12}$, and PTFE-$BaSm_2Ti_4O_{12}$, based on the experimental data obtained from Rajesh et al [11]. The lines represent predicted values based on Equation 2.1.

2.4.2 Specific heat

The heat capacity of polymers and their mixtures with powders is a complex function of temperature. At temperatures near the melting point, the heat capacity changes drastically as a result of the phase change. Further, a PIM feedstock typically contains multiple binder components, therefore multiple transitions are usually observed. Accordingly,

specific heat data is required over the range of processing temperatures in order to accurately model the heat transfer of the molten feedstock entering the mold cavity.

Table 2.4 summarizes the experimental data of specific heat for a wide range of compositions for several powder-polymer mixtures that have been reported in the literature. The simplest rule-of-mixture model used for predicting specific heat based on the general rule-of-mixtures [10] is shown in **Equation 2.3.**

$$C_{p_c} = \left[C_{p_b} X_b + C_{p_p} X_p\right] \tag{3}$$

where, C_p is the specific heat, X is the mass fraction and the subscripts c, b and p stand for the composite, binder and powder respectively.

Table 2.4. Literature studies on the specific heat of polymer-powder mixtures

Ref. No.	Authors	Filler	Median Particle Size of Filler, µm	Matrix	Composition Range
[1]	German et al	Fe	-	PW	85-96 wt.%
[8]	Boudenne et al	Al	5	PP	10-60 wt.%
[13]	Weidenfeller et al	Fe_3O_4	9	PP	0-50 vol.%
[13]	Weidenfeller et al	$BaSO_4$	1.5	PP	0-50 vol.%
[13]	Weidenfeller et al	$Mg_3[Si_4O_{10}][OH]_2$	2	PP	0-50 vol.%
[13]	Weidenfeller et al	$SrFe_{12}O_{19}$	1.5	PP	0-50 vol.%
[13]	Weidenfeller et al	Cu	15	PP	0-50 vol.%
[13]	Weidenfeller et al	SiO_2	11	PP	0-50 vol.%
[40]	Subodh et al	$Sr_2Ce_2Ti_5O_{16}$	7	PTFE	0-60 vol.%
[43]	Ishida et al	BN	100	PBO	50-90 wt.%

PW: paraffin wax; PP: polypropylene; PTFE: polytetrafluoroethylene; PBO: polybenzoxazine

A limitation of the above model is that it sometimes tends to slightly under-estimate the predicted values of specific heat. In order to address this issue, Christensen et al [12] proposed a model uses the thermal expansion coefficient (α) and bulk modulus (K) of the filler and polymer. This model is shown in **Equation 2.4:**

$$C_c = \bar{C} + 9T\left(\frac{\alpha_b - \alpha_c}{1/K_b - 1/K_c}\right)^2\left[\frac{1}{K_c} - \frac{1}{K_p}\right] \qquad (2.4)$$

where, $\bar{C}$ is the specific heat calculated using the general rule of mixtures in **Equation 2.3** and T is the temperature.

The requirement of additional experimental or modeled data of the thermal expansion coefficient and bulk modulus of the various materials in **Equation 2.4** reduces the relevance of the approach for the present application of generating property estimates for mold filling simulations. A simpler model that has been successfully applied to mixtures with high volume fraction fillers [6], is shown in **Equation 2.5:**

$$C_{p_c} = \left[C_{p_b}X_b + C_{p_p}X_p\right] * \left[1 + A * X_b X_p\right] \qquad (2.5)$$

where, *A*, is a correction factor assumed to be 0.2 for spherical particles.

Experimental data of specific heat obtained for a range of filler content was selected for five different powder-polymer systems from prior studies[1], [8], [13] and compared to values predicted by **Equation 2.5**, as seen in **Figure 2.3a**. Regression analysis shows that the model has coefficient of determination (R^2) values ranging from 0.92-0.99, confirming a good applicability to predict specific heat in highly filled polymers. As an example of comparing the models represented by **Equations 2.3-2.5**, **Figure 2.3b** presents the results of predicting the specific heat of polypropylene (PP) filled with aluminum (Al) in the concentration range of 45-75 wt.% [13]. It can be seen that while all the models provide a reasonable prediction, **Equation 2.5** appears provides the best relative fit with the experimental data reported by Weidenfeller et al [13].

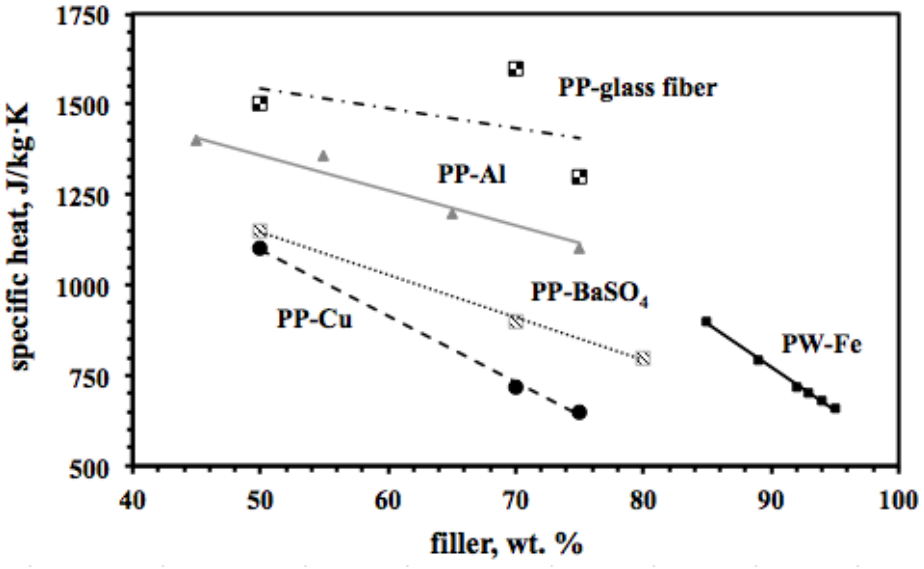

Figure 2.3a: Variation in specific heat as a function of filler content for 5 polymer-powder mixtures: PW-Fe, PP-Al, PP-Cu, PP-glass and PP-$BaSO_4$, based on the experimental data obtained from German et al [1], Boudenne et al [8] and Weidenfeller et al [13]. The lines represent predicted values based on Equation 2.3.

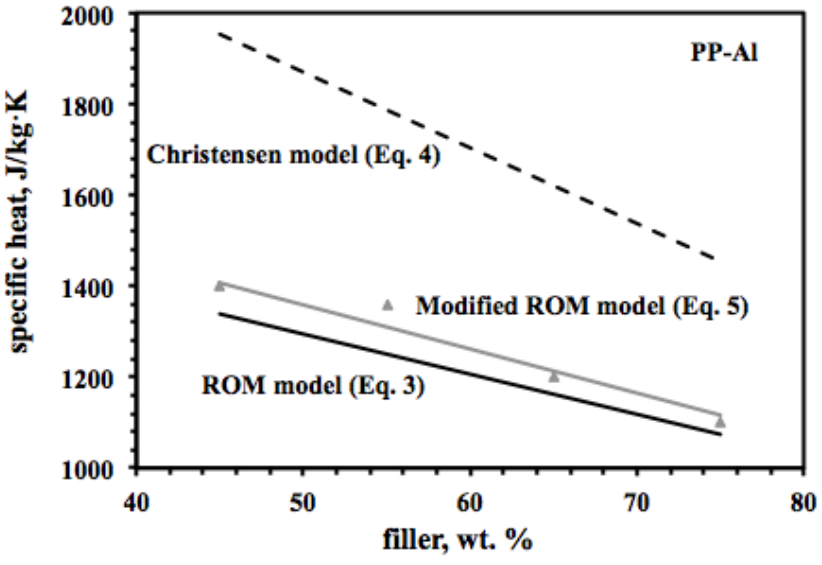

Figure 2.3b: Variation in specific heat as a function of filler content for PP-Al polymer-powder mixtures based on the experimental data obtained from Weidenfeller et al [13]. The lines represent predicted values using Equations 2.3-2.5

2.4.3 Thermal conductivity

The thermal conductivity of PIM feedstocks is significantly higher than conventional plastics, especially when the filler is metal or a ceramic such as a carbide or nitride. The implication for PIM is that solidification occurs more rapidly in these systems. Oxide ceramics on the other hand tend to be insulating. As a result, PIM processing becomes more sensitive to variations in mold and melt temperatures. **Table 2.5** summarizes the experimental data of thermal conductivity for a wide range of compositions for several powder-polymer mixtures that have been reported in the literature.

Several equations have been used to predict thermal conductivity of a composite at different filler concentrations [5, 9], 10]. The thermal conductivity of composites can be estimated using the Maxwell equation. This model can be used for two-phase mixtures having non-interacting homogenous spherical particles [3]. The Maxwell equation is as shown in **Equation 2.6**:

$$\lambda_c = \lambda_p \frac{\lambda_b + 2\lambda_p + 2\phi_p(\lambda_b - \lambda_p)}{\lambda_b + 2\lambda_p - \phi_p(\lambda_b - \lambda_p)} \qquad (2.6)$$

where, λ is the thermal conductivity, ϕ is the volume fraction of powder and the subscripts c, b and p stand for the composite, binder and powder respectively.

An approximation of the Maxwell model to predict thermal conductivity was proposed by Bruggeman. The Bruggeman model is shown in **Equation 2.7:**

$$1 - \phi_p = \left(\frac{\lambda_p - \lambda_c}{\lambda_p - \lambda_b}\right)\left(\frac{\lambda_b}{\lambda_c}\right)^{1/3} \qquad (2.7)$$

Equations 2.6 and 2.7 remain valid to predict thermal conductivities at low filler concentrations and typically cannot be used for highly filled polymers of interest in PIM.

Lichtenecker proposed a simplified model for estimating thermal conductivity as represented in **Equation 2.8:**

$$\lambda_c = {\lambda_p}^{\phi_p} {\lambda_b}^{(1-\phi_p)} \qquad (2.8)$$

Table 2.5. Literature studies on the thermal conductivity of polymer-powder mixtures

Ref. No.	Authors	Filler	Median Particle Size of Filler, μm	Matrix	Composition Range
[8]	Boudenne et al	Al	8 & 50	PP	10-60 wt.%
[13]	Weidenfeller et al	Fe_3O_4	9	PP	0-50 vol.%
[13]	Weidenfeller et al	$BaSO_4$	1.5	PP	0-50 vol.%
[13]	Weidenfeller et al	$Mg_3[Si_4O_{10}][OH]_2$	2	PP	0-50 vol.%
[13]	Weidenfeller et al	$SrFe_{12}O_{19}$	1.5	PP	0-50 vol.%
[13]	Weidenfeller et al	Cu	15	PP	0-50 vol.%
[13]	Weidenfeller et al.	glass fiber	11	PP	0-50 vol.%
[14]	Sanada et al	Al_2O_3	20	epoxy	0-60 vol.%
[17]	Wooster et al	SiO_2	6	CE	0-70 wt.%
[19]	Lee et al	wollastonite	2	HDPE	0-75 vol.%
[19]	Lee et al	SiC	1	HDPE	0-75 vol.%
[19]	Lee et al	BN	5	HDPE	0-75 vol.%
[38]	Xu et al	AlN	1.5-115	PVDF	0-60 vol.%
[38]	Xu et al	SiC whiskers	1.4	PVDF	50-60 vol.%
[40]	Subodh et al	$Sr_2Ce_2Ti_5O_{16}$	7	PTFE	0-60 vol.%
[44]	Zhou et al	Si_3N_4	2	SR	10-60 wt.%
[45]	Mutnuri	C	55	VE	50-60 wt.%
[46]	Moreira et al	Al_2O_3	0.04	UPR	0-10 vol.%
[46]	Moreira et al	CuO	0.04	UPR	0-10 vol.%
[47]	Logakis et al	carbon nanotubes	0.01	PMMA	0.5-8.0 wt.%
[48]	Dey et al	Si	10	HDPE	0-20 vol.%
[49]	Yung et al	hollow glass microspheres	30	epoxy	0-51 vol.%

SR: silicone rubber; VE: vinyl ester resin; PP: polypropylene; PTFE: polytetrafluoroethylene; UPR: unsaturated polyester resin; PMMA: polymethyl methacrylate; HDPE: high density polyethylene; PVC: polyvinyl chloride; CE: cyanate ester; PVDF: polyvinylidene fluoride

Mamunya et al developed a modified form of the Lichtenecker model [6] to account for the existence of an upper limit for ϕ as shown in **Equation 2.9**.

$$\log \lambda_c = \log \lambda_b + (\log \lambda_p - \log \lambda_b)\left(\phi_p/\phi_m\right)^N \qquad (2.9)$$

where, ϕ_m is the maximum volumetric packing fraction for the filler and N is a data-fitted constant.

The general rule-of-mixtures [10] provides a simpler approach to estimating thermal conductivity as represented in **Equation 2.10**:

$$\lambda_c = \lambda_b \phi_b + \lambda_p \phi_p \qquad (2.10)$$

Figure 2.4a shows the variation of thermal conductivity as a function of filler content obtained from experimental data for several powder-polymer systems reported in the literature [7], [14]. **Equation 10** was selected to fit the experimental data. Coefficient of determination values ranging from 0.87 to 0.99 are indicative of the applicability of the model for predicting thermal conductivity in these systems. Experimental data [19] of high density polyethylene (HDPE) filled with boron nitride (BN) was compared to predictions from **Equations 2.6, 2.7, 2.9 and 2.10** as shown in **Figures 2.4b**. It can be seen that **Equation 2.10** provides the best fit for this material system.

2.4.4 Coefficient of thermal expansion

Raising the temperature effectively decreases the volume fraction of filler because most binders have high thermal expansion coefficients as compared with the powders. For example, the thermal expansion coefficient of wax is approximately twenty times that of iron. Thus, on heating a wax-iron mixture, the higher wax expansion results in a progressive decrease in solids loading. Not only does this affect solids loading, but it also affects the molding process. Essentially, the decreasing volume fraction of powder with increased temperature makes molding much easier since viscosity decreases. However, the difference in thermal expansion coefficients between the powder and binder can result in residual thermal stresses during cooling, leading to warpage and cracks in the molded part.

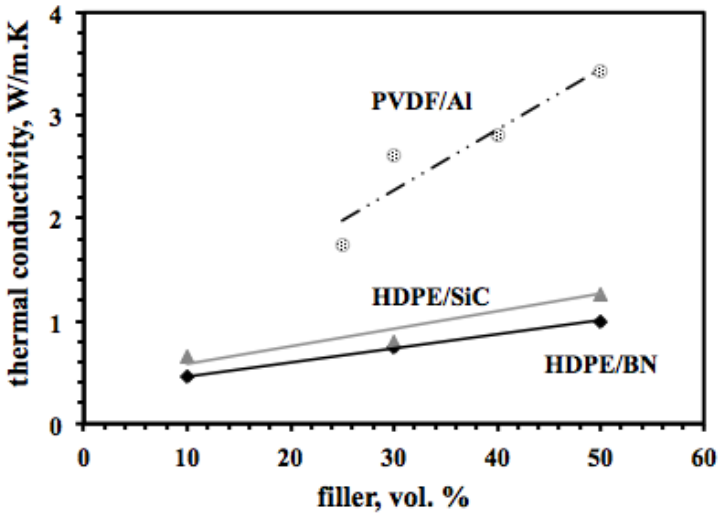

Figure 2.4a: Variation in thermal conductivity as a function of filler content for three polymer-powder mixtures: HDPE-BN, HDPE-SiC and PVDF-Al, based on the experimental data obtained from Lee et al [19] and Xu et al [38]. The lines represent predicted values based on Equation 2.10.

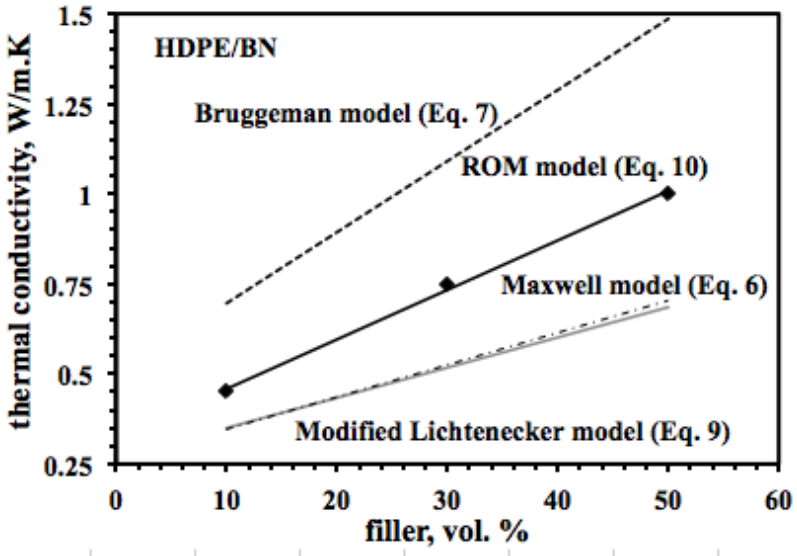

Figure 2.4b: Variation in thermal conductivity as a function of filler content for HDPE-BN polymer-powder mixtures based on experimental data obtained from Lee et al [19]. The lines show predicted values based on Equations 2.6-2.10.

Table 2.6 summarizes the experimental data of the coefficient of thermal expansion for a wide range of compositions for several powder-polymer mixtures that have been reported in the literature.

Table 2.6. Literature studies on the coefficient of thermal expansion of polymer-powder mixtures

Ref. No.	Authors	Filler	Median Particle Size of Filler, μm	Matrix	Composition Range
[2]	Brassell and Wischmann	Al_2O_3	15	epoxy	10-40 vol.%
[17]	Wooster et al	SiO_2	6	CE	0-70 wt.%
[38]	Xu et al	AlN	1.5-115	PVDF	0-60 vol.%
[38]	Xu et al	SiC whiskers	1.4	PVDF	50-60 vol.%
[39]	McGrath et al	Al_2O_3	4 -19	epoxy	0-50 vol.%
[40]	Subodh et al	$Sr_2Ce_2Ti_5O_{16}$	7	PTFE	0-0.6 vol.%
[42]	Goyal et al	Al_2O_3	0.04	PEEK	0-12 vol.%
[48]	Dey et al	Si	10	HDPE	0-20 vol.%
[49]	Yung et al	hollow glass microspheres	30	epoxy	0-51 vol. %
[50]	Elomari et al	SS 6061	150	Al_2O_3	10-20 vol.%
[51]	Hseis et al	NiAl	5	Al_2O_3	10-40 vol.%
[52]	Badrinarayan et al	ZrW_2O_8	0.1	PC	0-10 vol.%
[53]	Tognana et al	Al	110	epoxy	0-25 vol.%
[54]	Yoon et al	montmorillonite	-	nylon 6	0-7.2 wt.%

PTFE: polytetrafluoroethylene; PC: polycarbonate; HDPE: high density polyethylene; PEEK: polyether ether ketone CE: cyanate ester; PVDF: polyvinylidene fluoride

The coefficient of thermal expansion (CTE) of powder-polymer mixtures can be calculated by several models [8], [9], [15], [16]. The general rule-of-mixtures a simple approach [3] as shown in **Equation 2.11:**

$$\alpha_c = \phi_p \alpha_{\,p} + \alpha_b(1 - \phi_p) \tag{2.11}$$

where, α is the thermal expansion coefficient, ϕ is the volume fraction of the powder and the subscripts c, p and b stands for composite, powder and binder respectively. Alternatively, a similar model to **Equation 2.11** using weight fractions in stead of volume fractions has also been reported by Wooster et al [17] and Wong et al [3].

A model developed by Turner [3], [18] can be used to predict CTE. This model was based on interactions between materials in the composite and can be represented as shown in **Equation 2.12**. The shortcoming of this model was that it assumed dimension change in the composite to be same in all phases with change in temperature.

$$\alpha_c = \frac{\alpha_b K_b \phi_b + \alpha_p K_p \phi_p}{K_b \phi_b + K_p V \phi_p} \tag{2.12}$$

where, α is the thermal expansion coefficient, ϕ is volume fraction of the powder, K is bulk modulus and the subscripts c, p and b stands for composite, powder and binder respectively. Another equation which was based on interactions between materials in the composite and accounted shape effects (spherical) in predicting CTE was developed by Kerner [18] and is as shown in **Equation 2.13:**

$$\alpha_c = \alpha_b \phi_b + \alpha_p \phi_p + \phi_b \phi_p (\alpha_p - \alpha_b) \frac{K_p - K_b}{\phi_b K_b + \phi_p K_p + 3K_b K_p / 4G_b} \tag{2.13}$$

where, G is shear modulus and K is bulk modulus.

The Schapery equation [18] is also used to model thermal expansion coeffiecient and is as shown in **Equation 2.14:**

$$\alpha_c = \alpha_p + \frac{(\alpha_b - \alpha_p)\left(\left({}^{1}/_{K_c}\right) + \left({}^{1}/_{K_p}\right)\right)}{\left({}^{1}/_{K_b}\right) - \left({}^{1}/_{K_p}\right)} \tag{2.14}$$

where, K is bulk modulus. Another model used was proposed by Fahmy and Ragai [2] which is as shown in **Equation 2.15:**

$$\alpha_c = \alpha_b - \frac{3(\alpha_b - \alpha_p)(1 - \upsilon_b)\phi_p}{2(1-2\upsilon_b)\phi_p\left(\frac{E_b}{E_p}\right) + 2\phi_p(1-2\upsilon_b) + (1+\upsilon_b)} \qquad (2.15)$$

where, α is the thermal expansion coefficient, ϕ is volume fraction of the powder, E is elastic modulus, υ is the Poisson's ratio and the subscripts c, p and b stands for composite, powder and binder respectively.

The variation in coefficient of thermal expansion as a function of filler content for several polymer-powder mixtures is plotted in **Figure 2.5a** based on the experimental data reported in the literature [2], [11], [19], [20]. A regression fit based on **Equation 2.11** resulted in coefficient of difference (R^2) values ranging from 0.87-0.97, indicating a good fit. The experimental data of an epoxy filled with silica particles obtained from Feltham et al [20] were compared to predicted values from **Equations 2.11-15** computed in the study. It can be seen from **Figure 2.5b** that the models represented in **Equations 2.11, 2.14 and 2.15** provide a good fit with the experimental data thermal expansion coefficient. The need for the measurement or estimate of fewer parameters in **Equation 2.11** increases its preference.

2.4.5. Elastic and shear modulus

The feedstock elastic modulus influences molding and distortion. The molded strength of the feedstock is extremely important, since there are several handling steps after molding [68]. Binder composition influences strength, but it is not necessarily true that high binder strengths translate into high molded strengths. Adhesion between the powder and binder is important in determining the resistance to handling defects. Further, proper surfactants ensure good adhesion and greatly influence strength. Typically, the need for strength dictates the use of small particles with high inter-particle friction. Compared with the powders, it is small for most binders. For the feedstock the elastic modulus depends on the binder composition and solids loading.

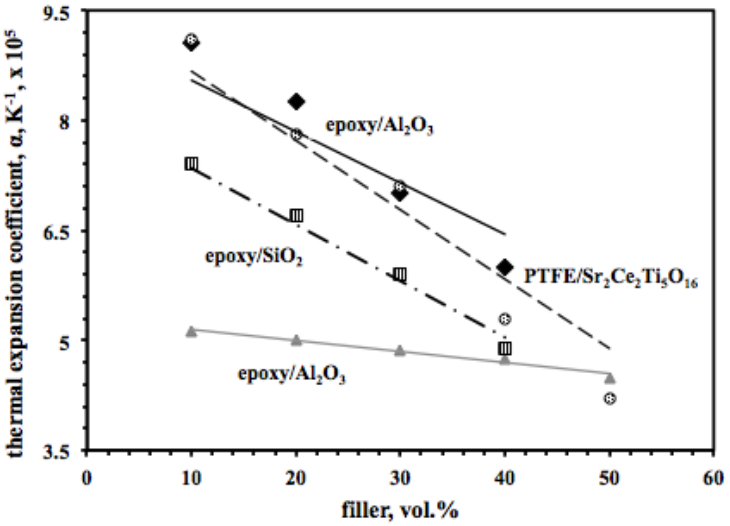

Figure 2.5a: Variation in thermal expansion coefficient as a function of filler content for polymer-powder mixtures: epoxy/Al_2O_3 and PTFE/$Sr_2Ce_2Ti_5O_{16}$ and epoxy/SiO_2, based on the experimental data obtained from Brassell et al [2], Feltham et al [20], McGrath et al [39], and Subodh et al [40]. The lines represent predicted values based on Equation 2.11.

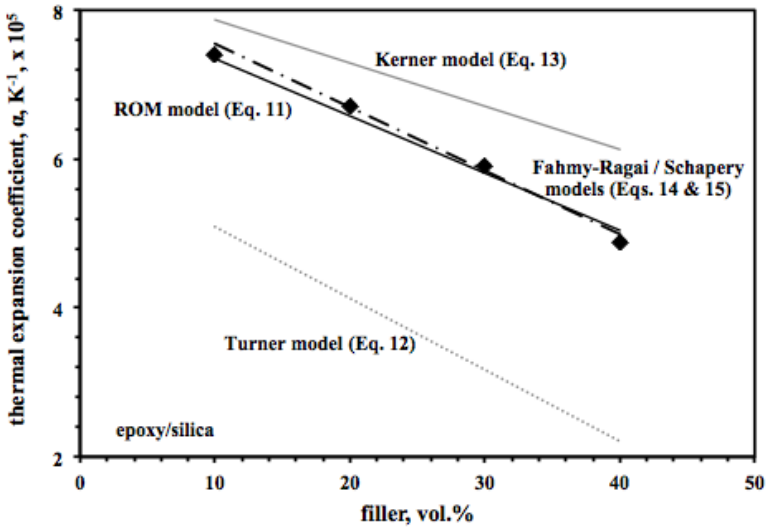

Figure 2.5b: Variation in thermal expansion coefficient as a function of filler content for epoxy/SiO_2 based on the experimental and predicted data obtained from Feltham et al [20]. The lines represent predicted values based on Equations 2.11-2.15.

Temperature further affects the elastic modulus. Polymers can store deformation energy as molecular orientations and volume dilations. Usually, the modulus decreases as temperature increases, but the relaxation of stresses due to the difference in thermal expansion coefficients between the powder and binder complicates the behavior. Consequently, the measured modulus will depend on the stress-temperature history of the feedstock. **Table 2.7** summarizes a number of powder-polymer systems for which experimental data of elastic modulus have been reported in the literature.

A model for the elastic or shear modulus based on a simple rule-of-mixtures is shown in **Equation 2.16**.

$$E_c = E_p\phi_p + E_b(1 - \phi_p) \tag{2.16}$$

where, ϕ is the volume fraction of the powder and E is the elastic or shear modulus. The subscripts c, p and b represent composite, powder and binder respectively. The Voigt model [3] is closely related to **Equation 2.16** except that weight fractions are used instead of volume fraction to predict the elastic and shear modulus.

The Reuss model is represented as shown in **Equation 2.17**. The values obtained using this equation is typically considered to be a lower bound.

$$E_c = \frac{E_b E_p}{E_b\phi_b + E_p\phi_p} \tag{2.17}$$

The variation in elastic modulus as a function of filler content for three polymer-powder mixtures is plotted in **Figure 2.6a** based on the experimental data reported in the literature [20–22]. A regression fit based on **Equation 2.16** resulted in coefficient of difference (R^2) values ranging from 0.71-0.89, indicating only a moderate fit. The experimental data of an epoxy filled with borosilicate glass particles obtained from Wu et al [22] were compared to predicted values from **Equations 2.16** and **2.17**. It can be seen from **Figure 2.6b** that the model represented in **Equation 2.16** provides a relatively better fit.

Table 2.7. Literature studies on the elastic modulus of polymer-powder mixtures

Ref. No.	Authors	Filler	Median Particle Size of Filler, μm	Matrix	Composition Range
[3]	Wong And Bollampally	SiO_2	15	epoxy	10-50 vol.%
[17]	Wooster et al	SiO_2	6	CE	0-70 wt.%
[21]	Balac et al	$Ca_{10}(PO_4)_6(OH)_2$	0.25	PLA	10-60 vol.%
[22]	Wu et al	borosilicate glass	-	epoxy	0-50 vol.%
[28]	Fornes et al	glass fiber	13	nylon 6	0-30 wt.%
[28]	Fornes et al	montmorillonite	0.01	nylon 6	0-7.2 wt.%
[55]	Saffar et al	CNT	0.15	epoxy	40-90 vol.%
[56]	Liang	glass bead	110	LDPE	0-30 wt.%
[57]	Spanoudakis et al	glass bead	4-62	epoxy	10-46 vol.%
[58]	Mishra et al	$CaCO_3$	0.03	PP	0-10 wt.%
[59]	Zhu et al	SiO_2	1.5, 0.15	PI	0-40 wt.%
[60]	Wang et al	$BaSO_4$	1.3	PP	0-32 wt.%
[60]	Wang et al	$Ca_{10}(PO_4)_6(OH)_2$	-	HDPE	0-45 vol. %
[61]	Reynaud et al	SiO_2	0.04	nylon 6	0-20 wt.%
[62]	Abu-Abdeen	Al_2O_3	<0.05	PVC	0-5 wt.%
[63]	Jaggi et al	$Ca_{10}(PO_4)_6(OH)_2$	1	HDPE	0-25 wt.%

PLA: poly-L-lactide; CE: cyanate ester; LDPE: low density polyethylene; EPDM: ethylene propylene diene monomer; PP: polypropylene; PI: polyimide; HDPE: high density polyethylene; PVC: polyvinyl chloride;

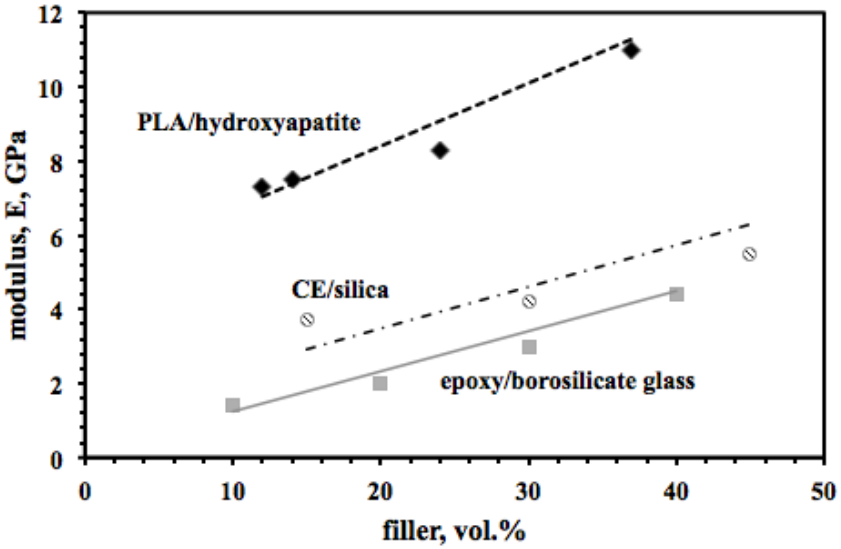

Figure 2.6a: Variation in elastic modulus as a function of filler content for 3 polymer-powder mixtures: PLA-hydroxyapatite, epoxy-borosilicate glass and CE-silica based on the experimental data obtained from Balac et al [35], Wu et al [36] and Wooster et al [37]. The lines show the predicted values based on Equation 2.16.

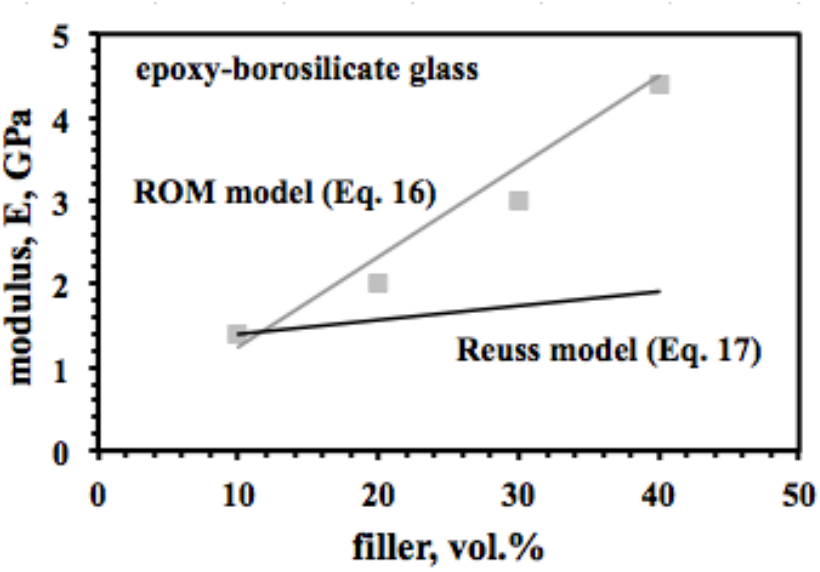

Figure 2.6b: Variation in elastic modulus as a function of filler content for 3 polymer-powder mixtures: PLA-hydroxyapatite, epoxy-borosilicate glass and CE-silica based on the experimental data obtained from Wooster et al [17], Balac et al [21], and Wu et al [22]. The lines represent predicted values based on Equation 2.16.

In order to predict the modulus as a function of the filler shape and the direction of loading, Halpin and Tsai [22] developed a widely accepted theory. This model is as shown in **Equation 2.18:**

$$\frac{E_c}{E_b} = \frac{1 + \xi\eta\phi_f}{1 - \eta\phi_f} \tag{2.18}$$

where, E is the elastic modulus, ξ is a shape parameter dependent on the geometry and loading direction, ϕ is volume fraction, subscripts f, c and b denote filler, composite and binder. The parameter η is given by **Equation 2.19:**

$$\eta = \frac{E_p/E_b - 1}{E_p/E_b + \xi} \tag{2.19}$$

The parameter, ξ can be approximated to 2 for spherical particles [22].

More accurate treatments for estimating the modulus of a composite have been proposed by several authors. For example, Hashin and Shtrikman [3] developed models where the shape of the filler is not a restraining factor. In their approach, the lower and upper bounds of the composite can calculated as shown in **Equations 2.20-2.23:**

$$K_c^l = K_b + \frac{\phi_p}{\frac{1}{(K_p - K_b)} + \frac{3(1 - \phi_p)}{(3K_b + 4G_b)}} \tag{2.20}$$

$$G_c^l = G_b + \frac{\phi_p}{\frac{1}{(G_p - G_b)} + \frac{6(1 - \phi_p)(K_b + 2G_b)}{5G_b(3K_b + 4G_b)}} \tag{2.21}$$

$$K_c^u = K_p + \frac{1 - \phi_p}{\frac{1}{(K_b - K_p)} + \frac{3\phi_p}{(3K_p + 4G_p)}} \tag{2.22}$$

$$G_c^u = G_p + \frac{1 - \phi_p}{\frac{1}{(G_b - G_p)} + \frac{6\phi_p(K_p + 2G_p)}{5G_p(3K_p + 4G_p)}} \tag{2.23}$$

where, K is the bulk modulus and G is the shear modulus.

The requirement for additional experimental or modeled data of additional parameters reduces the attractiveness of adopting models of such complexity as represented in **Equations 2.20-2.23**. Additional work is needed to establish the need for such methods for estimating data of relevance to performing mold-filling simulations.

2.4.6 Viscosity

Mold filling depends on viscous flow of the molten feedstock into the die cavity. This requires the knowledge of specific rheological characteristics of polymer-powder mixtures. The feedstock viscosity increases with the addition of powder. As the powder to binder ratio increases the viscosity becomes essentially infinite at the critical solids loading. Smaller particles inherently have more surface area and inter-particle friction. Accordingly, the viscosity of a powder-binder mixture is dependent on the inverse of the particle size. As a result of variations in powder characteristics, the composition of PIM feedstocks typically range from 45 vol.% to 75 vol.% filler content. Ceramic feedstocks, having relatively finer particle size, have a filler content ranging between 50 and 55 vol.%, depending on the powder and binder, while feedsotcks based on iron and steels, having relatively coarser particle size, are routinely processed in the 58 to 62 vol.% filler content. Rheological evaluations of powder-binder mixtures can be used in simulations and molding trials to identify conditions leading to flow instabilities, arising from material composition, molding temperature, filler content, shear rate, or tool design. Rheological evaluation also serves as a quality control tool in a PIM operation. **Table 2.8** summarizes a number of powder-polymer systems for which experimental rheological data have been reported in the literature.

The increase in viscosity of a suspension due to the addition of particles was first analyzed by Einstein[23], [24] as shown in **Equation 2.24**:

$$\eta_r = 1 + 2.5\phi_p \tag{2.24}$$

where, η_r is the relative viscosity of the suspension and represents the ratio of the viscosity of the mixture to the viscosity of the unfilled polymer melt. The linear dependence depicted in the above equation is only valid for very dilute suspensions where particles do not interact with each other.

Table 2.8. Literature studies on the viscosity of polymer-powder mixtures

Ref. No.	Authors	Filler	Median Particle Size of Filler, μm	Matrix	Composition Range
[27]	Zhang and Evans	Al_2O_3	0.8	LDPE	40-60 vol. %
[29]	Arefinia et al	Al	4-150	PB	0-50 vol.%
[29]	Arefinia et al	NH_4ClO_4	38-150	PB	0-50 vol.%
[41]	Osman et al	$CaCO_3$	2	HDPE	0-30 vol. %
[62]	Abu-Abdeen	Al_2O_3	0.04	PVC	0-5 wt.%

LDPE: low density polyethylene; PVC: polyvinyl chloride; PB: polybutadiene; HDPE: high density polyethylene

A model proposed by Mooney [25] is shown in **Equation 2.25**:

$$\eta_c = \exp\left(\frac{2.5\phi_p}{1 - k\phi_p}\right) \qquad (2.25)$$

where, η represents the viscosity, k is $1/\phi_m$ where m is maximum packing fraction while the subscripts c represent composite. **Equation 2.25** holds true for predicting viscosity at low concentration of fillers but predicts unrealistic values at high concentrations of fillers.

Another model that can be used to predict viscosity was proposed by Eiler [25], as shown in **Equation 2.26**:

$$\eta_c = \left(1 + \frac{1.25\phi_p}{1 - \phi_p/\phi_b}\right)^2 \qquad (2.26)$$

where, subscript b represents binder in the composite. Although this model predicts values that have a better data fit in comparison to Mooney's equation, it deviates from the experimental values at high concentration of fillers.

Chong et al [25] proposed a model that can be used to calculate relative viscosity as shown in **Equation 2.27:**

$$\eta_r = \left(\frac{\phi_b - 0.25\phi_p}{\phi_b - \phi_p}\right)^2 \qquad (2.27)$$

However, the above model fails to capture the physical effect of the existence of an upper limit for ϕ_p.

The Krieger-Dougherty [23], [24], [26] has been found to be suitable for predicting viscosity values at higher volume fractions of powder. A simplified form of the model is given in **Equation 2.28:**

$$\eta_c = \frac{\eta_b}{\left[1 - \frac{\phi_p}{\phi_m}\right]^2} \qquad (2.28)$$

where, the parameter, ϕ_m, stands for the maximum packing fraction of the powder.

Figure 2.7a shows the variation of viscosity as a function of filler content for three powder-polymer systems reported in the literature [27–29]. The data was fitted to predicted values using **Equation 2.28**. The coefficient of determination values ranged from 0.94-0.99 indicating excellent fit with the selected data. The experimental data of viscosity as a function of filler content for low density polyethylene (LDPE) filled with alumina (Al_2O_3) was obtained from the literature [27] and compared to predicted values based on **Equations 2.25-2.28** as shown in **Figure 2.7b**. It can be seen that the simplified Krieger-Dougherty model provides the best fit with the experimental data for the LDPE- Al_2O_3 system.

In addition to binder and powder effects, feedstock viscosity is sensitive to shear rate. Most PIM mixtures exhibit pseudoplastic behavior. Accordingly, a simple melt flow

index is inappropriate and the viscosity must be measured over a range of conditions that reflect those expected during injection molding.

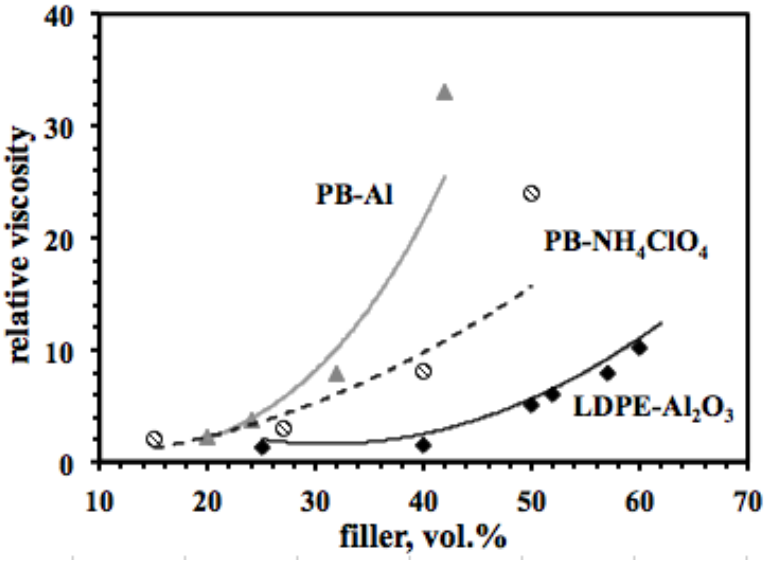

Figure 2.7a: Variation in viscosity as a function of filler content for 3 polymer-powder mixtures: LDPE-Al_2O_3, PB-Al and PB-NH_4ClO_4, based on the experimental data obtained from Zhang et al [27], Arefinia et al [29], and Osman et al [41]. The lines represent predicted values based on Equation 2.28.

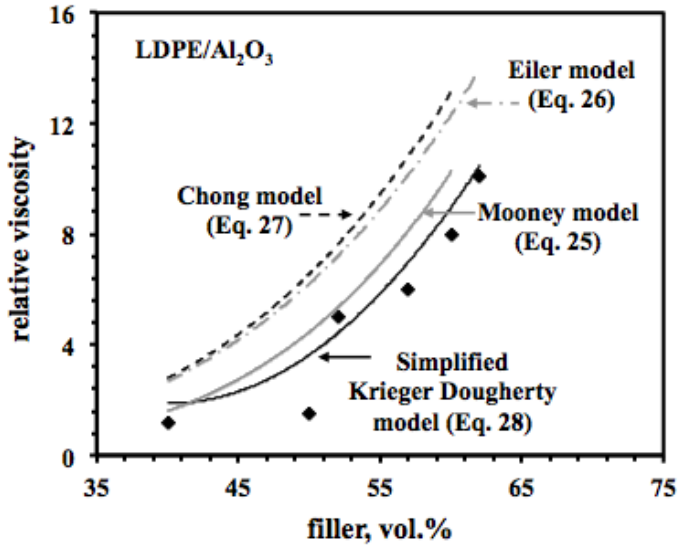

Figure 2.7b: Variation in viscosity as a function of filler content for LDPE-Al_2O_3, based on the experimental data obtained from Zhang et al [27]. The lines show predicted values based on Equations 25-28.

The Cross-WLF model [30] can be used to model the viscosity dependence of any given powder-polymer mixture on shear rate as shown in **Equation 2.29**:

$$\eta = \frac{\eta_o}{1 + \left(\frac{\eta_o \dot{\gamma}}{\tau^*}\right)^{1-n}} \qquad (2.29)$$

where, η is the melt viscosity (Pa-s), η_o is the zero shear viscosity(Pa-s), $\dot{\gamma}$ is the shear rate (s^{-1}), τ^* is the critical stress level at the transition to shear thinning (Pa), determined by curve fitting, and n is the power law index in the high shear rate regime, also determined by curve fitting.

Viscosity is also sensitive to temperature. At low temperatures the mixture viscosity is too high for standard molding conditions. At high temperatures the binder may be too thin, causing separation during molding. Thus, a narrow range of conditions exists over which PIM processing is most viable. The temperature dependence of viscosity of any powder-polymer mixture [30] can be calculated using **Equation 2.30:**

$$\eta_0 = D_1 exp\left[-\frac{A_1(T - T^*)}{A_2 + (T - T^*)}\right] \qquad (2.30)$$

where, T is the temperature (K). T^*, D_1 and A_1, are curve fitted coefficients. Additionally, A_2 is the WLF constant and is assumed to be 51.6 K. The values of these coefficients can be obtained by curve-fitting the estimated viscosity for different volume fractions of powder at various shear rates and temperatures.

Figure 2.8 plots the viscosity as a function of shear rate at two different temperatures for aluminum nitride (AlN) feedstocks incorporated with a paraffin wax-polypropylene binder system at 48 vol. % and 50 vol. % filler content using **Equations 2.28-2.30** [31]. The viscosity of these feedstocks was predicted using experimental data at 0 and 52 vol. % filler. Such estimates can be useful to examine the sensitivity of powder content on the mold-filling behavior of PIM feedstocks.

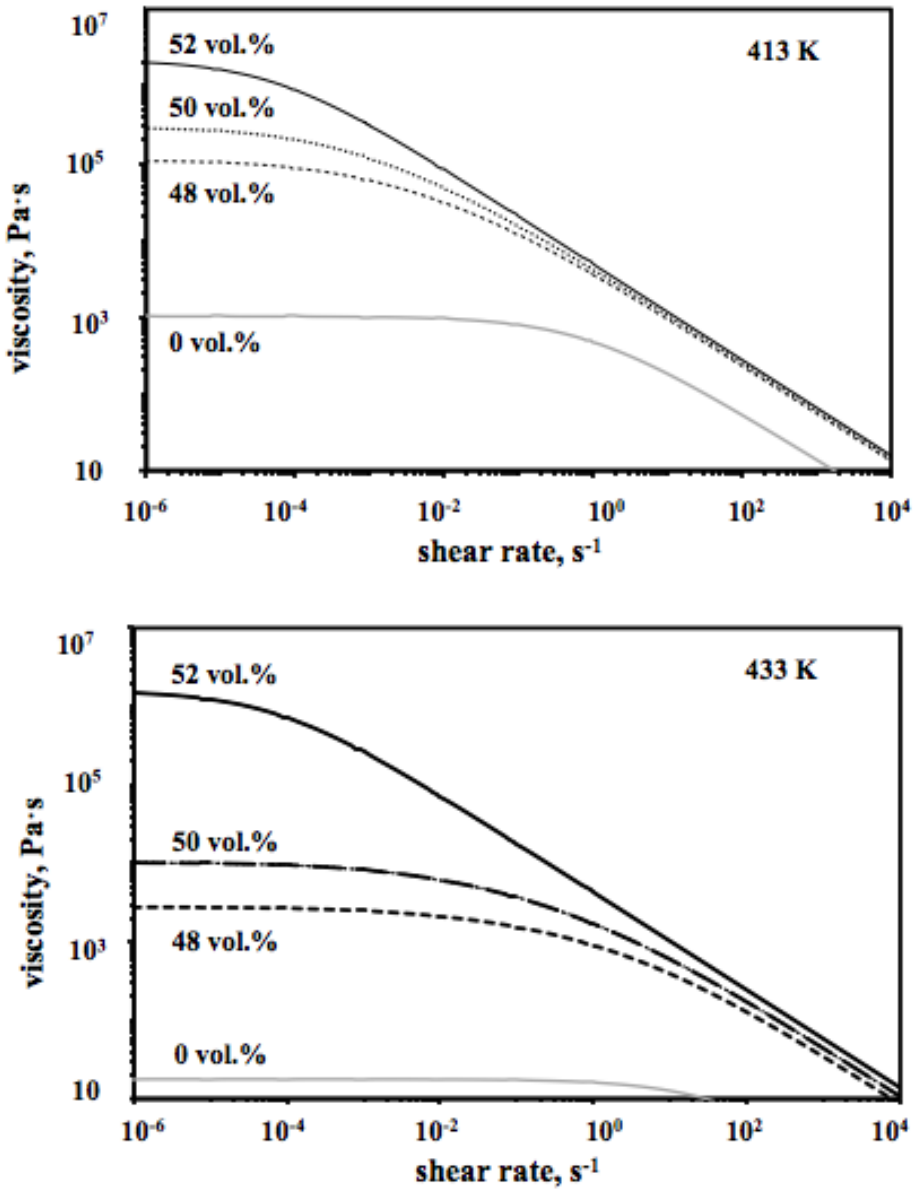

Figure 2.8: Comparison of viscosity with shear rate at 413 K (top) and 433 K (bottom) for different volume fractions of AlN powder, ϕ_p [31].

2.4.8 Specific volume

Shrinkage and warpage problems in molded components depend on the molecular orientation of polymers as well as residual stresses that form during processing as a result of flow and heat transfer during the filling, packing and cooling stages of the PIM

process. The change in specific volume of a PIM feedstock as a function of temperature and pressure (PvT) is used in conjunction with the temperature-dependent stress-strain behavior to predict the origin of such molding defects as a function of tool geometry and process conditions using simulation platforms. **Table 2.9** lists some studies on the PvT behavior of filled polymers found in the literature.

Table 2.9. Literature studies on the PvT behavior of polymer-powder mixtures

Ref. No.	Authors	Filler	Median Particle Size of Filler, μm	Matrix	Composition Range
[64]	Areerat et al	TiO_2	0.3	LDPE	10-20 wt.%
[65]	Dlubek et al	fumed silica	1	PDMS	35 wt.%
[66]	Carrubba et al	glass	30	PET, PBT, PA, PC	35-60 wt.%

LDPE: low density polyethylene; PDMS: polydimethyl siloxane; PET: polyethylene terephthalate, PBT: polybutylene terephthalate, PA: polyamide, PC: polycarbonate

The specific volume was calculated using the rule-of-mixtures [10] shown in **Equation 2.31:**

$$\upsilon_c = X_p \upsilon_p + \upsilon_b (1 - X_f) \qquad (2.31)$$

where, υ is the specific volume, X is the mass fraction of the powder and the subscripts c, p and b refer to the composite, powder and binder respectively. **Equation 2.31** is similar to **Equation 2.1** (specific volume being the reciprocal of density) and is used to predict the change in specific volume as a function of filler content for two powder-polymer systems in **Figure 2.9**. Coefficient of determination values of 0.99 indicate he suitability of **Equation 2.31** for predicting the specific volume for polypropylene (PP) filled with aluminum (Al) particles based on experimental data found in the literature [8].

Most injection molding software platform use a two-domain Tait [30] model **(Equation 2.32)** for generating specific volume data as a function of temperature and pressure.:

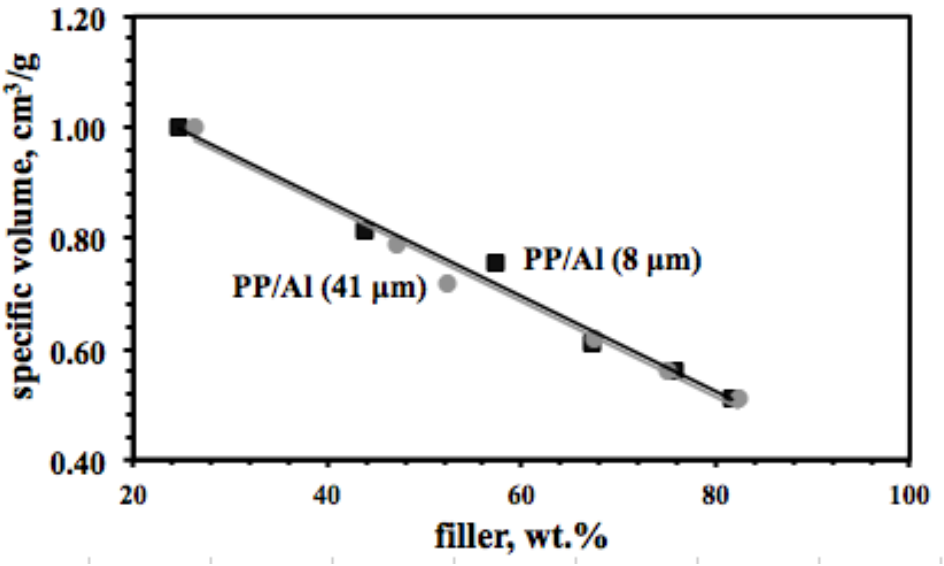

Figure 2.9: Variation in specific volume as a function of filler content for PP-Al mixtures, based on the experimental data obtained from Boudenne et al [8]. The lines show predicted values based on Equation 2.31.

$$\upsilon(T,p) = \upsilon_o(T)\left[1 - Cln\left(1 + \frac{p}{B(T)}\right) + \upsilon_t(T,p)\right] \qquad (2.32)$$

where, υ (T,p) is the specific volume at a given temperature and pressure, υ_o is the specific volume at zero gauge pressure, T is temperature in K, p is pressure in Pa, and C is a constant assumed as 0.0894. The parameter, B, accounts for the pressure sensitivity of the material and is separately defined for the solid and melt regions. For the upper bound [30] when $T > T_t$ (volumetric transition temperature), B is given by **Equation 2.33:**

$$\upsilon_o = b_{1m} + b_{2m}(T - b_5)B(T) = b_{3m}e^{[-b_{4m}(T-b_5)]}\upsilon_t(T,p) = 0 \qquad (2.33)$$

where, b_{1m}, b_{2m}, b_{3m}, b_{4m}, and b_5 are curve-fitted coefficients. For the lower bound [30], when $T < T_t$, the parameter, B, is given by **Equation 2.34:**

$$\upsilon_o = b_{1s} + b_{2s}(T - b_5)B(T) = b_{2s}e^{[-b_{4s}(T-b_5]}\upsilon_t(T,p) = b_7e^{[b_8(T-b_5)-(b_9p)]} \qquad (2.34)$$

where, b_{1s}, b_{2s}, b_{3s}, b_{4s}, b_5, b_7, b_8, and b_9 are curve-fitted coefficients. The dependence of the volumetric transition temperature, T_t on pressure can be given by $T_t(p) = b_5+b_6(p)$, where b_5 and b_6 are curve-fitted coefficients.

Figure 2.10 shows the predicted PvT behavior of aluminum nitride (AlN) feedstocks incorporated with a paraffin wax-polypropylene binder system at 48 vol. % and 50 vol. % filler content using **Equations 2.31-2.34** [31].

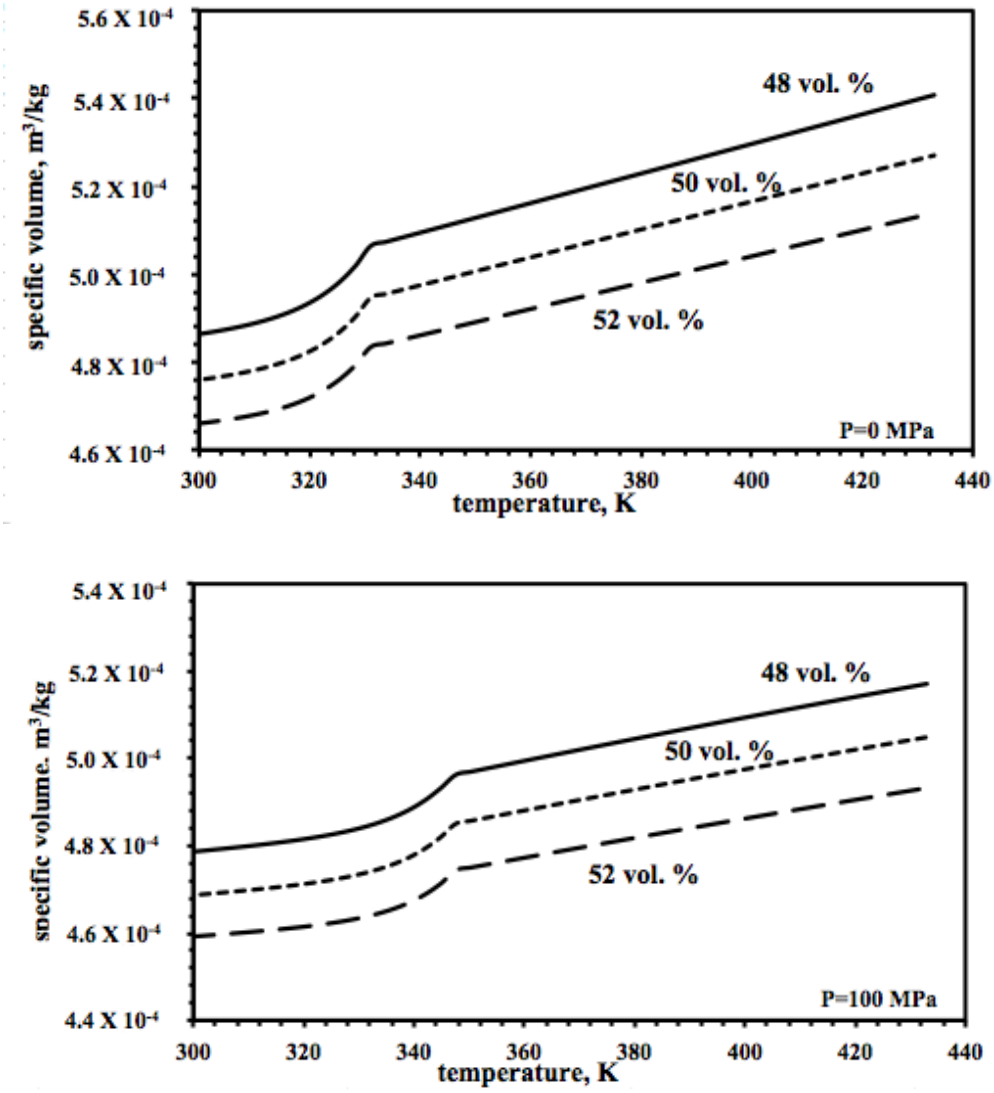

Figure 2.10: PVT behavior for 0 and100 MPa pressures for different volume fractions of AlN powder, ϕ_p [31].

The PvT data for these feedstocks was predicted using experimental data obtained at 0 and 52 vol. % filler. Such estimates can be useful to examine the influence of powder content on the shrinkage and warpage characteristics of PIM feedstocks.

Table 2.10 summarizes the coefficients of determination (R^2) for the most useful models for predicting all the material properties based on evaluation against experimental data obtained from the literature. It is anticipated that these models can be used in conjunction with limited experimentation to accurately simulate the mold filling behavior of PIM feedstocks using commercially available platforms such as PIMSolver and Moldflow [32–36]. The models discussed in this review do not specifically address variations in particle characteristics (e.g. shape, size, agglomeration) but can serve as a first step towards eliminating the trial-and-error procedures currently prevalent in the design of PIM parts [37]. Examples of mold-filling simulations for a broad range of applications are shown in **Figure 2.11**.

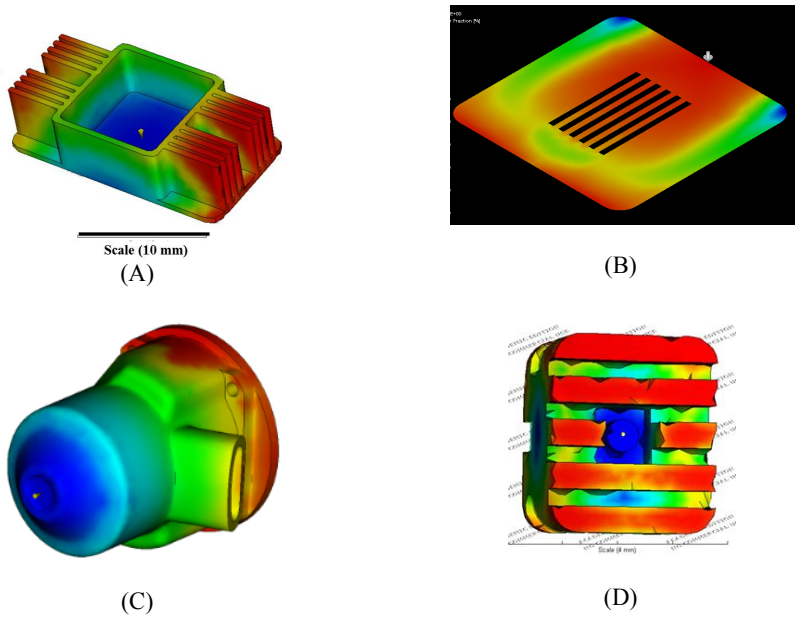

Figure 2.11: Examples of studies on mold –filling simulations for several applications and material systems (A) AlN heat sink [31], (B) 316L stainless steel microfluidic plate [36], (C) Si_3N_4 engine component [67], and (D) Al_2O_3 dental bracket [68].

Table 2.10. Coefficient of determination (R^2) values of predictive models

Property	Ref. No.	Authors	Material System	Model	R^2
Density	[11]	Rajesh et al	PTFE/TiO_2	Equation 1	1
	[11]	Rajesh et al	PTFE/$BaSm_2Ti_4O_{12}$		0.988
	[11]	Rajesh et al	PTFE/$BaPr_2Ti_4O_{12}$		0.971
Specific heat	[1]	German et al	PW/Fe	Equation 5	0.996
	[8]	Boudenne et al	PP/Al		0.981
	[13]	Weidenfeller et al	PP/Cu		0.998
	[13]	Weidenfeller et al	PP/GF		0.921
Thermal conductivity	[44]	Zhou et al	SR/Si_3N_4	Equation 10	0.87
	[19]	Lee et al	HDPE/BN		0.999
	[19]	Lee et al	HDPE/wollastonite		0.94
	[19]	Lee et al	HDPE/SiC		0.98
	[38]	Xu et al	PVDF/Al		0.99
Thermal expansion coefficient	[2]	Brassell et al	epoxy/Al_2O_3	Equation 11	0.87
	[39]	McGrath et al	epoxy/Al_2O_3		0.972
	[40]	Subodh et al	PTFE/$Sr_2Ce_2Ti_5O_{16}$		0.88
Modulus	[21]	Balac et al	PLA/ $Ca_{10}(PO_4)_6(OH)_2$	Equation 15	0.72
	[22]	Wu et al	epoxy/borosilicate		0.89
	[17]	Wooser et al	CE-SiO_2		0.88
	[28]	Fornes et al	nylon 6/glass fiber		0.77
Viscosity	[27]	Zhang et al	LDPE/Al_2O_3	Equation 25	0.94
	[29]	Arefinia et al	PB/Al		0.998
	[29]	Arefinia et al	PB/NH_4ClO_4		0.997
	[40]	Osman et al	PB/Al		0.968
Specific volume	[8]	Boudenne et al	PP/Al (41μm)	Equation 31	0.99
	[8]	Boudenne et al	PP/Al (8μm)		0.99

PTFE: polytetrafluoroethylene; PW: paraffin wax; PP: polypropylene; SR: silicone rubber; HDPE: high density polyethylene; PLA: poly-L-lactide; CE: cyanate ester; PVDF: polyvinylidene fluoride; LDPE: low density polyethylene; PB: polybutadiene

2.5. Conclusions

A literature review of the thermal, rheological and PVT properties of powder-polymer mixtures was conducted. The experimental data for each property as a function of filler volume fraction was selected for several powder-polymer systems and compared to predicted data from various mixture models. Regression analysis on the modeled data allowed the assessment of the suitability of models for estimating material properties for highly filled polymers. The combination of experimental methods and constitutive models analyzed in this paper presents a useful approach to scale material property data as a function of filler content by combining limited experimentation with appropriate models for predicting powder-polymer mixture properties. It is expected that such an approach will increase the design accuracy of part, mold and processes for a broad range of materials systems used in PIM, in a cost-effective manner. It is further anticipated that the approach presented in this paper will avoid expensive and time-consuming, trial-and-error iterations currently prevalent in PIM.

Acknowledgment

S.V. Atre would like to acknowledge financial support from the National Science Foundation (Award # CMMI 1200144).

2.6. References

[1] R. M. German and S. J. Park, Mathematical Relations in Particulate Materials Processing: Ceramics, Powder Metals, Cermets, Carbides, Hard Materials, and Minerals. John Wiley & Sons, 2008.

[2] G. W. Brassell and K. B. Wischmann, “Mechanical and thermal expansion properties of a participate filled polymer,” Journal of Materials Science, vol. 9, no. 2, pp. 307–314, 1974.

[3] C. P. Wong and R. S. Bollampally, “Thermal conductivity, elastic modulus, and coefficient of thermal expansion of polymer composites filled with ceramic particles for

electronic packaging," Journal of Applied Polymer Science, vol. 74, no. 14, pp. 3396–3403, 1999.

[4] S. McGee and R. L. McGullough, "Combining rules for predicting the thermoelastic properties of particulate filled polymers, polymers, polyblends, and foams," Polymer Composites, vol. 2, no. 4, pp. 149–161, 1981.

[5] J. Chen, J.-G. Mi, and K.-Y. Chan, "Comparison of different mixing rules for prediction of density and residual internal energy of binary and ternary Lennard–Jones mixtures," Fluid Phase Equilibria, vol. 178, no. 1–2, pp. 87–95, 2001.

[6] Y. P. Mamunya, "Electrical and thermal conductivity of polymers filled with metal powders," European Polymer Journal, vol. 38, no. 9, p. 1887, 2002.

[7] D. W. Sundstrom and Y.-D. Lee, "Thermal conductivity of polymers filled with particulate solids," Journal of Applied Polymer Science, vol. 16, no. 12, pp. 3159–3167, 1972.

[8] A. Boudenne, L. Ibos, M. Fois, E. Gehin, and J.-C. Majeste, "Thermophysical properties of polypropylene/aluminum composites," Journal of Polymer Science Part B: Polymer Physics, vol. 42, no. 4, pp. 722–732, 2004.

[9] M. J. Edirisinghe and J. R. G. Evans, "Review: Fabrication of engineering ceramics by injection moulding. I. Materials selection," International Journal of High Technology Ceramics, vol. 2, no. 1, pp. 1–31, 1986.

[10] L. E. Nielsen, Predicting the properties of mixtures: mixture rules in science and engineering. M. Dekker, 1978.

[11] S. Rajesh, K. P. Murali, H. Jantunen, and R. Ratheesh, "The effect of filler on the temperature coefficient of the relative permittivity of PTFE/ceramic composites," Physica B: Condensed Matter, vol. 406, no. 22, pp. 4312–4316, 2011.

[12] A. Christensen and S. Graham, “Thermal effects in packaging high power light emitting diode arrays,” Applied Thermal Engineering, vol. 29, no. 2–3, pp. 364–371, 2009.

[13] B. Weidenfeller, M. Höfer, and F. R. Schilling, “Thermal conductivity, thermal diffusivity, and specific heat capacity of particle filled polypropylene,” Composites Part A: Applied Science and Manufacturing, vol. 35, no. 4, pp. 423–429, 2004.

[14] K. Sanada, Y. Tada, and Y. Shindo, “Thermal conductivity of polymer composites with close-packed structure of nano and micro fillers,” Composites Part A: Applied Science and Manufacturing, vol. 40, no. 6–7, pp. 724–730, 2009.

[15] T. Zhang, J. R. G. Evans, and K. K. Dutta, “Thermal properties of ceramic injection moulding suspensions in the liquid and solid states,” Journal of the European Ceramic Society, vol. 5, no. 5, pp. 303–309, 1989.

[16] D. T. Jamieson and G. Cartwright, Properties of Binary Liquid Mixtures: Heat Capacity. National Engineering Laboratory, 1978.

[17] T. J. Wooster, S. Abrol, J. M. Hey, and D. R. MacFarlane, “Thermal, mechanical, and conductivity properties of cyanate ester composites,” Composites Part A: Applied Science and Manufacturing, vol. 35, no. 1, pp. 75–82, 2004.

[18] C. L. Hsieh and W. H. Tuan, “Elastic properties of ceramic–metal particulate composites,” Materials Science and Engineering A, vol. 393, no. 1–2, pp. 133–139, 2005.

[19] G.-W. Lee, M. Park, J. Kim, J. I. Lee, and H. G. Yoon, “Enhanced thermal conductivity of polymer composites filled with hybrid filler,” Composites Part A: Applied Science and Manufacturing, vol. 37, no. 5, pp. 727–734, 2006.

[20] S. J. Feltham, B. Yates, and R. J. Martin, “The thermal expansion of particulate-reinforced composites,” Journal of Materials Science, vol. 17, no. 8, pp. 2309–2323, 1982.

[21] I. Balać, M. Milovančević, C. Tang, P. S. Uskoković, and D. P. Uskoković, "Estimation of elastic properties of a particulate polymer composite using a face-centered cubic FE model," Materials Letters, vol. 58, no. 19, pp. 2437–2441, 2004.

[22] W. Wu, K. Sadeghipour, K. Boberick, and G. Baran, "Predictive modeling of elastic properties of particulate-reinforced composites," Materials Science and Engineering: A, vol. 332, no. 1–2, pp. 362–370, 2002.

[23] A. B. Metzner, "Rheology of suspensions in polymeric liquids," Journal of Rheology, vol. 29, no. 6, pp. 739–775, 1985.

[24] C. W. Macosko, Rheology: principles, measurements, and applications. VCH, 1994.

[25] X. Z. Shi, M. Huang, Z. F. Zhao, and C. Y. Shen, "Nonlinear fitting technology of 7-parameter cross-wlf viscosity model," Advanced Materials Research, vol. 189–193, pp. 2103–2106, 2011.

[26] V. P. Onbattuvelli, "The effects of nanoparticle addition on the processing, structure and properties of SiC and AlN," Thesis/Dissertation, 2010.

[27] T. Zhang and J. R. G. Evans, "Predicting the viscosity of ceramic injection moulding suspensions," Journal of the European Ceramic Society, vol. 5, no. 3, pp. 165–172, 1989.

[28] T. D. Fornes and D. R. Paul, "Modeling properties of nylon 6/clay nanocomposites using composite theories," Polymer, vol. 44, no. 17, pp. 4993–5013, 2003.

[29] R. Arefinia and A. Shojaei, "On the viscosity of composite suspensions of aluminum and ammonium perchlorate particles dispersed in hydroxyl terminated polybutadiene-New empirical model," J Colloid Interface Sci, vol. 299, no. 2, pp. 962–971, 2006.

[30] H. H. Chiang, C. A. Hieber, and K. K. Wang, “A unified simulation of the filling and postfilling stages in injection molding. Part I: Formulation,” Polymer Engineering & Science, vol. 31, no. 2, pp. 116–124, 1991.

[31] K. H. Kate, V. P. Onbattuvelli, R. K. Enneti, S. W. Lee, S.-J. Park, and S. V. Atre, “Measurements of powder–polymer mixture properties and their use in powder injection molding simulations for aluminum nitride,” JOM, vol. 64, no. 9, pp. 1048–1058, 2012.

[32] S. J. Park, S. Ahn, T. G. Kang, S. T. Chung, Y. S. Kwon, S. H. Chung, S. G. Kim, S. Kim, S. V. Atre, S. Lee, and R. M. German, “A review of computer simulations in powder injection molding,” International Journal of Powder Metallurgy, vol. 46, no. 3, pp. 37–46, 2010.

[33] R. Urval, S. Lee, S. V. Atre, S.-J. Park, and R. M. German, “Optimisation of process conditions in powder injection moulding of microsystem components using robust design method Part 2 – Secondary design parameters,” Powder Metallurgy, vol. 53, no. 1, pp. 71–81, 2010.

[34] S. Ahn, S. J. Park, S. Lee, S. V. Atre, and R. M. German, “Effect of powders and binders on material properties and molding parameters in iron and stainless steel powder injection molding process,” Powder Technology, vol. 193, no. 2, pp. 162–169, 2009.

[35] S. V. Atre, S.-J. Park, R. Zauner, and R. M. German, “Process simulation of powder injection moulding: identification of significant parameters during mould filling phase,” Powder Metallurgy, vol. 50, no. 1, pp. 76–85, 2007.

[36] R. Urval, S. Lee, S. V. Atre, S.-J. Park, and R. M. German, “Optimisation of process conditions in powder injection moulding of microsystem components using a robust design method: Part I. primary design parameters,” Powder Metallurgy, vol. 51, no. 2, pp. 133–142, 2008.

[37] R. M. German, Powder injection molding : design and applications. State College, PA: Innovative Material Solutions, 2003.

[38] Y. Xu, D. D. . Chung, and C. Mroz, “Thermally conducting aluminum nitride polymer-matrix composites,” Composites Part A: Applied Science and Manufacturing, vol. 32, no. 12, pp. 1749–1757, 2001.

[39] L. M. McGrath, R. S. Parnas, S. H. King, J. L. Schroeder, D. A. Fischer, and J. L. Lenhart, “Investigation of the thermal, mechanical, and fracture properties of alumina–epoxy composites,” Polymer, vol. 49, no. 4, pp. 999–1014, 2008.

[40] G. Subodh, M. V. Manjusha, J. Philip, and M. T. Sebastian, “Thermal properties of polytetrafluoroethylene/$Sr_2Ce_2Ti_5O_{16}$ polymer/ceramic composites,” Journal of Applied Polymer Science, vol. 108, no. 3, pp. 1716–1721, 2008.

[41] M. A. Osman and A. Atallah, “Interparticle and particle–matrix interactions in polyethylene reinforcement and viscoelasticity,” Polymer, vol. 46, no. 22, pp. 9476–9488, 2005.

[42] R. K. Goyal, A. N. Tiwari, U. P. Mulik, and Y. S. Negi, “Novel high performance Al_2O_3/poly(ether ether ketone) nanocomposites for electronics applications,” Composites Science and Technology, vol. 67, no. 9, pp. 1802–1812, 2007.

[43] H. Ishida and S. Rimdusit, “Heat capacity measurement of boron nitride-filled polybenzoxazine: The composite structure-insensitive property,” Journal of Thermal Analysis and Calorimetry, vol. 58, no. 3, pp. 497–507, 1999.

[44] W. Zhou, C. Wang, Q. An, and H. Qu, “Thermal properties of heat conductive silicone rubber filled with hybrid fillers,” Journal of Composite Materials, vol. 42, no. 2, pp. 173–187, 2008.

[45] B. Mutnuri, “Thermal Conductivity Characterization of Composite Materials,” West Virginia University, Morgantown, W. Va., 2006.

[46] D. C. Moreira, L. A. Sphaier, J. M. L. Reis, and L. C. S. Nunes, “Experimental investigation of heat conduction in polyester–Al_2O_3 and polyester–CuO nanocomposites,” Experimental Thermal and Fluid Science, vol. 35, no. 7, pp. 1458–1462, 2011.

[47] E. Logakis, C. Pandis, P. Pissis, J. Pionteck, and P. Pötschke, “Highly conducting poly(methyl methacrylate)/carbon nanotubes composites: Investigation on their thermal, dynamic-mechanical, electrical and dielectric properties,” Composites Science and Technology, vol. 71, no. 6, pp. 854–862, 2011.

[48] T. K. Dey and M. Tripathi, “Thermal properties of silicon powder filled high-density polyethylene composites,” Thermochimica Acta, vol. 502, no. 1–2, pp. 35–42, 2010.

[49] K. C. Yung, B. L. Zhu, T. M. Yue, and C. S. Xie, “Preparation and properties of hollow glass microsphere-filled epoxy-matrix composites,” Composites Science and Technology, vol. 69, no. 2, pp. 260–264, 2009.

[50] S. Elomari, R. Boukhili, and D. J. Lloyd, “Thermal expansion studies of prestrained Al_2O_3/Al metal matrix composite,” Acta Materialia, vol. 44, no. 5, pp. 1873–1882, 1996.

[51] C. L. Hsieh and W. H. Tuan, “Thermal expansion behavior of a model ceramic–metal composite,” Materials Science and Engineering: A, vol. 460–461, no. 0, pp. 453–458, 2007.

[52] P. Badrinarayanan and M. R. Kessler, “Zirconium tungstate/cyanate ester nanocomposites with tailored thermal expansivity,” Composites Science and Technology, vol. 71, no. 11, pp. 1385–1391, 2011.

[53] S. Tognana, W. Salgueiro, A. Somoza, J. A. Pomarico, and H. F. Ranea-Sandoval, “Influence of the filler content on the thermal expansion behavior of an epoxy

matrix particulate composite," Materials Science and Engineering: B, vol. 157, no. 1–3, pp. 26–31, 2009.

[54] P. J. Yoon, T. D. Fornes, and D. R. Paul, "Thermal expansion behavior of nylon 6 nanocomposites," Polymer, vol. 43, no. 25, pp. 6727–6741, 2002.

[55] K. PourAkbar Saffar, A. R. Arshi, N. JamilPour, A. R. Najafi, G. Rouhi, and L. Sudak, "A cross-linking model for estimating Young's modulus of artificial bone tissue grown on carbon nanotube scaffold," Journal of Biomedical Materials Research Part A, vol. 94A, no. 2, pp. 594–602, 2010.

[56] J. Z. Liang, "Viscoelastic properties and characterization of inorganic particulate-filled polymer composites," Journal of Applied Polymer Science, vol. 114, no. 6, pp. 3955–3960, 2009.

[57] J, Spanoudakis, J. and R. J.Young, "Crack propagation in a glass particle-filled epoxy resin Part 1. Effect of particle volume fraction and size : Journal of Materials Science Vol 19 (1984) pp 473–486," Composites, vol. 15, no. 3, p. 242, 1984.

[58] S. Mishra, S. H. Sonawane, and R. P. Singh, "Studies on characterization of nano $CaCO_3$ prepared by the in situ deposition technique and its application in PP-nano $CaCO_3$ composites," Journal of Polymer Science Part B: Polymer Physics, vol. 43, no. 1, pp. 107–113, 2005.

[59] Z. K. Zhu, Y. Yang, J. Yin, and Z. N. Qi, "Preparation and properties of organosoluble polyimide/silica hybrid materials by sol–gel process," Journal of Applied Polymer Science, vol. 73, no. 14, pp. 2977–2984, 1999.

[60] M. Wang, C. Berry, M. Braden, and W. Bonfield, "Young's and shear moduli of ceramic particle filled polyethylene," Journal of Materials Science and Materials in Medicine, vol. 9, no. 11, pp. 621–624, 1998.

[61] E. Reynaud, T. Jouen, C. Gauthier, G. Vigier, and J. Varlet, “Nanofillers in polymeric matrix: a study on silica reinforced PA6,” Polymer, vol. 42, no. 21, pp. 8759–8768, 2001.

[62] M. Abu-Abdeen, “Static and dynamic mechanical properties of poly(vinyl chloride) loaded with aluminum oxide nanopowder,” Materials & Design, vol. 33, no. 0, pp. 523–528, 2012.

[63] H. S. Jaggi, Y. Kumar, B. K. Satapathy, A. R. Ray, and A. Patnaik, “Analytical interpretations of structural and mechanical response of high density polyethylene/hydroxyapatite bio-composites,” Materials & Design, vol. 36, no. 0, pp. 757–766, 2012.

[64] S. Areerat, Y. Hayata, R. Katsumoto, T. Kegasawa, H. Egami, and M. Ohshima, “Solubility of carbon dioxide in polyethylene/titanium dioxide composite under high pressure and temperature,” Journal of Applied Polymer Science, vol. 86, no. 2, pp. 282–288, 2002.

[65] G. Dlubek, U. De, J. Pionteck, N. Y. Arutyunov, M. Edelmann, and R. Krause-Rehberg, “Temperature dependence of free volume in pure and silica-filled poly(dimethyl siloxane) from positron lifetime and PvT experiments,” Macromolecular Chemistry and Physics, vol. 206, no. 8, pp. 827–840, 2005.

[66] V. L. Carrubba, M. Bulters, and W. Zoetelief, “Dependence of coefficient of volumetric thermal expansion (CVTE) of glass fiber reinforced (GFR) polymers on the glass fiber content,” Polymer Bulletin, vol. 59, no. 6, pp. 813–824, 2008.

[67] J. Lenz, R. K. Enneti, V. P. Onbattuvelli, K. Kate, R. Martin, and S. V. Atre, " Powder injection molding of ceramic engine components for transportation," JOM, vol. 64, pp. 388-392, 2012.

[68] R. K. Enneti, S. J. Park, J. Palagi de Souza, and S. V. Atre, "Critical issues in manufacturing dental brackets by powder injection molding," International Journal of Powder Metallurgy, , vol. 48, no. 2, pp. 23-29, 2012.

Chapter 3

Measurements of Powder-Polymer Mixture Properties and Their Use in Powder Injection Molding Simulations for Aluminum Nitride

3.1 Abstract

Aluminum nitride has been favored for applications in manufacturing substrates for heat sinks due to its elevated temperature operability, high thermal conductivity and low thermal expansion coefficient. Powder injection molding is a high-volume manufacturing technique that can translate these useful material properties into complex shapes. In order to design and fabricate components from aluminum nitride it is important to know the injection molding behavior at different powder-binder compositions. However, the lack of a materials database for design and simulation at different powder-polymer compositions is a significant barrier. In this paper, a database of rheological and thermal properties for aluminum nitride-polymer mixtures at various volume fractions of powder was compiled from experimental measurements. This database was used to carry out mold-filling simulations to understand the effects of powder content on the process parameters and defect evolution during the injection molding process. The experimental techniques and simulation tools can be used to design new materials, select component geometry attributes, and optimize process parameters while eliminating expensive and time-consuming trial-and-error practices prevalent in the area of powder injection molding.

3.2 Introduction

Powder injection molding (PIM) is useful to economically net-shape complex ceramic and metal components at high production volumes. In PIM, ceramic or metal powder is compounded with polymer (binder) and used to mold parts with an injection-molding machine, in a manner analogous to the fabrication of conventional thermoplastics. Subsequently, the polymer is removed (debinding) from the molded part and then sintered under controlled time, temperature and atmospheric conditions to get the final part of desired dimensions, density, microstructure and properties. Due to the requirement for several subsequent processing steps it is essential to identify appropriate powder-binder mixture (feedstock) compositions and processing conditions that will result in obtaining parts that are free of defects such as weld-lines, internal stresses, cracks and warpage during the injection molding stage. One common approach to resolve precision and defect avoidance issues during manufacturing is to lower the amount of powder in the powder-polymer mixture to improve the mold filling attributes and increase the green strength during ejection of the part from the mold. However, the volume fraction of powder not only affects powder-polymer mixture properties and molding behavior but also the debinding and sintering conditions as well as the final dimensions of the part.

Equation 3.1 provides the final dimensions of the sintered part based on the initial volume fraction of powder, ϕ_p [1]:

$$Y = 1 - \left(\frac{\emptyset_p}{f_s}\right)^{1/3} \tag{3.1}$$

where, Y is the linear shrinkage factor and f_s is the fractional sintered density. This inter-relationship between component shrinkage, sintered density and initial volume fraction of powder is shown in **Figure 3.1**. It can be seen that parts with lower volume fraction of powder in the feedstock undergo larger shrinkage for a given sintered density. Sintering to lower final density is typically not an option since structural and functional properties depend on achieving high sintering densities. Alternatively, mold cavity dimensions can be changed to achieve the desired sintered dimensions but that would involve expensive and time-consuming tool rework. Therefore, there is a critical need to address the effects

of feedstock composition on the injection molding attributes and defect avoidance at the component design stage itself.

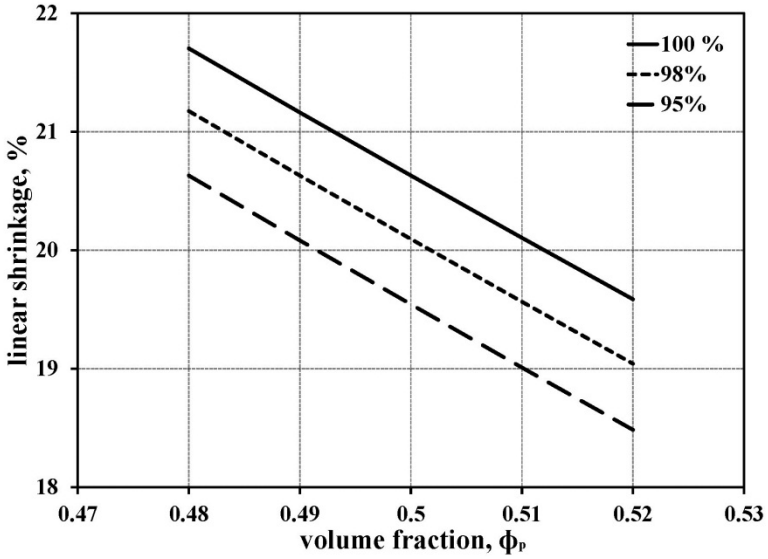

Figure 3.1: Dependence of linear shrinkage on final sintered density and different volume fractions of powder, ϕ_p, using Equation 3.1.

Several injection molding simulation platforms are available for addressing the above design challenges in PIM. In order to facilitate the design of PIM components using such simulation tools, there is a critical need to determine the effects of variation in material composition on the thermal, rheological and mechanical properties of powder-polymer mixtures. The experimental data that are typically required for powder-polymer mixtures at high volume fractions of powder are limited in the literature and also tend to be expensive to obtain for specific volume fractions of powder.

In order to understand the effects of compositional change on powder-polymer mixture properties, empirical models that have a limited number of fitting constants to predict feedstock properties were evaluated and used in the current study using aluminum nitride (AlN) PIM feedstocks. The approach involved using experimental property data of the unfilled polymer and a powder-polymer mixture at 0.52 volume fraction AlN powder in

conjunction with the selected mixing models to model a number of physical properties over a range of powder volume fractions in the feedstock. The modeled data thus generated were used as input into a feedstock property file in the Autodesk Moldflow Insight software for simulating the injecting molding process. These simulations were used to understand the sensitivity of feedstock composition and consequently, physical properties on the injection molding behavior and defect evolution in AlN components. It is anticipated that the experimental techniques and modeling and simulation tools presented in this study can be generalized to design new materials, select component geometry attributes, and optimize process parameters while eliminating expensive and time-consuming trial-and-error practices prevalent in PIM.

3.3 Experimental Materials and Methods

Commercially available AlN (D_{50} ~1 μm) and Y_2O_3 (D_{50} ~50 nm) were used as the starting materials in as-received condition. The micrographs of the powder was taken with the QuantaTM –FEG (FEI) dual beam scanning electron microscope (SEM) coupled with an energy dispersive X-ray spectrometer (EDAX) and is shown in **Figure 3.2**.

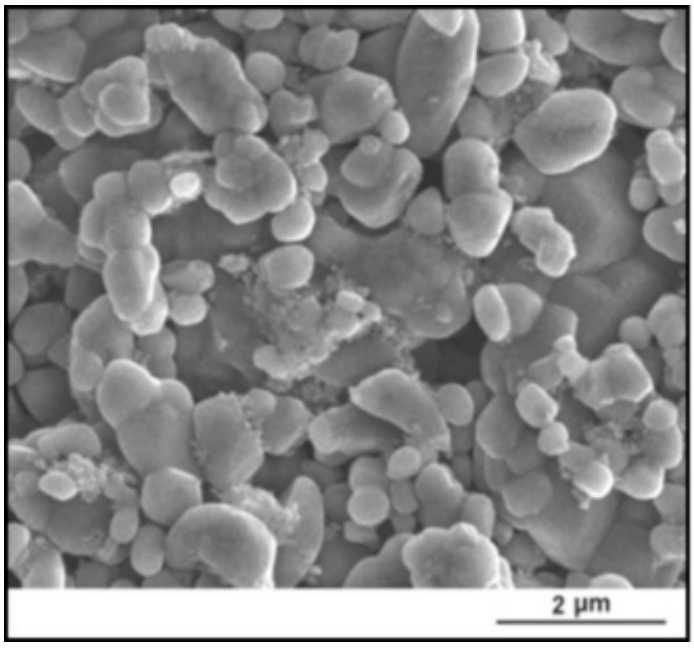

Figure 3.2: SEM image of AlN powder used in this study.

5 wt.% Y_2O_3 was added on the basis of AlN to the powder mixture. A multi-component binder system comprising of paraffin wax (PW), polypropylene (PP), polyethylene-g-maleic anhydride (LDPE-g-MA) and stearic acid (SA) was used in the current study. Details of the composition and mixing preparations are provided elsewhere [2]. Torque rheometry was performed in the Intelli-Torque Plasticorder (Brabender) in order to determine the maximum packing density of the powder-polymer mixture. Twin screw extrusion of AlN feedstocks was performed with an Entek co-rotating 27 mm twin screw extruder with an L/D ratio of 40 and pelletized for further use. Injection molding was performed on an Arburg 221M injection molding machine. Thermogravimetric analysis (TGA) was performed on the extruded feedstocks using TA- Q500 (TA instruments) thermal system operated under nitrogen flow in the temperature range of 50-600°C with a heating rate of 20 °C/min in order to confirm the powder weight fraction in the feedstock.

The rheological characteristics of the feedstock were examined on a Gottfert Rheograph 2003 capillary rheometer at different shear rates and temperatures. The testing was carried out in accordance with ASTM D 3835. The temperatures were between the highest melting temperature and the lowest degradation temperature of the binder system. The barrel of inner diameter of 1 mm and die length of 20 mm was used. The preheating time was kept at 6 minutes. A K-System II Thermal Conductivity System was used to evaluate the thermal conductivity of the feedstock. The testing was carried out in accordance with ASTM D 5930. The initial temperature was 190^{o}C and final temperature was 30^{o}C. The probe voltage was kept at 4 V and acquisition time of 45 s. Specific heat measurements were carried out on Perkin Elmer DSC7 equipment in accordance with ASTM E 1269. The testing was done with an initial temperature of 190^{o}C and final temperature of 20^{o}C. The cooling rate was kept constant of 20^{o}C/minute. A Gnomix PVT apparatus was used to find the PVT relationships of the feedstock materials. The test was carried out in accordance with ASTM D 792. The pellets were dried for 4 hours at 70^{o}C under vacuum. The measurement type used was isothermal heating scan with a heating rate of approximately 3^{o}C/minute.

Autodesk Moldflow Insight 2010 software was used for simulating the injection conditions of two heat sink geomteries. The heat sink geometries were built using Autodesk Solidworks 2011 software and the geometry was imported in Moldflow Insight software. The part was meshed using an automated solid 3D meshing which makes use of finite element analysis for meshing. The process settings were 303 K for the mold temperature and 433 K for the melt temperature. Simulations were conducted for a fill-and-pack type condition in order to meet the objective of understanding injection molding behavior and its packing characteristics.

3.4 Estimating Properties of Powder-Polymer Mixtures:

The experimentally determined physical properties of AlN powder-polymer mixtures at 0 and 0.52 volume fraction were used to estimate properties of AlN powder-polymer mixtures with 0.48 to 0.51 volume fractions. In order to estimate these properties, various models were initially screened before choosing models that were specific to estimating material properties at high volume fraction fillers. Further, models having fewer empirical constants were preferred over alternatives, when necessary. Additionally, the viscosity and PVT data required curve fitting to extract constants required for the simulations using Autodesk Moldflow Insight software.

3.4.1 Density

The melt and solid density of powder-polymer mixtures can be estimated using various models [3, 4]. In this paper, an inverse rule-of-mixtures was used [4] as given in **Equation 3.2:**

$$\frac{1}{\rho_c} = \frac{X_b}{\rho_b} + \frac{X_p}{\rho_p} \tag{3.2}$$

where, ρ is the density, X is the mass fraction and the subscripts c, b and p stand for the composite, binder and powder respectively. Further, the mass fractions for powder and binder can be calculated using **Equation 3.3:**

$$X_p = \frac{\phi_p \rho_p}{\phi_p \rho_p + \phi_b \rho_b} \qquad X_b = \frac{\phi_b \rho_b}{\phi_p \rho_p + \phi_b \rho_b} \tag{3.3}$$

where ϕ is the volume fraction of the powder. A comparison of density as a function of volume fraction of powder is shown in **Table 3.1.**

Table 3.1: Comparison of melt and solid densities for different volume fractions of AlN powder, ϕ_p.

volume fraction, Φ_p	melt density, kg/m^3	solid density, kg/m^3
0	**727**	**879**
0.48	1873	2128
0.49	1897	2152
0.5	1921	2177
0.51	1945	2201
0.52	**1969**	**2225**

The melt and solid density data for 0 and 0.52 volume fractions, Φ_p were experimentally obtained while the values for intermediate volume fractions were estimated using **Equation 3.2.** It was observed that for a change from 0.48 to 0.52 volume fraction of AlN, the melt density increased from 727 to 1969 kg/m^3 and solid density increased from 879 to 2252 kg/m^3. The data in **Table 3.1** indicates a ±2 % variation in melt and solid density as a result of a ±4% change in the volume fraction of AlN.

3.4.2 Specific heat

The specific heat of powder-polymer mixtures has been be estimated by different mixing rules [5–8]. In this study, a model that has been successfully applied to mixtures with high volume fraction fillers [6], was used as shown in **Equation 3.4:**

$$C_{p_c} = \left[C_{p_b} X_b + C_{p_p} X_p\right] * \left[1 + A * X_b X_p\right] \tag{3.4}$$

where, C_p is the specific heat, X is the mass fraction and the subscripts c, b and p stand for the composite, binder and powder respectively. The parameter, A, is a correction factor assumed to be 0.2 for spherical particles. The mass fractions were calculated using

Equation 3.3. The specific heat values calculated for different volume fractions of powder at various temperatures are shown in **Table 3.2.**

Table 3.2: Specific heat capacity values at various temperatures for different volume fractions of AlN powder, ϕ_p.

volume fraction, Φ_p	temperature, K						
	283	298	304	322	331	374	423
	specific heat capacity C_p, J/kg-K						
0	**2080**	**3360**	**3840**	**4900**	**4640**	**3490**	**2530**
0.48	960	1190	1460	2890	1200	1200	1260
0.49	950	1170	1440	2870	1170	1180	1250
0.5	940	1150	1420	2850	1150	1160	1230
0.51	930	1130	1400	2830	1120	1140	1220
0.52	**920**	**1110**	**1380**	**2810**	**1090**	**1130**	**1210**

The specific heat data for 0 and 0.52 volume fractions were experimentally obtained while the values for intermediate volume fractions were estimated using **Equation 3.4.** It was observed that the specific heat of the powder-polymer mixtures decreased with an increase in volume fraction of powder. It was also observed that the specific heat increased with increase in temperature and reached a maximum at a transition temperature beyond which it again reduces. As a specific example, a change of volume fraction from 0.48 to 0.52 at 374 K resulted in a decrease in specific heat from 1200 to 1130 J/g-K. The data in **Table 3.2** indicates that a ± 2.5 % change in specific heat results from a ± 4 % change in the volume fraction of AlN.

3.4.3 Thermal conductivity

Several equations have been used to predict thermal conductivity of a composite at different filler concentrations [5, 9, 10]. In this paper, a general rule-of-mixtures model [4] was used as represented in **Equation 3.5**:

$$\lambda_c = \lambda_b \phi_b + \lambda_p \phi_p \tag{3.5}$$

where, λ is the thermal conductivity, ϕ is the volume fraction of powder and the subscripts c, b and p stand for the composite, binder and powder respectively. The

estimated values of thermal conductivity as a function of volume fraction of powder at various temperatures are shown in **Table 3.3.**

Table 3.3: Thermal conductivity for different volume fractions of AlN powder, ϕ_p.

volume fraction, Φ_p	temperature, K						
	315	336	356	377	397	417	436
	thermal conductivity, W/m·K						
0	**0.195**	**0.188**	**0.182**	**0.176**	**0.171**	**0.166**	**0.162**
0.48	3.95	3.55	2.08	2.47	1.91	1.90	2.32
0.49	4.03	3.62	2.52	2.71	1.95	1.94	2.37
0.5	4.11	3.69	2.16	2.57	1.99	1.97	2.41
0.51	4.18	3.76	2.19	2.61	2.02	2.01	2.46
0.52	**4.26**	**2.37**	**2.23**	**2.41**	**2.22**	**2.2**	**2.7**

The thermal conductivity data for 0 and 0.52 volume fractions were experimentally obtained while the data for intermediate volume fractions were estimated using **Equation 3.5.** The values of thermal conductivity are similar to studies by Mamunya *et al* [11] for AlN-epoxy composites at powder content of 0.4-0.5 volume fractions. It can be seen that the thermal conductivity increases with an increase in volume fraction of AlN powder, Φ_p. Additionally, a decrease in the thermal conductivity value is observed when the temperature increases above glass transition. The data presented in Table 4 indicate that a ± 4 % variation in thermal conductivity results from a ± 4% change in volume fraction of AlN.

3.4.4 Coefficient of thermal expansion

The coefficient of thermal expansion (CTE) of powder-polymer mixtures can be calculated by several models [8, 9, 12, 13]. In this paper first order model was used [9] as shown in **Equation 3.6** since fewer empirical constants were required.

$$\alpha_c = X_p \alpha_p + \alpha_b (1 - X_p) \tag{3.6}$$

where, α is the thermal expansion coefficient, X is the mass fraction of the powder and the subscripts c, p and b stands for composite, powder and binder respectively. The CTE data are as shown in **Table 3.4.**

Table 3.4: Coefficient of thermal expansion for different volume fractions of AlN powder, ϕ_p.

volume fraction, Φ_p	CTE, K^{-1}
0	**5.65E-05**
0.48	2.28E-05
0.49	2.25E-05
0.5	2.23E-05
0.51	2.20E-05
0.52	**2.18E-05**

The CTE data at 0 and 0.52 volume fractions AlN were experimentally obtained while the rest were estimated using **Equation 3.6**. It can be seen that the CTE value decreases with an increase in volume fraction of AlN. Typically in the range of 0.48 to 0.52 volume fractions, ϕ_p, the CTE varied between 2.28 E-5 to 2.18 E-5 K^{-1} which represents a ± 3 % variation in CTE for a ± 4% change in volume fraction of AlN in the powder-polymer mixtures.

3.4.5 Elastic and shear modulus

In this paper, the Voigt model [9] was used to predicting the elastic and shear modulus as shown in **Equation 3.7:**

$$E_c = E_p X_p + E_b(1 - X_b) \tag{3.7}$$

where, E is the elastic or shear modulus and subscripts c, p and b represent composite, powder and binder respectively. X is the mass fraction and is calculated using **Equation 3.3**. **Table 3.5** shows the elastic and shear modulus values estimated at different volume fractions of powder.

Table 3.5: Elastic and shear modulus values for different volume fractions of AlN powder, ϕ_p.

volume fraction, Φ_p	elastic modulus, MPa	shear modulus, MPa
0	**2560**	**930**
0.48	13050	4900
0.49	13270	5000
0.5	13480	5070
0.51	13700	5150
0.52	**13920**	**5240**

The modulus data for powder volume fractions of 0 and 0.52 were experimentally obtained while the values for the intermediate volume fractions were estimated using **Equation 3.7**. It can be seen that the elastic and shear modulus values increase with an increase in volume fractions of AlN. Typically, in the range of 0.48 to 0.52 volume fractions, ϕ_p, the elastic modulus increased between ~13000 to ~14000 MPa and shear modulus varies between 4900 to 5240 MPa which represents a ± 3.5 % variation in the elastic and shear modulus for a ± 4% change in volume fraction of AlN in the powder-polymer mixtures.

3.4.6 Viscosity

The viscosity of powder-polymer mixtures at different volume fractions of AlN can be predicted using numerous mixing rules [4, 14-16]. In this paper, a simplified Krieger-Dougherty [16] viscosity model was used as it is suitable for predicting viscosity values at higher volume fractions of powder using the fewest empirical constants, as given in **Equation 3.8:**

$$\eta_c = \frac{\eta_b}{\left[1 - \frac{\phi_p}{\phi_{max}}\right]^2} \tag{3.8}$$

where, η and ϕ_p represent the viscosity and the volume fraction of powder, respectively while the subscripts c and b represent composite and binder respectively. The parameter, ϕ_{max}, stands for the maximum packing fraction of the powder. Additionally, the Cross-WLF model [17] was used to model the viscosity dependence of any given powder-polymer mixture on shear rate as shown in **Equation 3.9**:

$$\eta = \frac{\eta_0}{1 + \left(\frac{\eta_0 \gamma}{\tau^*}\right)^{1-n}} \tag{3.9}$$

where, η is the melt viscosity (Pa-s), η_0 is the zero shear viscosity, γ is the shear rate (1/s), τ^* is the critical stress level at the transition to shear thinning, determined by curve fitting, and n is the power law index in the high shear rate regime, also determined by curve fitting. The temperature dependence of viscosity of any powder-polymer mixture [17] can be calculated using **Equation 3.10:**

$$\eta_0 = D_1 exp\left[-\frac{A_1(T - T^*)}{A_2 + (T - T^*)}\right] \quad (3.10)$$

where, T is the temperature (K). T^*, D_1 and A_1, are curve fitted coefficients. Additionally, A_2 is the WLF constant and is assumed to be 51.6 K. The values of these coefficients were obtained by curve-fitting the estimated viscosity for different volume fractions of powder at various shear rates and temperatures and are summarized in **Table 3.6.**

Table 3.6: Cross-WLF constants for different volume fractions of AlN powder, ϕ_p.

Cross WLF constants	volume fraction, Φ_p					
	0	**0.48**	**0.49**	**0.5**	**0.51**	**0.52**
n	**0.4**	0.46	0.46	0.45	0.43	**0.38**
τ, Pa	**793.46**	280.12	230.58	183.65	148.20	**117.77**
D1, Pa·s	**4.29E+23**	8.73E+10	9.66E+10	1.81E+11	8.46E+10	**8.78E+10**
T*, K	**333**	375.15	374.68	372.29	370.45	**263.15**
A1	**78.13**	31.13	31.12	30.24	26.13	**14.23**
A2, K	**51.6**	51.6	51.6	51.6	51.6	**51.6**

Figure 3.3 shows the shear-rate dependence of viscosity for several powder-polymer mixtures at 413 and 433 K. The zero-shear viscosity was estimated from the plateau region at low shear rate while the power law index was obtained from the slope at higher shear rates. The data for powder volume fractions of 0 and 0.52 are experimental values while the data for intermediate volume fractions of powder were estimated from **Equation 3.8**. It can be observed that the zero-shear viscosity increased considerably with small increases in volume fraction, ϕ_p, in the range of interest. The curve-fitted WLF parameters n, τ^*, D_1, T^*, A_1 and A_2 were estimated for temperatures between 413 K and 433 K. The values estimated for n and τ^* for each temperature were then averaged out for individual volume fractions of powder which resulted in an error of ± 1.5 %. The values of rest of the parameters did not vary with an increase in temperature. The power law index, n, decreased from 0.46 to 0.38 with an increase in volume fractions from 0.48 to 0.52. Similarly, τ^* decreased from 280 to 118 MPa with an increase in volume fractions from 0.48 to 0.52.

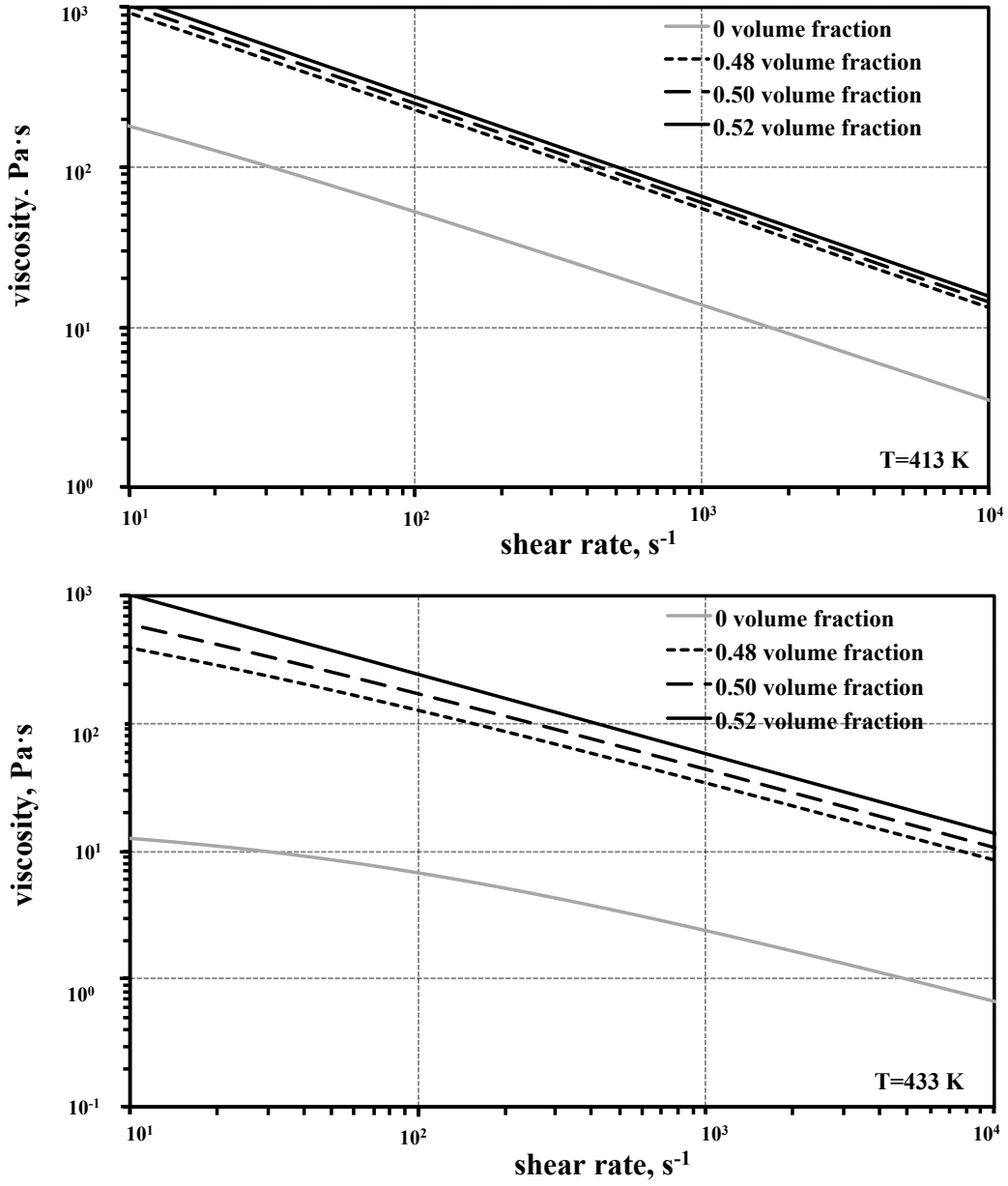

Figure 3.3: Comparison of viscosity with shear rate at 413 K (top) and 433 K (bottom) for different volume fractions of AlN powder, ϕ_p.

T^* is the transition temperature at which the material exhibits a change from Newtonian to shear-thinning behavior on increasing shear rates. It was observed that the value of T^* decreased from 370 K to 263 K when the volume fraction of AlN was changed from 0.48

to 0.52. It was also observed, that A_1 changed from 31 to 14 when the volume fraction of AlN was changed from 0.48 to 0.52.

3.4.7 Specific volume

The specific volume was calculated using the general rule-of-mixtures [4] given in **Equation 3.11:**

$$\upsilon_c = X_p \upsilon_p + \upsilon_b(1 - X_f) \tag{3.11}$$

where, υ is the specific volume, X is the mass fraction of the powder and the subscripts c, p and b refer to the composite, powder and binder respectively. The injection molding software platform uses the two-domain Tait [18] equation **(Equation 3.12)** for generating viscosity values at different volume fractions of powder.

$$\upsilon(T,p) = \upsilon_o(T)\left[1 - Cln\left(1 + \frac{p}{B(T)}\right) + \upsilon_t(T,p)\right] \tag{3.12}$$

where, υ (T,p) is the specific volume at a given temperature and pressure, υ_o is the specific volume at zero gauge pressure, T is temperature in K, p is pressure in Pa, and C is a constant assumed as 0.0894. The parameter, B, accounts for the pressure sensitivity of the material and is separately defined for the solid and melt regions. For the upper bound [18] when $T > T_t$ (volumetric transition temperature), B is given by **Equation 3.13:**

$$\upsilon_o = b_{1m} + b_{2m}(T - b_5)B(T) = b_{3m}e^{[-b_{4m}(T-b_5)]}\upsilon_t(T,p) = 0 \tag{3.13}$$

where, b_{1m}, b_{2m}, b_{3m}, b_{4m}, and b_5 are curve-fitted coefficients. For the lower bound [18], when $T < T_t$, the parameter, B, is given by **Equation 3.14:**

$$\upsilon_o = b_{1s} + b_{2s}(T - b_5)B(T) = b_{2s}e^{[-b_{4s}(T-b_5]}\upsilon_t(T,p) = b_7 e^{[b_8(T-b_5)-(b_9 p)]} \tag{3.14}$$

where, b_{1s}, b_{2s}, b_{3s}, b_{4s}, b_5, b_7, b_8, and b_9 are curve-fitted coefficients. The dependence of the volumetric transition temperature, T_t on pressure can be given by $T_t(p) = b_5 + b_6(p)$, where b_5 and b_6 are curve-fitted coefficients. The values of these coefficients are summarized in **Table 3.7.**

Table 3.7: Dual-domain Tait constants for different volume fractions of AlN powder, ϕ_p.

Dual-domain Tait constants	volume fraction, Φ_p					
	0	**0.48**	**0.49**	**0.5**	**0.51**	**0.52**
b5, K	**336.15**	331	331	331	331	**331**
b6, K/Pa	**1.47E-07**	1.65E-07	1.65E-07	1.65E-07	1.65E-07	**1.65E-07**
b1m, m^3/kg	**1.26E-03**	5.07E-04	5.00E-04	4.95E-04	4.90E-04	**4.84E-04**
b2m, m^3/kg·K	**1.34E-06**	3.37E-07	3.27E-07	3.18E-07	3.09E-07	**2.99E-07**
b3m, Pa	**1.26E+08**	2.71E+08	2.71E+08	2.71E+08	2.87E+08	**2.87E+08**
b4m, K^{-1}	**5.87E-03**	4.88E-03	4.88E-03	4.88E-03	2.49E-03	**4.82E-03**
b1s, m^3/kg	**1.17E-03**	4.92E-04	4.84E-04	4.75E-04	4.74E-04	**4.69E-04**
b2s, m^3/kg·K	**8.57E-07**	1.82E-07	1.71E-07	1.65E-07	1.47E-07	**9.70E-08**
b3s, Pa	**2.40E+08**	5.79E+08	5.79E+08	5.79E+08	5.79E+08	**5.79E+08**
b4s, K^{-1}	**4.16E-03**	1.26E-03	1.26E-03	1.26E-03	1.26E-03	**1.26E-03**
b7, m^3/kg	**8.46E-05**	3.23E-06	7.78E-06	1.04E-05	7.27E-06	**1.49E-05**
b8, K^{-1}	**6.69E-02**	4.50E-02	3.99E-02	1.85E-02	5.33E-02	**1.10E-01**
b9, Pa^{-1}	**1.39E-08**	2.12E-08	2.12E-08	2.12E-08	2.12E-08	**2.12E-08**

Figure 3.4 shows the comparative plot of specific volumes at 0, 100, and 200 MPa pressure. The PVT behavior for 0.52 volume fraction of powder is plotted from experimental values while the data for 0.48 and 0.50 volume fractions of powder were estimated using **Equation 10**. It can be observed that the specific volume increases with an increase in volume fraction of AlN. The dual-domain Tait constants were estimated using curve fitting for 0, 50, 100, 150, 200 MPa pressure for volume fractions of 0, 0.48 to 0.52 AlN. The parameters, b_5 b_6, and b_9, did not vary in the range of 0.48 to 0.52 volume fractions of AlN. It was also observed that the parameters, b_{1m}, b_{2m}, b_{1s} and b_{2s}, decreased on increasing the volume fractions from 0.48 to 0.52 but the change was nominal. The parameters, b_{3m}, b_{4m}, b_{3s} and b_{4s}, also did not vary for volume fractions between 0.48 to 0.52. Parameters, b_7 and b_8, showed a relatively greater sensitivity to changes in the volume fraction of AlN, however no distinctive trends could be observed.

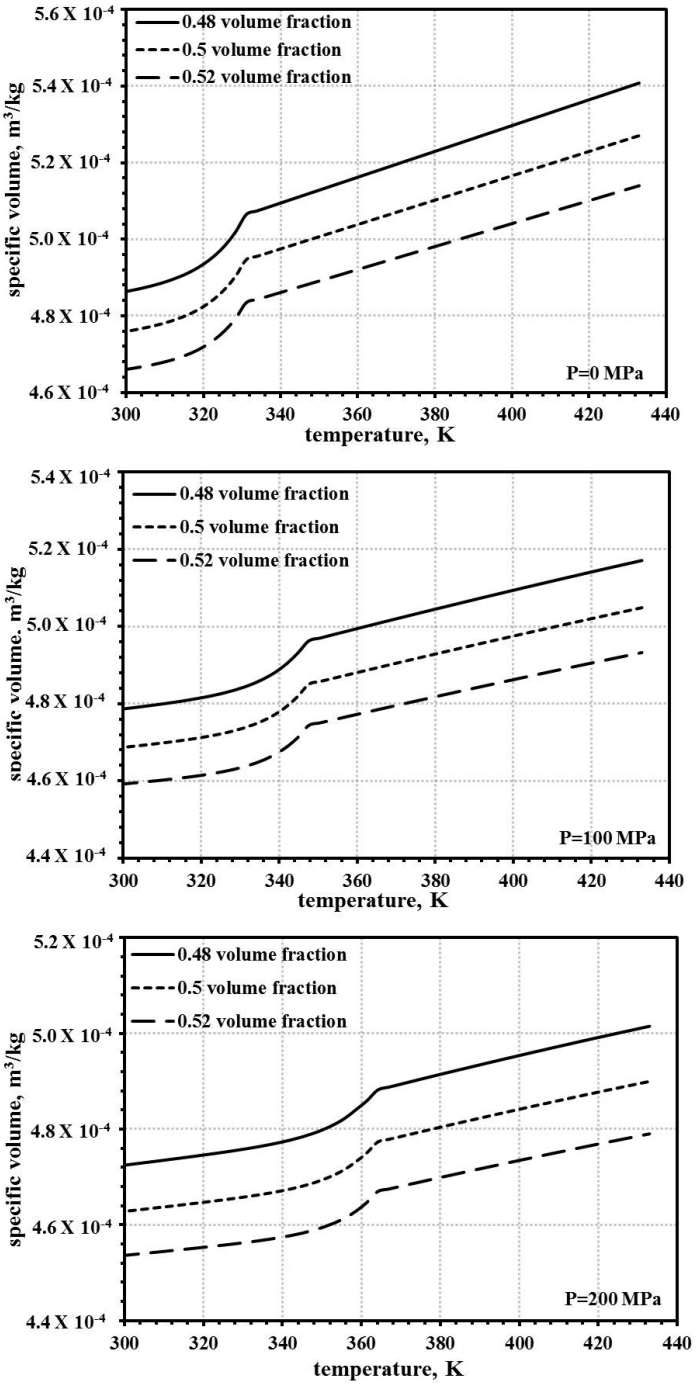

Figure 3.4: PVT behavior for 0, 100, and 200 MPa pressures for different volume fractions of AlN powder, ϕ_p.

3.5 Simulation Results

Simulations were conducted for 0.48 to 0.52 volume fractions of AlN at 433 K melt temperature and 303 K mold temperatures using the heat-sink geometries shown in **Figure 3.5.**

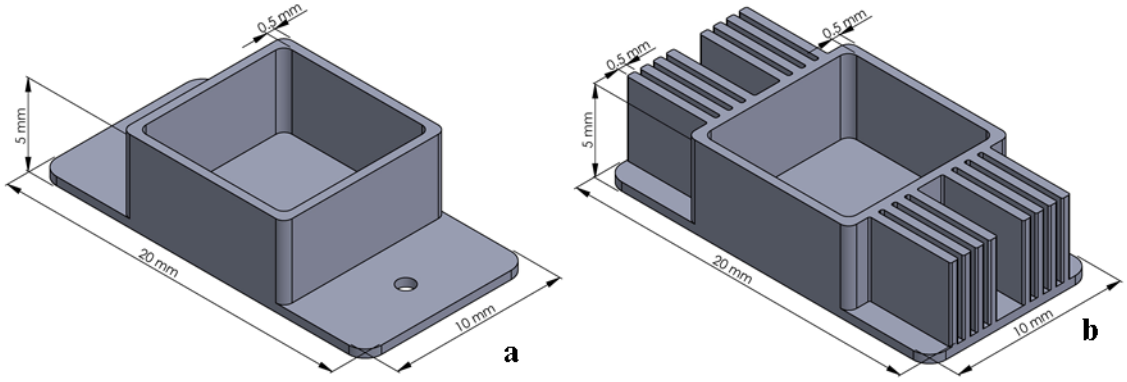

Figure 3.5: Mold geometry used in injection molding simulations: a) simple heat-sink substrate without fins, and b) heat sink substrate with fins.

The simulations were done for mold filling and packing stages. The progressive filling behavior of the feedstock with 0.51 volume fraction AlN is shown in **Figure 3.6** for the two geometries. It can be seen that the fin region of the mold cavity fills at the end of the molding stage.

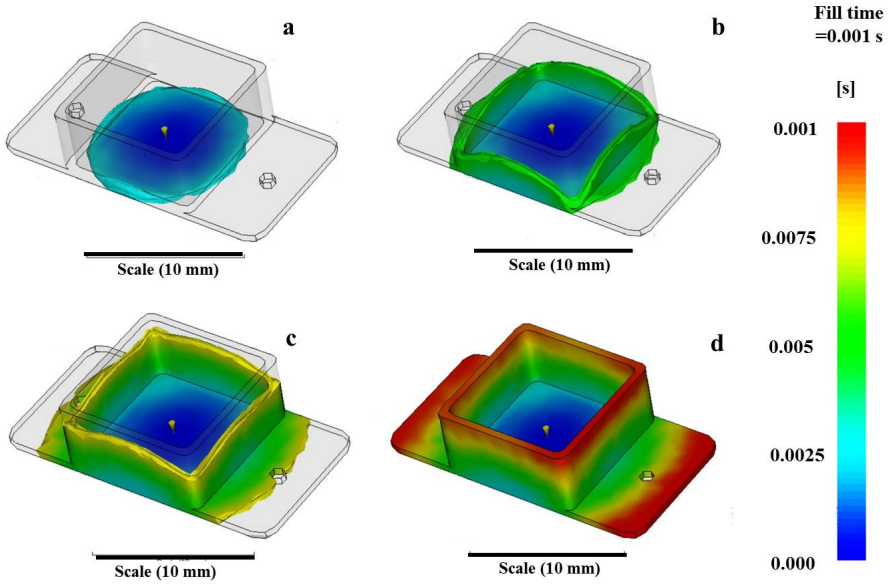

Figure 3.6A: Progressive filling of the heat sink substrate without fins shown in Figure 5A for 0.51 volume fraction AlN feedstock: (a) 25% fill, (b) 50% fill, (c): 75% fill and (d) 100% fill.

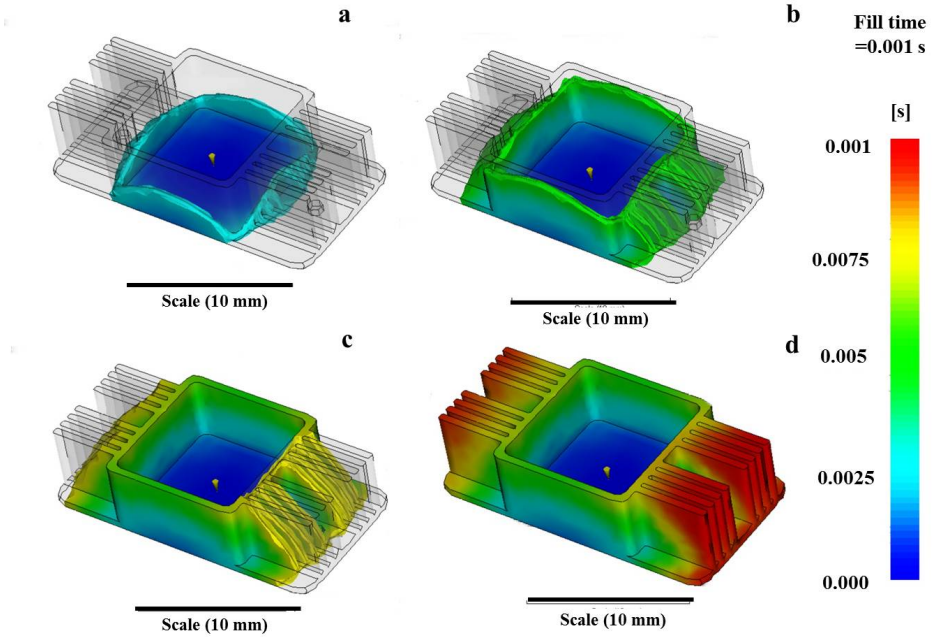

Figure 3.6B: Progressive filling of the heat sink substrate with fins shown in Figure 5B for 0.51 volume fraction AlN feedstock: (a) 25% fill, (b) 50% fill, (c): 75% fill and (d) 100% fill.

Figure 3.7 shows the variation of part weight as a function of volume fraction of AlN for the two heat-sink geometries shown in **Figure 3.5**. The part weight increases with an increase in volume fraction of AlN powder from 0.48 to 0.52.

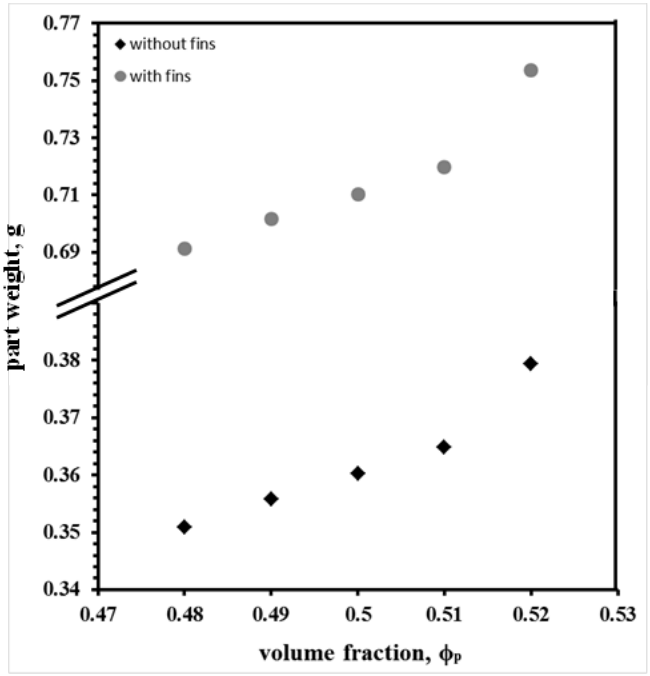

Figure 3.7: Part weight for different volume fractions of AlN powder, ϕ_p.

This increase in part weight with an increase in powder volume fraction can be attributed to an increase in density values with a rise in volume fractions of AlN as observed in **Table 3.1.** Further, for an AlN powder volume fraction change from 0.48 to 0.52, the part weight changes from 0.35 to 0.38 g for heat sink substrate without fins. In the case of the heat sink substrate with fins, the corresponding change is from 0.69 to 0.76 g. This change denotes a ±3 % variation in part weight for a ± 4% change in the volume fraction of AlN. It was also observed that the part weight doubled for heat sink substrate with fins in comparison to the heat sink substrates without fins in **Figure 3.7**

As the filling phase nears completion, the packing phase commences during which the part cools till a 100 % frozen volume is obtained. **Figure 3.8** shows the dependence on freeze time on the volume fraction of AlN powder in the feedstock.

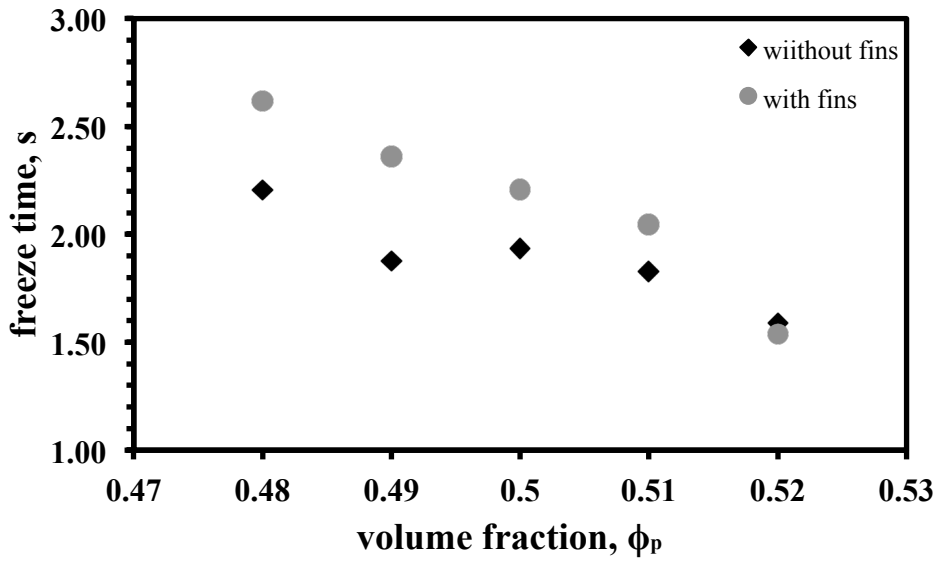

Figure 3.8: Freeze time for different volume fractions of AlN powder, ϕ_p.

It can be observed from **Figure 3.8** that for a change of 0.48 to 0.52 volume fractions of AlN, the freeze time changes from 2.2 to 1.6 s for heat sink substrate without fins. In the case of the heat-sink substrate with fins, the change in freeze time is from 2.6 to 1.6 s. This denotes a ± 2.5 % variation in freeze time for a ± 4% change in the volume fraction of AlN. The change in freeze time as a function of volume fraction can be attributed to the change in thermal properties estimated from **Equations 3.4** and **3.5**.

Figure 3.9 shows the variation in peak injection pressure as a function of the volume fraction of powder for the two heat-sink substrates. The peak injection pressure is located near the gate of the mold cavity. The peak injection pressure is relatively higher for the heat-sink substrate with fins compared to the heat-sink substrate without fins as a result of an increase in volumetric flow rate. It can be seen that for the heat-sink substrate with fins, the peak injection pressure increases from ~14 to ~16 MPa with an increase in powder volume fraction from 0.48 to 0.52. This behavior can be attributed to an increase in the viscosity of the powder-polymer mixture as represented in **Equations 3.8-3.10**. An increase in injection pressure directly increases the clamp force and correspondingly

reduces the number of mold cavities that can be simultaneously filled on a molding machine.

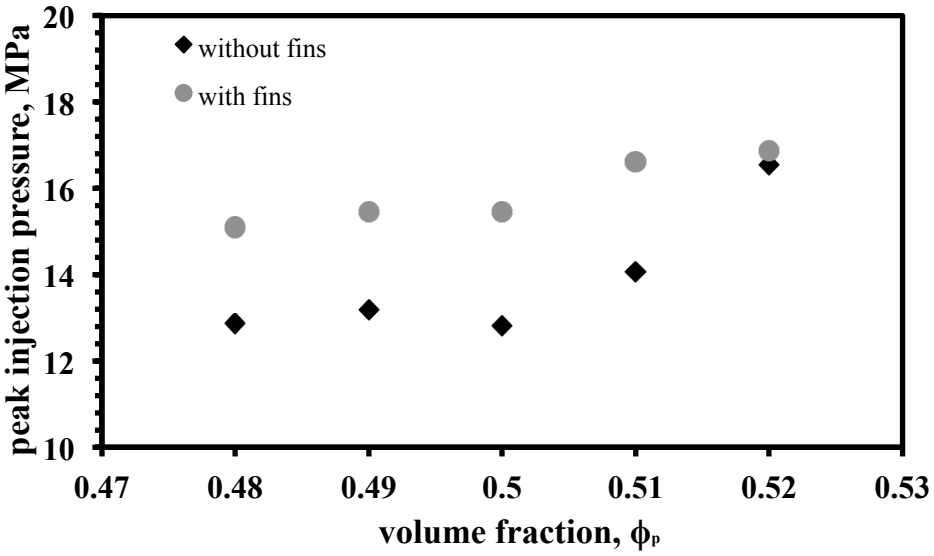

Figure 3.9: Peak injection pressure for different volume fractions of AlN powder, ϕ_p.

An increase in injection pressure can also result in an undesirable alteration of the melt flow such as jetting. Further, microstructural inhomogeneity can also be introduced in the part at higher injection pressures due to powder-polymer separation.

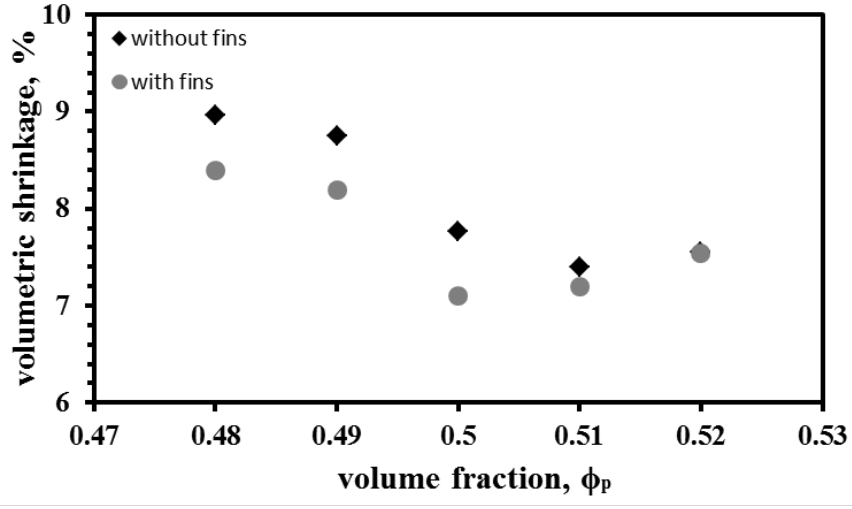

Figure 3.10: Volumetric shrinkage (%) for different volume fractions of AlN powder, ϕ_p.

Figure 3.10 shows the dependence of volumetric shrinkage of the heat-sink substrates as a function of powder volume fraction. It can be seen that the volumetric shrinkage generally decreases from ~8.5 to ~7 % with increase in powder volume fraction from 0.48 to 0.52. This can be attributed to the PVT behavior of the powder-polymer mixtures as described in **Equations 3.11-3.14**.

Figure 3.11 shows the weld-line distribution for the two heat-sink substrates as a function of powder volume fraction.

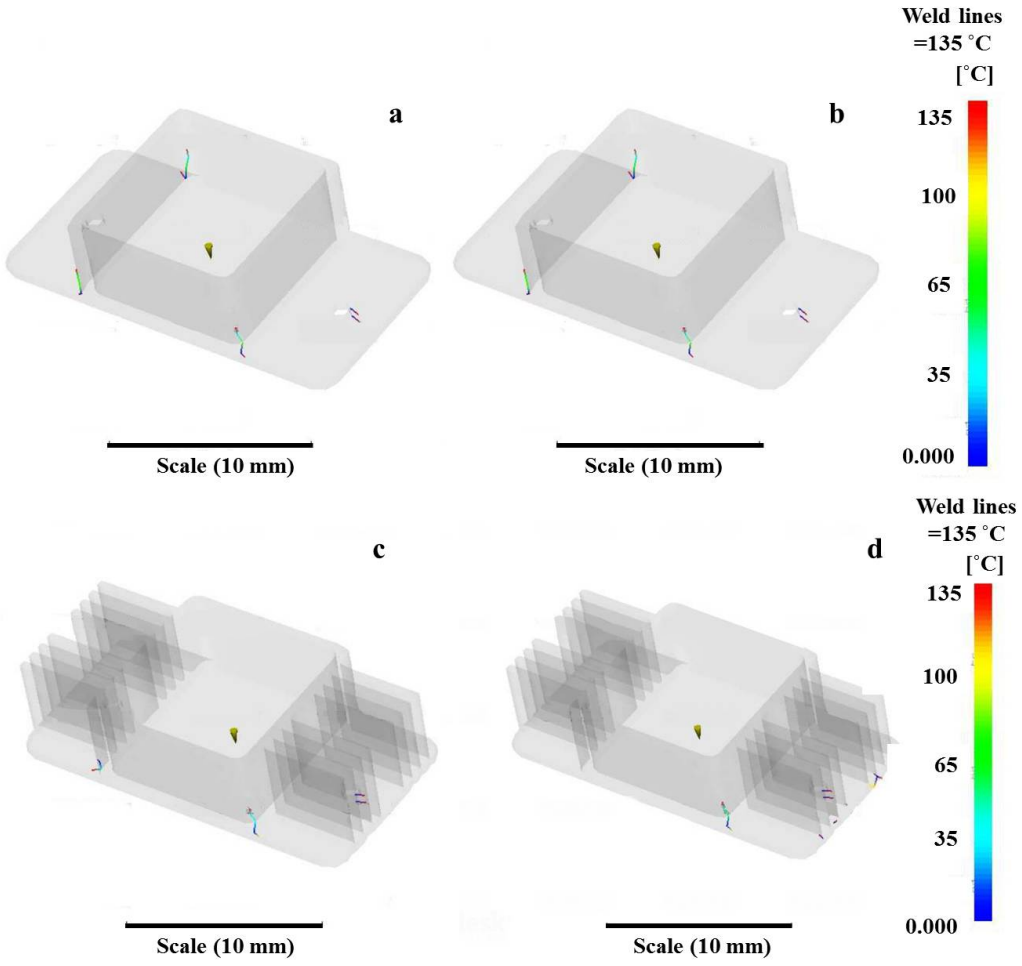

Figure 3.11: Weld-line distribution in the heat-sink geometries without fins (top) and with fins (bottom), at 0.48(a and c) and 0.52 (b and d) volume fractions of AlN powder, ϕ_p.

No significant differences were observed (**Figure 3.11 a** and **b**) for the weld-line distributions in the heat-sink substrate without fins as the powder volume fraction increased from 0.48 to 0.52. In contrast, a number of new weld lines appeared in the fin region of the second heat-sink substrate (**Figure 3.11 c** and **d**) when the powder volume fraction increased from 0.48 to 0.52. Thus, as the part complexity increases, the sensitivity of defect evolution to changes in material composition can increase. Further analysis on the strength of the weld lines as well as residual stresses in the molded parts will be performed in the future, based on the data in **Equations 3.6** and 3.**7**.

3.6 Conclusions

The thermal, rheological and PVT properties of powder-polymer mixtures can be modeled as a function of powder volume fraction in the concentration ranges of interest to PIM. This data is critical to understanding the consequences of material composition on the mold-filling behavior of powder-polymer mixtures. The combination of experimental methods, constitutive models and the computer simulation platform analyzed in this paper represents a useful approach to address problems of precision and defects in PIM parts early in the design cycle. It is anticipated that the approach presented in this paper will avoid expensive and time-consuming, trial-and-error iterations currently prevalent in PIM.

Acknowledgment

S.V. Atre would like to acknowledge financial support from the National Science Foundation (Award # CMMI 1200144).

3.7 References

[1] R. M. German and S. J. Park, Mathematical Relations in Particulate Materials Processing: Ceramics, Powder Metals, Cermets, Carbides, Hard Materials, and Minerals. John Wiley & Sons, 2008.

[2] V. P. Onbattuvelli, S. Vallury, T. McCabe, S. J. Park, and S. Atre, “Properties of SiC and AlN feedstocks for the powder injection moulding of thermal management devices,” Powder Injection Moulding International, vol. 4, no. 3, pp. 64–70, 2010.

[3] J. Chen, J.-G. Mi, and K.-Y. Chan, “Comparison of different mixing rules for prediction of density and residual internal energy of binary and ternary Lennard–Jones mixtures,” Fluid Phase Equilibria, vol. 178, no. 1–2, pp. 87–95, Mar. 2001.

[4] L. E. Nielsen, Predicting the properties of mixtures: mixture rules in science and engineering. M. Dekker, 1978.

[5] T. Zhang, J. R. G. Evans, and K. K. Dutta, “Thermal properties of ceramic injection moulding suspensions in the liquid and solid states,” Journal of the European Ceramic Society, vol. 5, no. 5, pp. 303–309, 1989.

[6] D. T. Jamieson and G. Cartwright, Properties of Binary Liquid Mixtures: Heat Capacity. National Engineering Laboratory, 1978.

[7] R. K. Sinnott, J. M. Coulson, and J. F. Richardson, Chemical engineering design. Butterworth-Heinemann, 2005.

[8] C. J. Cremers and H. A. Fine, Thermal Conductivity. Springer, 1991.

[9] C. P. Wong and R. S. Bollampally, “Thermal conductivity, elastic modulus, and coefficient of thermal expansion of polymer composites filled with ceramic particles for electronic packaging,” Journal of Applied Polymer Science, vol. 74, no. 14, pp. 3396–3403, Dec. 1999.

[10] Y. Zhang, Z. Shen, and Z. Tong, “Thermal Conductivity and Interfacial Thermal Barrier Resistance of the Particle Reinforced Metal Matrix Composites,” in Electronic Packaging Technology, 2007. ICEPT 2007. 8th International Conference on, 2007, pp. 1 –4.

[11] Y. P. Mamunya, “Electrical and thermal conductivity of polymers filled with metal powders,” European Polymer Journal, vol. 38, no. 9, p. 1887, Sep. 2002.

[12] T. Zhang and J. R. G. Evans, “Thermal expansion and equation of state for ceramic injection moulding suspensions,” Journal of the European Ceramic Society, vol. 6, no. 1, pp. 15–21, 1990.

[13] S. Elomari, R. Boukhili, and D. J. Lloyd, “Thermal expansion studies of prestrained Al2O3/Al metal matrix composite,” Acta Materialia, vol. 44, no. 5, pp. 1873–1882, May 1996.

[14] T. Zhang and J. R. G. Evans, “Predicting the viscosity of ceramic injection moulding suspensions,” Journal of the European Ceramic Society, vol. 5, no. 3, pp. 165–172, 1989.

[15] P. C. Hiemenz and R. Rajagopalan, Principles of Colloid and Surface Chemistry. CRC Press, 1997.

[16] V. P. Onbattuvelli, “The effects of nanoparticle addition on the processing, structure and properties of SiC and AlN,” Thesis/Dissertation, 2010.

[17] X. Z. Shi, M. Huang, Z. F. Zhao, and C. Y. Shen, “Nonlinear Fitting Technology of 7-Parameter Cross-WLF Viscosity Model,” Advanced Materials Research, vol. 189–193, pp. 2103–2106, Feb. 2011.

[18] H. H. Chiang, C. A. Hieber, and K. K. Wang, “A unified simulation of the filling and postfilling stages in injection molding. Part I: Formulation,” Polymer Engineering & Science, vol. 31, no. 2, pp. 116–124, 1991.

Chapter 4

Feedstock Properties And Injection Molding Simulations Of Bimodal Mixtures of Nanoscale and Microscale Aluminum Nitride

4.1 Abstract

Powder injection molding (PIM) is useful to manufacture small net-shape complex metal and ceramic components in high production volumes. The use of nanoparticles (n) in conjunction with microparticles (μ) has been previously identified in our research group as a promising approach to achieve high sintered density and low shrinkage in injection molded AlN. The sintering studies showed the formation of liquid phase at 1500°C in the bimodal μ-n AlN samples, a temperature that is at least 100°C lower than typically reported values in the literature. The sintered parts of bimodal μ-n AlN mixtures exhibited comparable sintered density but lower shrinkage (~14%) than the corresponding monomodal mixtures (~20%). These benefits in sintered attributes were accompanied by a significant increase in the maximum powder content (~ 71 vol.%) in powder-polymer mixtures with the addition of nanoparticles. In order to take advantage of the benefits of nanoparticles, a clear understanding of the effects of nanoparticles on feedstock properties is required especially since nanoparticles exhibit poor packing behavior and show high tendency for agglomeration, negatively impacting the rheological behavior and homogeneity of the feedstock. The current study is focused on understanding the effect of nanoparticle addition on the rheological and properties of feedstock**.** The feedstock properties were further used as to carry out mold-filling simulations to understand the effects of powder content on the process parameters and defect evolution during the injection molding process. The feedstock properties and simulations can be used to improve PIM design practices in material selection, component geometry attributes, and optimized process parameters.

4.2 Introduction

Powder injection molding (PIM) has emerged as the primary technology to economically manufacture small net-shape complex metal and ceramic components in high production volumes [1]. The PIM process utilizes a mixture of metal or ceramic powder and polymer (feedstock) to shape the component. In subsequent processing steps, the polymer is removed from the shaped component and the part is sintered at high temperature in a controlled atmosphere to enhance the density and achieve the required functional properties [2].

The feedstock composition and properties play a critical role in successful manufacturing of parts by PIM. A failure to optimize feedstock compositions could result in the formation of defects such as weld-lines, cracks and warpage during the injection molding process. Most of the internal defects formed during injection molding exaggerate during subsequent sintering operations resulting in the production of low quality parts after undergoing significant value addition steps [3]. Thus, understanding the effects of metal or ceramic powders on feedstock properties is critical to the success of the PIM process. One common practice in PIM to avoid the formation of defects is to lower the amount of powder in the feedstock thus increasing the polymer content which in turn enhances the flowability and green strength of the part during injection molding. However lowering the powder content in the feedstock will result in higher shrinkage during sintering resulting in issues with meeting stringent dimensional control requirements of final parts.

The relation between final dimensions of the sintered part and the initial volume fraction of powder ϕ_p is given by **Equation 1** [4]:

$$Y = 1 - \left(\frac{\emptyset_p}{f_s}\right)^{1/3} \qquad (1)$$

where, Y is the linear shrinkage factor and f_s is the fractional sintered density. This inter-relationship between part shrinkage, sintered density and initial volume fraction of powder is shown in **Figure 1**. It can be seen that for a given sintered density, parts with lower volume fraction of powder in the feedstock undergo larger shrinkage. Sintering at a

lower temperature in order to minimize the shrinkage is not viable since it will result in lower density and properties of the component.

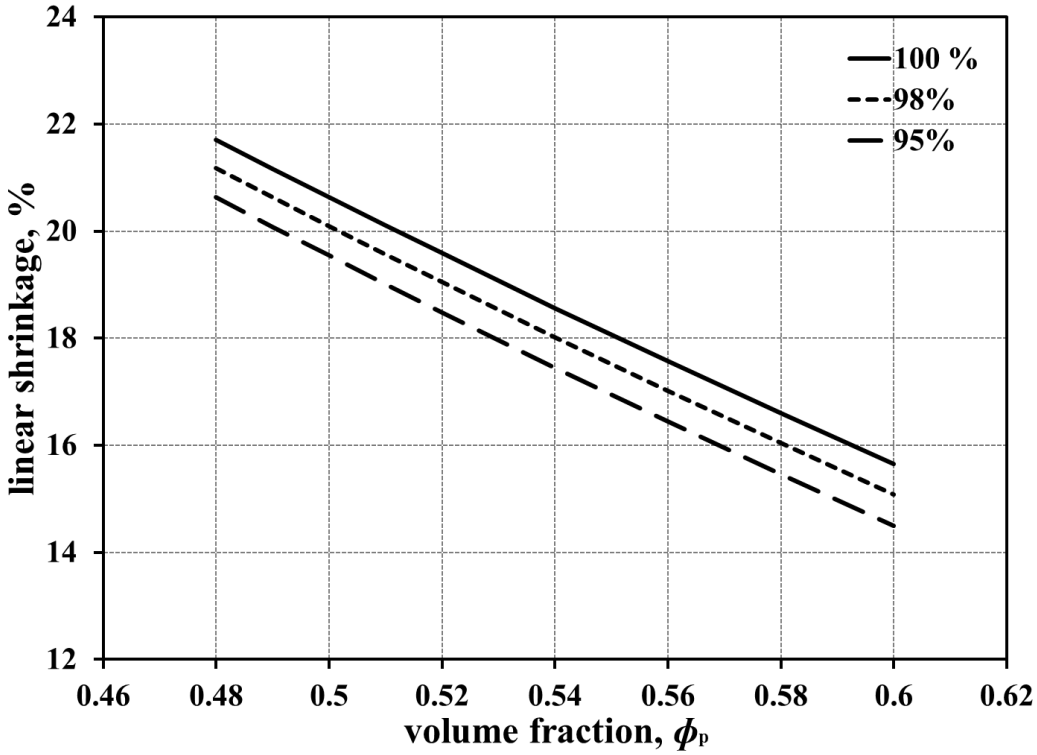

Figure 4.1: Dependence of linear shrinkage on final sintered density and different volume fractions of powder, ϕ_p, using Equation 1.

Similar to other techniques in powder processing techniques, the goal in PIM is also to manufacture parts with high sintered density and low shrinkage. The use of nanoparticles in conjunction with microscale particles was identified as a promising approach to achieve the goal of manufacturing parts with high sintering density with low shrinkage in recent studies emerging from our research group [5-7]. Nanoparticles require lower sintering temperature to achieve high sinter density and parts with superior mechanical properties. These studies have shown the positive effect of addition of nanoparticles in achieving high sintered density and lower shrinkage in injection molded AlN. The sintering studies showed the formation of liquid phase at 1500°C in the bimodal μ-n AlN samples, a temperature that is at least 100°C lower than typically reported values in the literature. The sintered parts of bimodal μ-n AlN mixtures exhibited comparable sintered

density but lower shrinkage (~14%) than the corresponding monomodal mixtures (~20%) [5-7]. Our prior research study [8] also showed significant increase in the maximum powder content in powder-polymer mixture with the addition of nanoparticles. A maximum powder content of 90 wt. % (71 vol. %) was achieved in AlN powder-polymer mixes with the addition of nanoparticles. The monomodal μ AlN powder-polymer mixes had a maximum achievable powder content of only 81 wt.% (54 vol.%) [8]. However, in order to take advantage of the benefits of addition of nanoparticles, a clear understanding of the effect of nanoparticles on feed stock properties is required especially since nanoparticles exhibit poor packing behavior and show high tendency for agglomeration which negatively impact the rheological behavior and homogeneity of the feedstock [8]. The current study is focused on understanding the effects of nanoparticle addition on the rheological, mechanical and thermal properties of bimodal μ-n AlN feedstock.

The simulation of injection molding process relies on the properties of the feedstock as input data [9]. In order to facilitate the design of PIM components using simulation tools, there is a critical need to determine the effects of variation in material composition on the thermal, rheological and mechanical properties of powder-polymer mixtures. The aim of the current study is to understand the effect of change in properties of the feedstock as a result of increased volume fraction due to addition of nanoparticles. Subsequently, the effects of feedstock properties on the mold filling behavior and defect formation were studied using the Autodesk Moldflow Insight simulation platform. The results from the present study will provide a quantitative understanding of the influence of nanoparticle addition on feedstock properties and injection molding process; resulting in the development of new material compositions that will ultimately result in manufacturing complex sintered components with high density and low shrinkage. The simulation results will also assist in selecting component geometry attributes and optimize process parameters while eliminating expensive and time-consuming trial-and-error practices prevalent in the area of PIM.

4.3 Experimental Materials and Methods

Commercially available AlN (~1 μm and ~20 nm) and Y_2O_3 (~50 nm) were used as the starting materials in as received condition. The bimodal μ-n AlN mixtures contained 82 wt.% larger (μ) and 18 wt. % finer (n) AlN powder. 5 wt. % Y_2O_3 was added on the basis of AlN to the powder mixture. The SEM micrograph of the powder is shown in **Figure 2**.

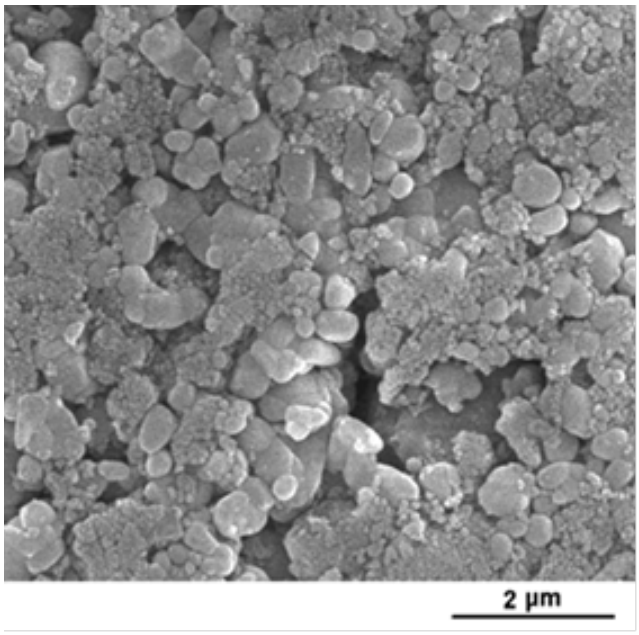

Figure 4.2: SEM of bimodal μ-n AlN powder used in the present study.

A multi-component binder system comprising of paraffin wax (PW), polypropylene (PP), polyethylene-g-maleic anhydride (LDPE-g-MA) and stearic acid (SA) was used in the current study. Details of the composition and mixing preparations are provided elsewhere [10].

The rheological characteristics of the feedstock were examined on a Gottfert Rheograph 2003 capillary rheometer at different shear rates and temperatures. The testing was carried out in accordance with ASTM D3835. The temperatures were between the highest melting temperature and the lowest degradation temperature of the binder system. The barrel of inner diameter of 1 mm and die length of 20 mm was used. The preheating time was kept at 6 minutes. Torque rheometry was performed in the Intelli-Torque Plasticorder (Brabender) in order to determine the maximum packing density of the

powder-polymer mixture. Twin screw extrusion of AlN feedstocks was performed with an Entek co-rotating 27 mm twin screw extruder with an L/D ratio of 40 and pelletized for further use. Injection molding was performed on an Arburg 221M injection molding machine. Thermogravimetric analysis (TGA) was performed on the extruded feedstocks using TA- Q500 (TA instruments) thermal system operated under nitrogen flow in the temperature range of 50-600°C with a heating rate of 20 °C/min in order to confirm the powder weight fraction in the feedstock.

A K-System II Thermal Conductivity System was used to evaluate the thermal conductivity of the feedstock. The testing was carried out in accordance with ASTM D5930. The initial temperature was 190^{o}C and final temperature was 30^{o}C. The probe voltage was kept at 4 V and acquisition time of 45 s. Specific heat measurements were carried out on Perkin Elmer DSC7 equipment in accordance with ASTM E1269. The testing was done with an initial temperature of 190^{o}C and final temperature of 20^{o}C. The cooling rate was kept constant of 20^{o}C/minute. A Gnomix PVT apparatus was used to find the PVT relationships of the feedstock materials. The test was carried out in accordance with ASTM D792. The pellets were dried for 4 hours at 70^{o}C under vacuum. The measurement type used was isothermal heating scan with a heating rate of approximately 3^{o}C/minute.

Autodesk Moldflow Insight 2011 software was used for simulating the injection conditions of two heat sink geomteries. The heat sink geometries were built using Autodesk Solidworks 2011 software and the geometry was imported in Moldflow Insight software. The part was meshed using an automated solid 3D meshing which makes use of finite element analysis for meshing. The process settings were 303K for the mold temperature and 433K for the melt temperature. Simulations were conducted for a fill-and-pack type condition in order to meet the objective of understanding injection molding behavior and its packing characteristics.

4.4 Results and Discussion

4.4.1 Properties

The experimentally determined physical properties of bimodal μ-n AlN powder-polymer mixtures at 0 and 0.6 volume fractions were used to estimate properties of bimodal μ-n AlN powder-polymer mixtures with 0.52 to 0.58 volume fractions. Several models have been published in the literature to predict various properties of feedstocks that are necessary as input data for conducting mold-filling simulations [11-28]. The empirical models used in the present study were selected after carrying out an in-depth statistical analysis of the ability of various published models to fit literature data on powder-polymer mixture properties [29]. The empirical models used to estimate various properties of bimodal μ-n AlN are summarized in **Table 4.1**. The descriptions of symbols in the empirical formulas are detailed in **Table 4.2**. Additionally, the viscosity and PVT data required curve fitting to extract constants required for mold filling simulations using Autodesk Moldflow Insight software

A simplified Krieger-Dougherty [7] viscosity model was used as it is suitable for predicting viscosity values at higher volume fractions of powder (**Equation 4.2**). The Cross-WLF model [11] was used to model the viscosity dependence of any given powder-polymer mixture on shear rate (**Equation 4.3**). The temperature dependence of viscosity of any powder-polymer mixture [11] was estimated using **Equation 4.4.** The values of the coefficients (T^*, D_1 and A_1,) were obtained by curve-fitting the estimated viscosity for different volume fractions of powder at various shear rates and temperatures and are summarized in **Table 4.3.** Additionally, the viscosity and PVT data required curve fitting to extract constants required for mold filling simulations using Autodesk Moldflow Insight software

Table 4.1: Models used in the present study to estimate the feedstock properties.

Property	Empirical relation	Equation number
Viscosity	$\eta_c = \frac{\eta_b}{\left[1-\frac{\phi_p}{\phi_{max}}\right]^2}$	4.2
	$\eta = \frac{\eta_0}{1+\left(\frac{\eta_0 \gamma}{\tau^*}\right)^{1-n}}$	4.3
	$\eta_0 = D_1 exp\left[-\frac{A_1(T-T^*)}{A_2+(T-T^*)}\right]$	4.4
Specific volume	$v_c = X_p v_p + v_b(1-X_f)$	4.5
	$v(T,p) = v_o(T)\left[1 - Cln\left(1+\frac{p}{B(T)}\right) + v_t(T,p)\right]$	4.6
	$T > T_t$: $v_o = b_{1m} + b_{2m}(T-b_5) B(T) = b_{3m} e^{[-b_{4m}(T-b_5)]} v_t(T,p) = 0$	4.7
	$T < T_t$: $v_o = b_{1s} + b_{2s}(T-b_5) B(T) = b_{2s} e^{[-b_{4s}(T-b_5]} v_t(T,p) = b_7 e^{[b_8(T-b_5)-(b_9 p)]}$	4.8
Density	$\frac{1}{\rho_c} = \frac{X_b}{\rho_b} + \frac{X_p}{\rho_p}$	4.9
Mass fraction	$X_p = \frac{\phi_p \rho_p}{\phi_p \rho_p + \phi_b \rho_b}$	4.10
	$X_b = \frac{\phi_b \rho_b}{\phi_p \rho_p + \phi_b \rho_b}$	4.11
Specific heat	$C_{p_c} = \left[C_{p_b} X_b + C_{p_p} X_p\right] * \left[1 + A * X_b X_p\right]$	4.12
Thermal conductivity	$\lambda_c = \lambda_b \phi_b + \lambda_p \phi_p$	4.13
Coefficient of thermal expansion	$\alpha_c = X_p \alpha_p + \alpha_b (1-X_p)$	4.14
Elastic and shear modulus	$E_c = E_p X_p + E_b (1-X_b)$	4.15

Table 4.2: Descriptions of the symbols used in empirical relations presented in Table 4.1.

Symbol	Description	Symbol	Description
η_b	viscosity of binder	ρ_p	density of powder
η_c	viscosity of composite	X_c	mass fraction of composite
ϕ_p	volume fraction of powder	X_b	mass fraction of binder
ϕ_{max}	maximum volume fraction	X_p	mass fraction of powder
η	melt viscosity	C_p	specific heat
η_0	zero shear viscosity	λ	thermal conductivity
γ	shear rate	α	thermal expansion coefficient
τ^*	critical stress level at the transition to shear thinning	E	elastic or shear modulus
n	power law index in the high shear rate regime	υ	specific volume
T	temperature	υ (T,p)	specific volume at a given temperature and pressure
T^*, D_1 and A_1	curve-fitted coefficients	υ_o	specific volume at zero gauge pressure
T_t	volumetric transition temperature	p	Pressure
A_2	WLF constant, 51.6 K	C	constant, 0.0894
ρ_c	density of composite	b_{1s}, b_{2s}, b_{3s}, b_{4s},b_5, b_7,b_8,b_9	curve-fitted coefficients
ρ_b	density of binder	b_{1m},b_{2m},b_{3m}, b_{4m},b_5 ,b_6	curve-fitted coefficients

A simplified Krieger-Dougherty [7] viscosity model was used as it is suitable for predicting viscosity values at higher volume fractions of powder (**Equation 4.2**). The Cross-WLF model [11] was used to model the viscosity dependence of any given powder-polymer mixture on shear rate (**Equation 4.3**). The temperature dependence of viscosity of any powder-polymer mixture [11] was estimated using **Equation 4.4.** The values of the coefficients (T^*, D_1 and A_1,) were obtained by curve-fitting the estimated viscosity for different volume fractions of powder at various shear rates and temperatures and are summarized in **Table 4.3.**

Table 4.3: Cross-WLF constants for different volume fractions of bimodal μ-n AlN powders.

Cross-WLF constants		**volume fraction, ϕ_p**				
	0	0.52	0.54	0.56	0.58	**0.6**
n	**0.40**	0.24	0.21	0.18	0.13	**0.05**
τ, Pa*	**793**	30077	44040	67975	116687	**161976**
D_1, *Pa·s*	**$4.29\text{x}10^{23}$**	$1.08\text{x}10^{14}$	$1.83\text{x}10^{14}$	$4.29\text{x}10^{14}$	$1.71\text{x}10^{15}$	**$9.13\text{x}10^{19}$**
T, K*	**333.00**	264.65	266.14	264.65	264.65	**263.15**
A_1	**78.13**	29.55	29.56	29.55	29.55	**29.54**
A_2, *K*	**51.60**	51.60	51.60	51.60	51.60	**51.60**

Figure 4.3 shows the shear-rate dependence of viscosity for bimodal μ-n AlN at 413 and 433 K.

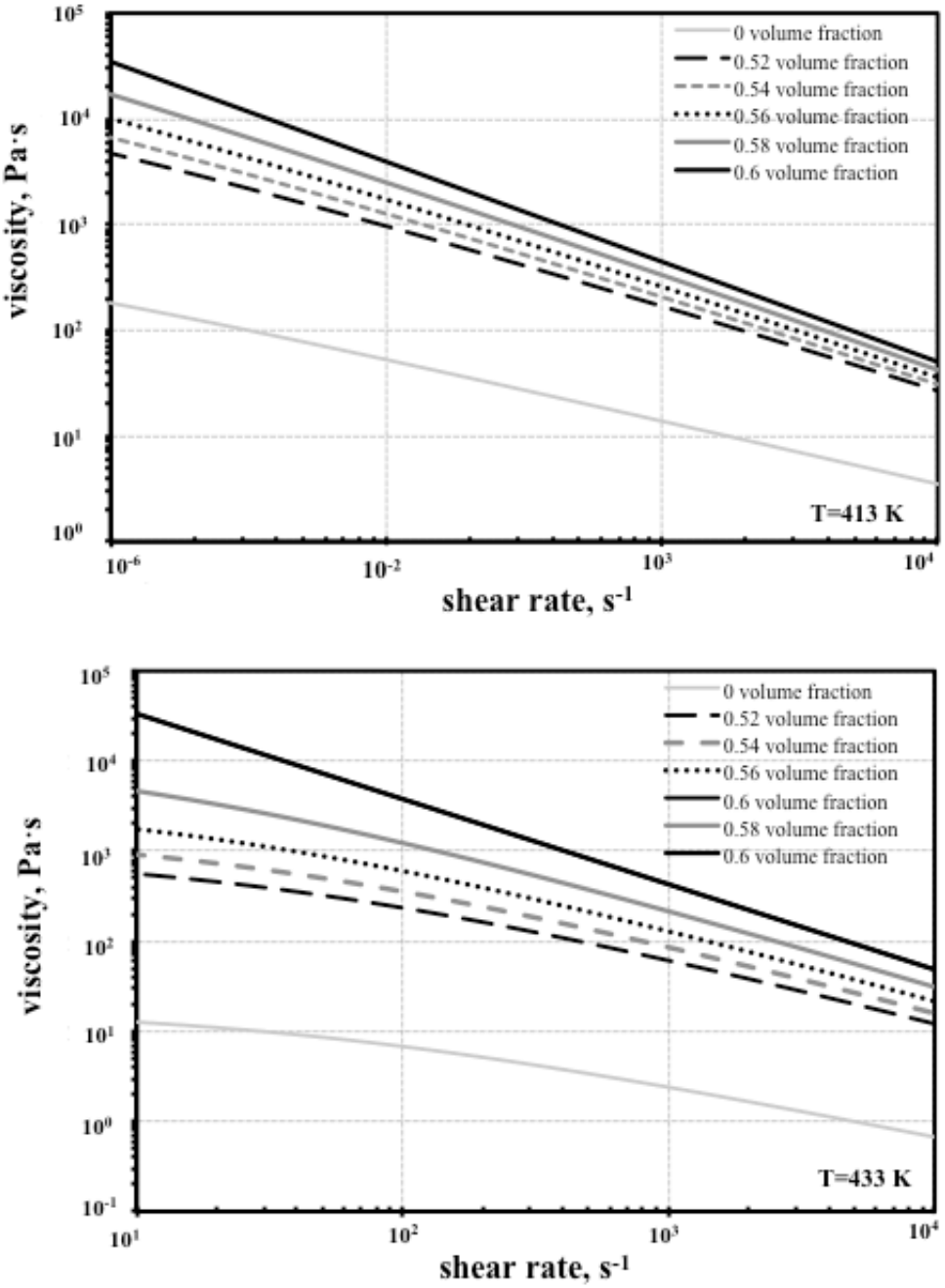

Figure 4.3: Comparison of viscosity with shear rate at 413 K (top) and 433 K (bottom) for different volume fractions of bimodal μ-n AlN powder.

The zero-shear viscosity was estimated from the plateau region at low shear rate while the power law index was obtained from the slope at higher shear rates. It can be observed that the zero-shear viscosity increased considerably with small increases in volume fraction, ϕ_p, in the range of interest. The curve-fitted WLF parameters n, τ^*, D_1, T^*, A_1 and A_2 were estimated for temperatures between 413 K and 433 K. The values estimated for n and τ^* for each temperature were then averaged out for individual volume fractions of powder. The values of rest of the parameters did not vary appreciably with an increase in temperature in the range evaluated in experiments. The power law index, n, decreased from 0.24 to 0.05 with an increase in volume fraction from 0.52 to 0.60. Similarly, τ^* increased from 3 x 10^4 to 1.6 x 10^5 MPa with an increase in volume fraction from 0.52 to 0.60. There was no change in transition temperature (T^*) at which the material exhibits a change from Newtonian to shear-thinning behavior on increasing shear rates with increase in volume fraction of the powder.

The specific volume was calculated using the general rule-of-mixtures as shown in **Equation 4.5** [12]. The injection molding software platform uses the two-domain Tait [13] equation (**Equation 4.6**) for generating viscosity values at different volume fractions of powder. The parameter, B, accounts for the pressure sensitivity of the material and is separately defined for the solid and melt regions. For the upper bound, when $T > T_t$ (volumetric transition temperature), B is given by **Equation 4.7**. For the lower bound, when $T < T_t$, the parameter, B, is given by **Equation 4.8**. The dependence of the volumetric transition temperature, T_t on pressure can be given by $T_t(p) = b_5+b_6(p)$, where b_5 and b_6 are curve-fitted coefficients. The values of these coefficients are summarized in **Table 4.4**.

Table 4.4: Dual-domain Tait constants for different volume fractions of bimodal μ-n AlN powders.

dual-domain Tait constants	**volume fraction, ϕ_p**						
	0	0.5	0.52	0.54	0.56	0.58	**0.6**
b_5, K	**336**	336	336	336	336	336	**336**
b_6, K/Pa	**1.5×10^{-7}**	1.6×10^{-7}	1.6×10^{-7}	1.6×10^{-7}	1.6×10^{-7}	1.6×10^{-7}	**1.6×10^{-7}**
b_{1m}, m^3/kg	**1.3×10^{-3}**	5.1×10^{-4}	4.9×10^{-4}	4.8×10^{-4}	4.7×10^{-4}	4.6×10^{-4}	**4.5×10^{-4}**
b_{2m}, $m^3/kg\cdot K$	**1.3×10^{-6}**	2.8×10^{-7}	2.6×10^{-7}	2.4×10^{-7}	2.2×10^{-7}	2.0×10^{-7}	**1.8×10^{-7}**
b_{3m}, Pa	**1.3×10^{8}**	3.4×10^{8}	3.4×10^{8}	3.4×10^{8}	3.4×10^{8}	3.4×10^{8}	**3.4×10^{8}**
b_{4m}, K^{-1}	**6.0×10^{-3}**	4.0×10^{-3}	4.0×10^{-3}	4.0×10^{-3}	4.0×10^{-3}	4.0×10^{-3}	**4.0×10^{-3}**
b_{1s}, m^3/kg	**1.2×10^{-3}**	4.9×10^{-4}	4.8×10^{-4}	4.7×10^{-4}	4.6×10^{-4}	4.5×10^{-4}	**4.3×10^{-4}**
b_{2s}, $m^3/kg\cdot K$	**8.6×10^{-7}**	2.6×10^{-7}	2.3×10^{-7}	2.0×10^{-7}	1.8×10^{-7}	1.5×10^{-7}	**1.5×10^{-7}**
b_{3s}, Pa	**2.4×10^{8}**	5.0×10^{8}	5.0×10^{8}	5.0×10^{8}	5.0×10^{8}	5.0×10^{8}	**5.0×10^{8}**
b_{4s}, K^{-1}	**4.2×10^{-3}**	6.5×10^{-3}	4.3×10^{-3}	9.7×10^{-3}	9.2×10^{-2}	1.1×10^{-2}	**1.0×10^{-2}**
b_7, m^3/kg	**8.5×10^{-5}**	2.0×10^{-6}	3.8×10^{-6}	2.8×10^{-6}	2.9×10^{-6}	8.7×10^{-7}	**8.9×10^{-6}**
b_8, K^{-1}	**6.7×10^{-2}**	2.5×10^{-2}	1.2×10^{-2}	3.9×10^{-2}	4.0×10^{-2}	6.1×10^{-2}	**1.3×10^{-1}**
b_9, Pa^{-1}	**1.4×10^{-8}**	2.2×10^{-8}	2.2×10^{-8}	2.2×10^{-8}	2.2×10^{-8}	2.2×10^{-8}	**2.2×10^{-8}**

Figure 4.4 shows the comparative plot of specific volumes at 0, 100, and 200 MPa pressure.

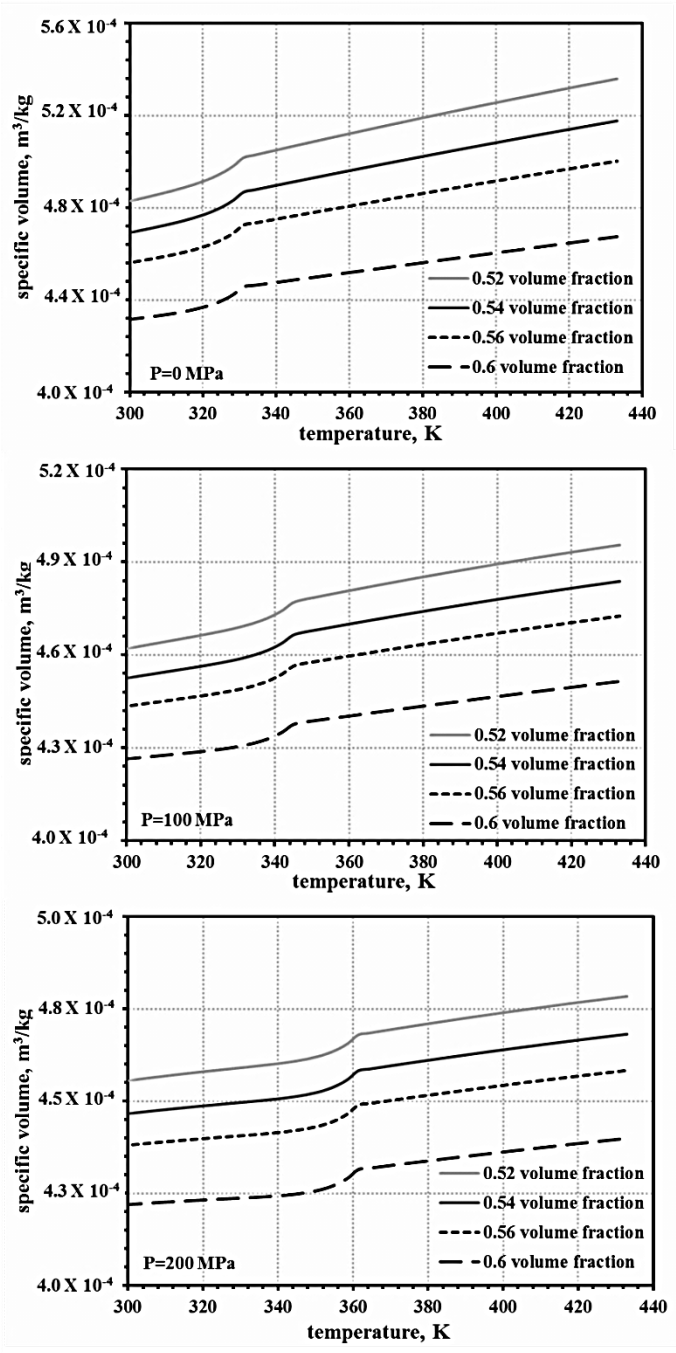

Figure 4.4: PVT behavior for 0, 100, and 200 MPa pressures for different volume fractions of bimodal μ-n AlN powder.

The specific volume decreases with an increase in volume fraction of bimodal μ-n AlN. The dual-domain Tait constants were estimated using curve fitting for 0, 50, 100, 150, 200 MPa pressure for volume fractions of 0, 0.52 to 0.60 bimodal μ-n AlN. The parameters, b_5, b_6, b_9, b_{3m}, b_{4m}, b_{3s} and b_{4s} did not vary in the range of 0.52 to 0.60 volume fraction of bimodal μ-n AlN. The parameters b_{1m}, b_{2m}, b_{1s} and b_{2s} showed a minor decrease on increasing the volume fractions from 0.52 to 0.60. Parameters, b_7 and b_8 increased with increase in volume fraction of powder.

An inverse rule-of-mixtures [12] shown in **Equation 4.9** was used to estimate the melt and solid density**.** Further, the mass fractions for powder and binder can be calculated using **Equation 4.10-4.11**. The comparison of melt and solid density as a function of volume fraction of bimodal μ-n AlN is shown in **Table 4.5.**

Table 4.5: Comparison of melt and solid densities for different volume fractions of bimodal μ-n AlN powders.

volume fraction of powder, ϕ_p	**melt density, kg/m^3**	**solid density, kg/m^3**
0	**727**	**879**
0.52	1950	2119
0.54	2002	2167
0.56	2055	2214
0.58	2109	2262
0.6	**2163**	**2310**

The melt and solid density values increased with increase in powder volume fraction. The melt density increased from 1950 to 2163 kg/m^3 and solid density increased from 2119 to

2310 kg/m^3 with increase in volume fraction of bimodal μ-n AlN from 0.52 to 0.60. The data in **Table 4.5** indicates a ± 4% variation in melt and solid density as a result of a ±7% change in the volume fraction of bimodal μ-n AlN.

The specific heat of powder-polymer mixtures has been be estimated by different mixing rules [14-18]. In this study, a model that has been successfully applied to mixtures with high volume fraction fillers [15] was used as shown in **Equation 12**. The parameter, *A*, is a correction factor assumed to be 0.2 for spherical particles. The specific heat values calculated for different volume fractions of powder at various temperatures are shown in **Table 4.6**.

Table 4.6: Specific heat capacity values at various temperatures for different volume fractions of bimodal μ-n AlN powders.

volume fraction of powder, ϕ_p	**Temperature, K**						
	273	293	303	322	331	384	443
	specific heat capacity, C_p, J/kg-K						
0	**2077**	**3360**	**3840**	**4894**	**4639**	**3484**	**2528**
0.52	1006	1291	1613	3049	1476	1358	1491
00.54	1004	1263	1575	3014	1422	1346	1470
0.56	1002	1002	1539	2980	1370	1335	1450
0.58	1000	1211	1505	2947	1321	1325	1431
0.6	**998**	**1186**	**1472**	**2915**	**1274**	**1315**	**1413**

The specific heat of the feedstock decreased with increase in volume fraction of powders. As a specific example, a change of volume fraction from 0.52 to 0.60 at 443 K resulted in

a decrease in specific heat from 1491 to 1413 J/g-K. The data in **Table 4.6** indicates that a ±2 % change in specific heat results from a ±7 % change in the volume fraction of bimodal μ-n AlN.

Several equations have been used to predict thermal conductivity of a composite at different filler concentrations [14, 16-25]. In this study, a general rule-of-mixtures model [12] was used as represented in **Equation 4.13**. The estimated values of thermal conductivity as a function of volume fraction of powder at various temperatures are shown in **Table 4.7**.

Table 4.7: Thermal conductivity for different volume fractions of bimodal μ-n AlN powder.

volume fraction of powder, ϕ_p	**Temperature, K**						
	315	336	356	377	397	417	436
	Thermal conductivity, W/m·K						
0	**0.2**	**0.2**	**0.2**	**0.2**	**0.2**	**0.2**	**0.2**
0.52	2.7	2.7	2.9	2.0	2.1	3.0	1.9
0.54	2.8	2.8	2.9	2.1	2.2	3.1	2.0
0.56	2.9	2.9	3.1	2.1	2.2	3.2	2.0
0.58	3.0	3.0	3.2	2.2	2.3	3.3	2.1
0.6	**3.1**	**3.1**	**3.3**	**2.3**	**2.4**	**3.4**	**2.2**

It can be seen that the thermal conductivity increases with increase in volume fraction of bimodal μ-n AlN. For example, the thermal conductivity increased from increases from 1.9 to 2.2 W/m.K with an increase in volume fraction from 0.52 to 0.6 bimodal μ-n AlN

at 436K. The data presented in **Table 4.7** indicate that a ± 8% variation in thermal conductivity results from a ± 7% change in volume fraction of bimodal μ-n AlN.

The coefficient of thermal expansion (CTE) of powder-polymer mixtures can be calculated using several models [18, 25-28]. In this paper, a first order model was used [18] as shown in **Equation 14**. The CTE data are as shown in **Table 4.8**. The data in **Table 4.8** clearly shows an increase in CTE with an increase in volume fraction of bimodal μ-n AlN. Typically in the range of 0.52 to 0.60 volume fractions, the CTE varied between 2.2 E-5 to 1.7 E-5 K^{-1} which represents a ± 12.8% variation in CTE for a ± 7% change in volume fraction of bimodal μ-n AlN in the powder-polymer mixtures.

Table 4.8: Coefficient of thermal expansion for different volume fractions of bimodal μ-n AlN powder.

volume fraction of powder, ϕ_p	**CTE (x 10^{-5}), K^{-1}**
0	**5.65**
0.52	1.94
0.54	1.9
0.56	1.8
0.58	1.77
0.60	**1.72**

The Voigt model [18] was used to predicting the elastic and shear modulus as shown in **Equation 4.15**. The elastic and shear modulus values estimated at different volume fractions of powder is shown in **Table 4.9**. The elastic and shear modulus values were found to increase with an increase in volume fraction of bimodal μ-n AlN. Typically, in

the range of 0.52 to 0.60 volume fraction, the elastic modulus increased between ~1.9 x 10^4 to ~2.1 x 10^4 MPa and shear modulus varies between 7.1 X 10^3 to 8.1 X 10^3 MPa which represents a ± 6.3% variation in the elastic and shear modulus for a ± 7% change in volume fraction of bimodal μ-n AlN in the powder-polymer mixtures.

Table 4.9: Elastic and shear modulus values for different volume fractions of bimodal μ-n AlN powder.

volume fraction of powder, ϕ_p	**Elastic modulus, MPa**	**Shear modulus, MPa**
0	**2560**	**930**
0.52	18860	7120
0.54	19490	7360
0.56	20110	7600
0.58	20740	7840
0.6	**21370**	**8075**

4.4.2 Simulation Results

Simulations were conducted for 0.52 - 0.60 volume fraction of bimodal μ-n AlN at 433 K melt temperature and 303 K mold temperatures using the heat-sink geometries shown in **Figure 4.5.** The simulations were performed for mold filling and packing stages. The progressive filling behavior of the feedstock with 0.60 volume fraction of bimodal μ-n AlN is shown in **Figure 4.6** for the two geometries. The figure clear shows that the narrow fin region of the mold cavity fills at the end of the molding stage, when the material is at its most viscous.

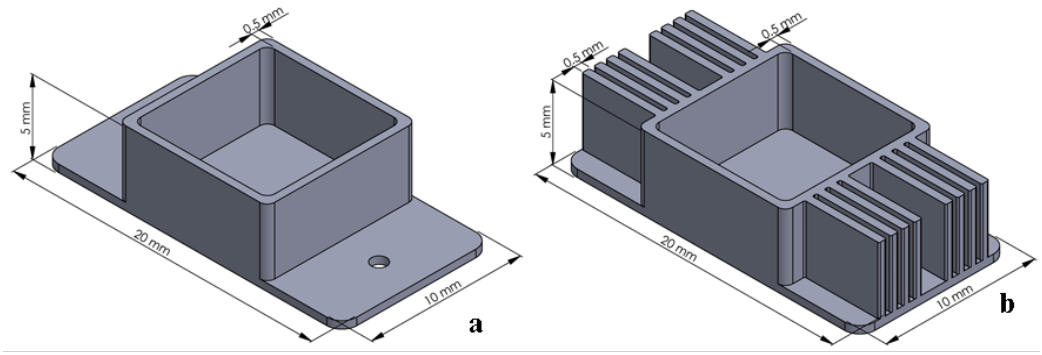

Figure 4.5: Mold geometry used in injection molding simulations: a) simple heat-sink substrate without fins, and b) heat sink substrate with fins.

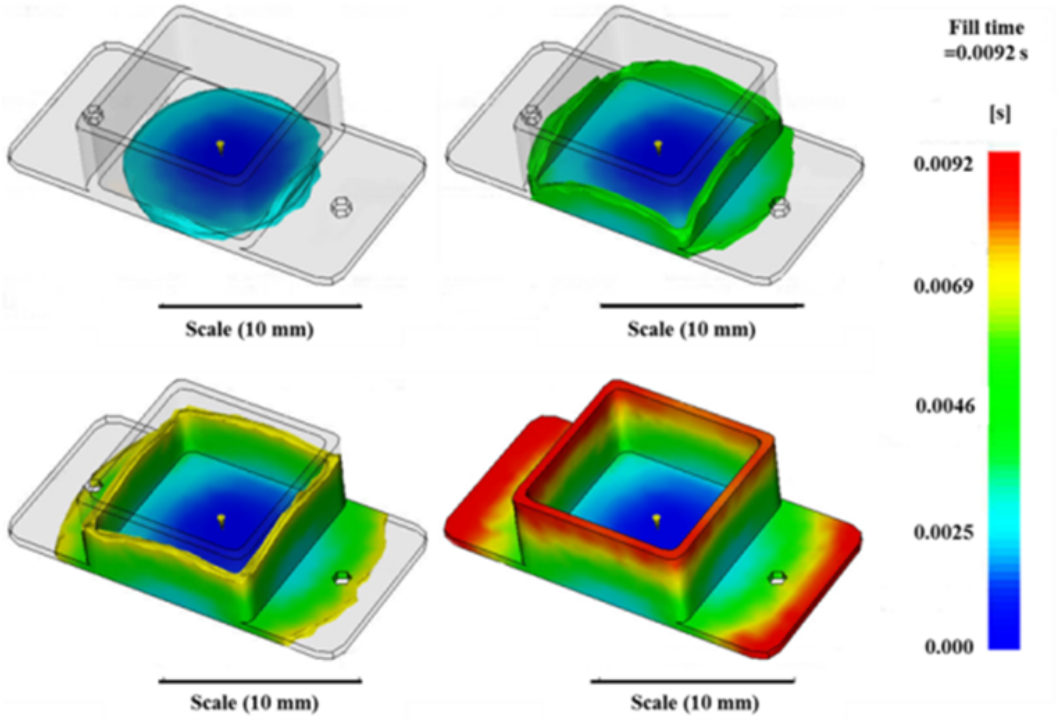

Figure 4.6A: Progressive filling of the heat sink substrate without fins shown in Figure 5A for 0.60 volume fraction bimodal μ-n AlN feedstock: (a) 25% fill, (b) 50% fill, (c): 75% fill and (d) 100% fill

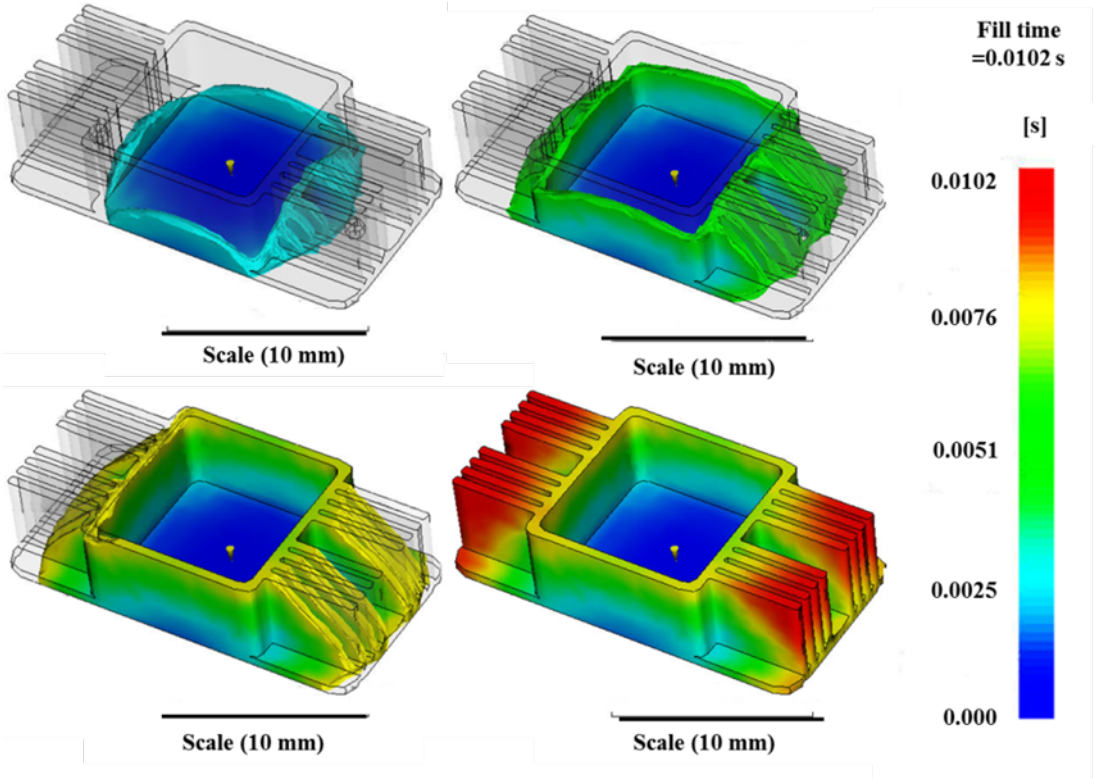

Figure 4.6B: Progressive filling of the heat sink substrate with fins shown in Figure 5B for 0.60 volume fraction bimodal μ-n AlN feedstock: (a) 25% fill, (b) 50% fill, (c): 75% fill and (d) 100% fill

Figure 7 shows the variation of part weight as a function of volume fraction of bimodal μ-n AlN for the two heat-sink geometries shown in **Figure 5**. The part weight increases with an increase in volume fraction of bimodal μ-n AlN powder from 0.52 to 0.60. This increase in part weight with an increase in powder volume fraction can be attributed to an increase in density values with a rise in volume fractions of bimodal μ-n AlN as observed in **Table 4**. Further, for a bimodal μ-n AlN powder volume fraction change from 0.52 to 0.60, the part weight changes from 0.38 to 0.41 g for heat sink substrate without fins. In the case of the heat sink substrate with fins, the corresponding change is from 0.79 to 0.82 g. This change denotes a ± 2% variation in part weight for a ± 7% change in the volume fraction of bimodal μ-n AlN. The part weight doubled for heat sink substrate with fins in comparison to the heat sink substrates without fins.

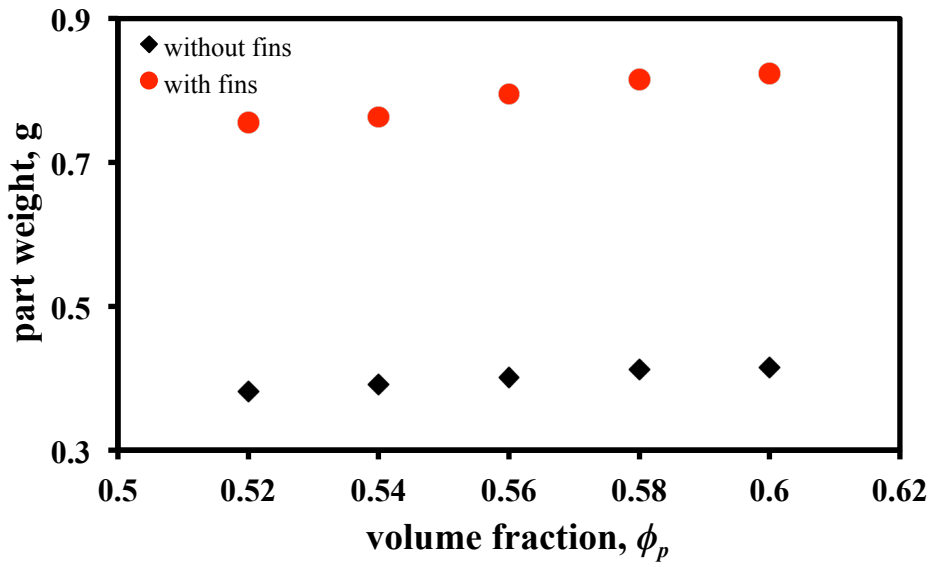

Figure 4.7: Part weight for different volume fractions of bimodal μ-n AlN powder.

As the filling phase nears completion, the packing phase commences during which the part cools till a 100 % frozen volume is obtained. **Figure 4.8** shows the dependence on freeze time on the volume fraction of bimodal μ-n AlN powder in the feedstock.

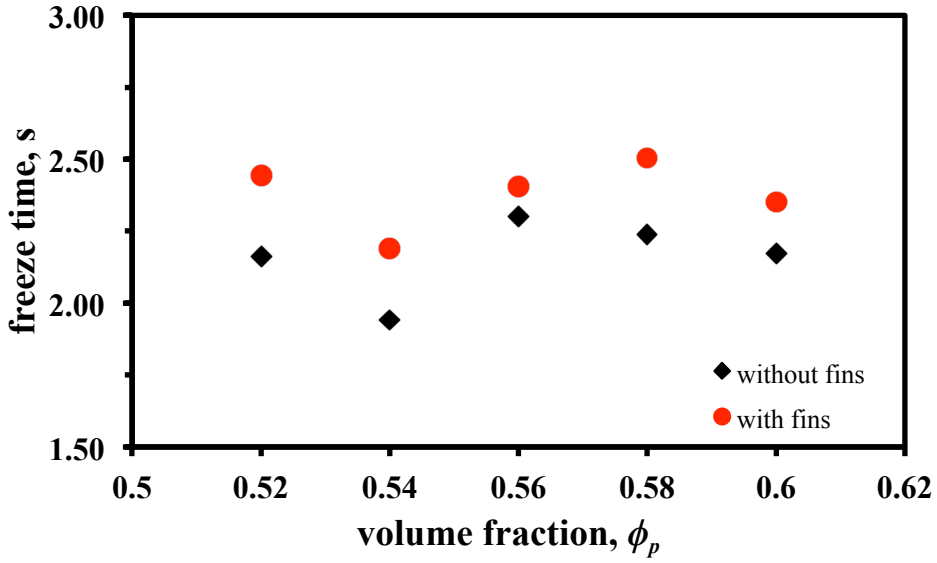

Figure 4.8: Freeze time for different volume fractions of bimodal μ-n AlN powder.

It can be observed from **Figure 4.8** that for a change of 0.52 to 0.60 volume fraction of bimodal μ-n AlN, the freeze time changes from 2.16 to 2 s for heat sink substrate without fins. In the case of the heat-sink substrate with fins, the change in freeze time is from 2.45 to 2.35 s. This denotes a ± 2% variation in freeze time for a ± 7% change in the volume fraction of bimodal μ-n AlN. The relatively small difference in freeze time for the two geometries despite the increase in surface area in the heat-sink substrate with fins can be attributed to the corresponding increase in part weight/volume.

Figure 4.9 shows the variation in peak injection pressure as a function of the volume fraction of powder for the two heat-sink substrates.

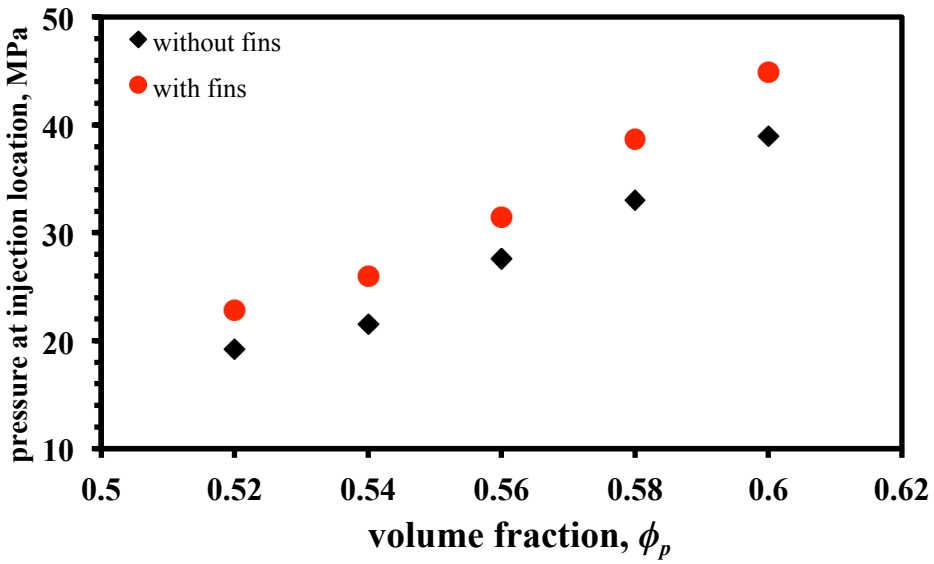

Figure 4.9: Peak injection pressure for different volume fractions of bimodal μ-n AlN powder.

The peak injection pressure is located near the gate of the mold cavity. The peak injection pressure is relatively higher for the heat-sink substrate with fins compared to the heat-sink substrate without fins as a result of an increase in volumetric flow rate. It can be seen that for the heat-sink substrate with fins, the peak injection pressure increases from 23 to 48 MPa with an increase in powder volume fraction from 0.52 to 0.60. This behavior can be attributed to an increase in the viscosity of the powder-polymer mixture with volume fraction of bimodal μ-n AlN. An increase in injection pressure directly increases the

clamp force (**Figure 4.10**) and correspondingly reduces the number of mold cavities that can be simultaneously filled on a molding machine. An increase in injection pressure can also result in an undesirable alteration of the melt flow such as jetting. Further, microstructural inhomogeneity can also be introduced in the part at higher injection pressures due to powder-polymer separation.

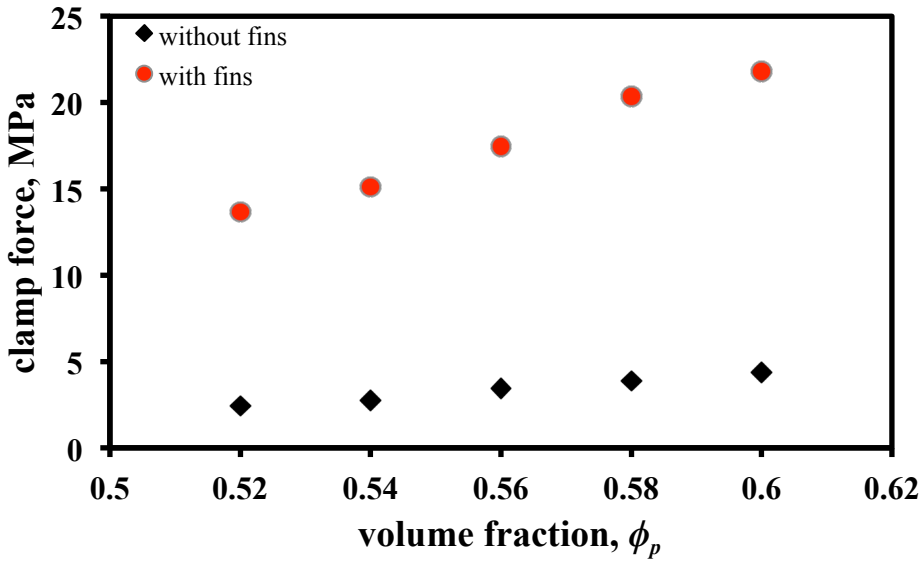

Figure 4.10: Variation of clamp force for different volume fractions of bimodal μ-n AlN powder.

3.3 Defect Quality

Figure 4.11 shows the weld-line distribution for the two heat-sink substrates at 0.52 and 0.60 volume fraction of bimodal μ-n AlN. No significant differences were observed for the weld-line distributions in the heat-sink substrate without fins as the powder volume fraction increased from 0.52 to 0.60. In contrast, a number of new weld lines appeared in the fin region of the second heat-sink substrate when the powder volume fraction increased from 0.52 to 0.60. The results suggest that the probability of defect evolution increases with increase in complexity of the part geometry and material composition.

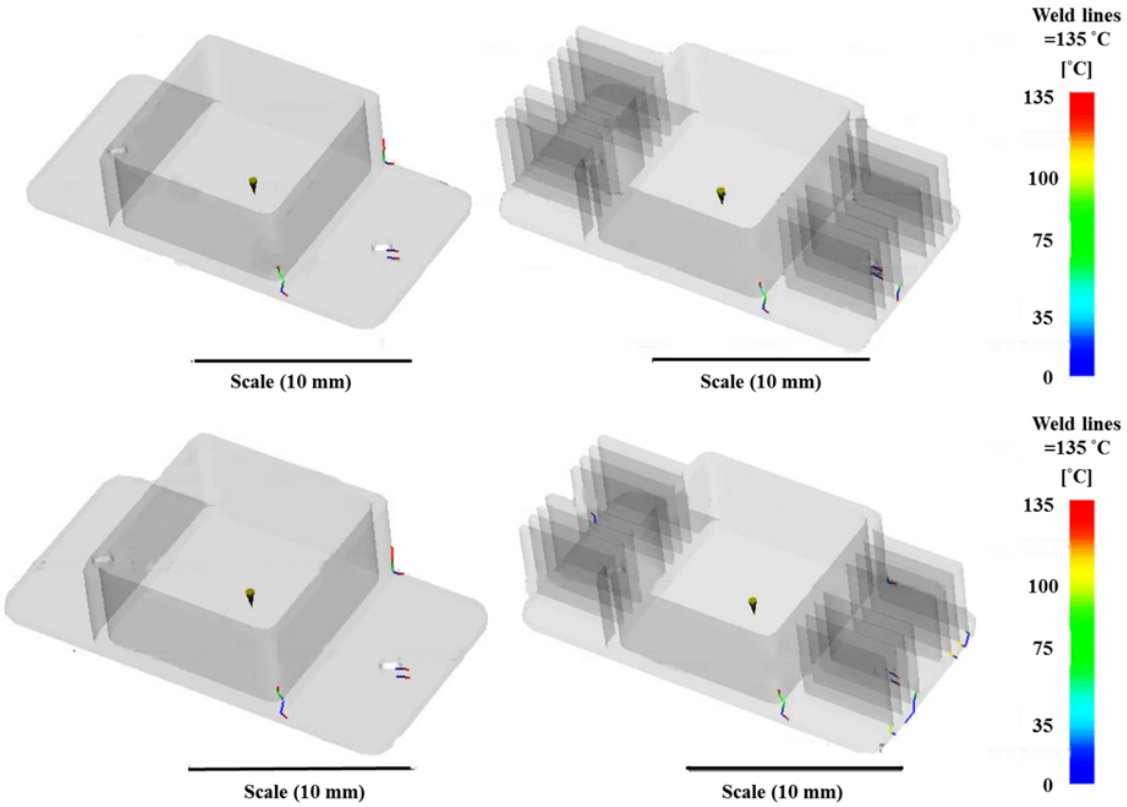

Figure 4.11: Simulation results of weld lines at 0.52 volume fractions (top) and 0.6 volume fractions (bottom) bimodal μ-n AlN powder for heat sink geometry with and without fin

4.5. Conclusions

The effects of nanoparticle addition on the rheological and properties of feedstock were studied in the present paper. The addition of nanoparticles showed a significant effect on the rheological properties of the feedstock, owing to an increase in the maximum packing fraction in the powder-polymer mixtures. The zero shear viscosity, melt density, solid density, thermal conductivity, coefficient of thermal expansion, elastic and shear modulus increased with increase in volume fraction of the powders. On the other hand, properties like specific volume and specific heat decreased with increase in volume fraction of powder. The simulation studies obtained from the feedstock properties showed an increase in part weight and peak injection pressure with increase in powder volume fraction. The studies also showed a decrease in freeze time with increase in powder volume fraction. The feedstock properties and simulations presented in the paper can be used to design new materials, select component geometry attributes, and optimize process parameters while eliminating expensive and time-consuming trial-and-error practices prevalent in the area of powder injection molding.

4.6. References

[1] D. F. Heaney, “Handbook of metal injection molding”, Woodhead Publishing Limited, Cambridge, UK, 2012.

[2] R. M. German, “Powder Metallurgy Science”, Metal Powder Industries Federation, 105 College Rd. E, Princeton, N. J. 08540, U. S. A, 1984.

[3] R. K. Enneti , S. J. Park , R. M. German, S. V.Atre, “Review: thermal debinding process in particulate materials processing”, Materials and Manufacturing Processes, 27: 103–118, 2012.

[4] R. M. German and S. J. Park, Mathematical Relations in Particulate Materials Processing: Ceramics, Powder Metals, Cermets, Carbides, Hard Materials, and Minerals. John Wiley & Sons, 2008.

[5] V. P. Onbattuvelli, R. K. Enneti, and S. V. Atre, “The effects of nanoparticle addition on the sintering and properties of bimodal μ-n AlN”, Ceramics International, Volume 38, Issue 8, pp. 6495–6499, 2012.

[6] V. P. Onbattuvelli, R. K. Enneti, and S. V. Atre, “The effects of nanoparticle addition on the densification and properties of SiC”, Ceramics International, Volume 38, Issue 7, pp. 5393–5399, 2012.

[7] V. P. Onbattuvelli, “The effects of nanoparticle addition on the processing, structure and properties of SiC and AlN,” Thesis/Dissertation, 2010.

[8] V. P. Onbattuvelli, R. K. Enneti, S. J. Park, and S. V. Atre, “The effects of nanoparticle addition on SiC and AlN powder–polymer mixtures: Packing and flow behavior” Int. Journal of Refractory Metals and Hard Materials 36,77–84, 2013.

[9] K.H. Kate, V.P. Onbattuvelli, R.K. Enneti, S.W. Lee, S. J. Park, and S.V. Atre, “Measurements of powder–polymer mixture properties and their use in powder injection molding simulations for aluminum nitride,” Journal of the Minerals, Metals and Materials Society (JOM), Vol. 64, No. 9, pp. 1048-1058, 2012.

[10] V. P. Onbattuvelli, S. Vallury, T. McCabe, S. J. Park, and S. Atre, "Properties of SiC and AlN feedstocks for the powder injection moulding of thermal management devices," Powder Injection Moulding International, vol. 4, no. 3, pp. 64–70, 2010.

[11] X. Z. Shi, M. Huang, Z. F. Zhao, and C. Y. Shen, "Nonlinear fitting technology of 7-parameter Cross-WLF viscosity model," Advanced Materials Research, vol. 189–193, pp. 2103–2106, 2011.

[12] L. E. Nielsen, Predicting the properties of mixtures: mixture rules in science and engineering. M. Dekker, 1978.

[13] H. H. Chiang, C. A. Hieber, and K. K. Wang, "A unified simulation of the filling and postfilling stages in injection molding. Part I: Formulation," Polymer Engineering & Science, vol. 31, no. 2, pp. 116–124, 1991.

[14] A. Boudenne, L. Ibos, M. Fois, E. Gehin, and J. C. Majeste, "Thermophysical properties of polypropylene/aluminum composites," Journal of Polymer Science Part B: Polymer Physics, vol. 42, no. 4, pp. 722–732, 2004.

[15] D. T. Jamieson and G. Cartwright, Properties of Binary Liquid Mixtures: Heat Capacity. National Engineering Laboratory, 1978.

[16] B. Weidenfeller, M. Höfer, and F. R. Schilling, "Thermal conductivity, thermal diffusivity, and specific heat capacity of particle filled polypropylene," Composites Part A: Applied Science and Manufacturing, vol. 35, no. 4, pp. 423–429, 2004.

[17] G. Subodh, M. V. Manjusha, J. Philip, and M. T. Sebastian, "Thermal properties of polytetrafluoroethylene/$Sr_2Ce_2Ti_5O_{16}$ polymer/ceramic composites," Journal of Applied Polymer Science, vol. 108, no. 3, pp. 1716–1721, 2008.

[18] C. P. Wong and R. S. Bollampally, "Thermal conductivity, elastic modulus, and coefficient of thermal expansion of polymer composites filled with ceramic particles for electronic packaging," Journal of Applied Polymer Science, vol. 74, no. 14, pp. 3396–3403, 1999

[19] H. Ishida and S. Rimdusit, “Heat capacity measurement of boron nitride-filled polybenzoxazine: The composite structure-insensitive property,” Journal of Thermal Analysis and Calorimetry, vol. 58, no. 3, pp. 497–507, 1999.

[20] C. P. Wong and R. S. Bollampally, “Thermal conductivity, elastic modulus, and coefficient of thermal expansion of polymer composites filled with ceramic particles for electronic packaging,” Journal of Applied Polymer Science, vol. 74, no. 14, pp. 3396–3403, Dec. 1999.

[21] G.-W. Lee, M. Park, J. Kim, J. I. Lee, and H. G. Yoon, “Enhanced thermal conductivity of polymer composites filled with hybrid filler,” Composites Part A: Applied Science and Manufacturing, vol. 37, no. 5, pp. 727–734, 2006.

[22] D. C. Moreira, L. A. Sphaier, J. M. L. Reis, and L. C. S. Nunes, “Experimental investigation of heat conduction in polyester–Al_2O_3 and polyester–CuO nanocomposites,” Experimental Thermal and Fluid Science, vol. 35, no. 7, pp. 1458–1462, 2011.

[23] Y. Xu, D. D. Chung, and C. Mroz, “Thermally conducting aluminum nitride polymer-matrix composites,” Composites Part A: Applied Science and Manufacturing, vol. 32, no. 12, pp. 1749–1757, 2001.

[24] T. K. Dey and M. Tripathi, “Thermal properties of silicon powder filled high-density polyethylene composites,” Thermochimica Acta, vol. 502, no. 1–2, pp. 35–42, 2010.

[25] K. Sanada, Y. Tada, and Y. Shindo, “Thermal conductivity of polymer composites with close-packed structure of nano and micro fillers,” Composites Part A: Applied Science and Manufacturing, vol. 40, no. 6–7, pp. 724–730, 2009.

[26] P. Badrinarayanan and M. R. Kessler, “Zirconium tungstate/cyanate ester nanocomposites with tailored thermal expansivity,” Composites Science and Technology, vol. 71, no. 11, pp. 1385–1391, 2011.

[27] S. Tognana, W. Salgueiro, A. Somoza, J. A. Pomarico, and H. F. Ranea-Sandoval, “Influence of the filler content on the thermal expansion behavior of an epoxy matrix

particulate composite," Materials Science and Engineering: B, vol. 157, no. 1–3, pp. 26–31, 2009.

[28] S. Elomari, R. Boukhili, and D. J. Lloyd, "Thermal expansion studies of prestrained Al_2O_3/Al metal matrix composite," Acta Materialia, vol. 44, no. 5, pp. 1873–1882, 1996.

[29] K. H. Kate, R. K. Enneti, S. J. Park, R. M. German, and Sundar V. Atre, "Predicting powder-polymer mixture properties for PIM design," submitted to International Materials Reviews.

Chapter 5

Conclusions and Future Work

5.1 Conclusions

Feedstock properties presented in this work have been estimated using predictive models with limited experimental data. The properties were subsequently used in computer simulations to study the mold-filling behavior of aluminum nitride. During the course of research an in-depth literature search led to selecting specific rules of mixtures over a wide range of empirical models for each thermal, mechanical and rheological property. The selected rules of mixtures were curve fitted to experimental data and a coefficient of determination was calculated for data from each material system. The results of the analysis showed that the selected models had general applicability for a wide range of highly filled powder-polymer mixtures.

The selected models were used to predict the effect of filler content on the feedstock properties data for two aluminum nitride-polymer mixtures. The predicted properties helped to quantitatively understand the influence of material composition on mold-filling behavior using computer simulations performed on Autodesk Moldflow Insight software. The part weight increases with an increase in volume fraction of monomodal and bimodal AlN powders from 0.48 to 0.52 and 0.52 to 0.6 respectively. This increase in part weight with an increase in powder volume fraction can be attributed to an increase in density values with a rise in volume fractions of AlN. Similarly, an increase in peak injection pressure was observed for both monomodal and bimodal AlN feedstocks. Additionally, the heat sink substrate with fins required a higher injection pressure in comparison to the heat sink substrate without fins, presumably as a result of high volumetric flow rates. It was inferred that an increase in injection pressure directly increases the clamp force and correspondingly reduces the number of mold cavities that can be simultaneously filled on a molding machine. Further the addition of nanoparticles showed a significant effect on the rheological properties of the feedstock, as a result of an increase in the maximum packing density in the bimodal mixtures. The zero shear viscosity, melt density, solid

density, thermal conductivity, coefficient of thermal expansion, elastic and shear modulus increased with increase in volume fraction of the powders. Finally, the predictive models for estimating the compositional dependence of feedstock properties in conjunction with the computer simulations presented in this thesis can be used to design new materials, select component geometry attributes, and optimize process parameters while eliminating expensive and time-consuming trial-and-error practices prevalent in the area of powder injection molding.

5.2 Future Work

The current research demonstrated the use of predictive models to estimate AlN feedstock properties that are needed used to study the injection molding behavior and defect evolution in PIM components. One area of future research is to conduct experimental verification of the predicted data for feedstock properties presented in this thesis.

In the current research only a limited number of injection molding process parameters were used to perform computer simulations of the mold filling behavior of aluminum nitride powder mixtures. In the future, a wide range of input parameters could be tested for analyzing the mold-filling behavior and defect evolution. Further, there are additional computer simulation tools such as PIMSolver that have been developed for PIM that can be compared to the predictions of Moldflow and validated with molding experiments.

Bibliography

Bibliography

1. A. B. Metzner, “Rheology of suspensions in polymeric liquids,” Journal of Rheology, vol. 29, no. 6, pp. 739–775, 1985.
2. Boudenne, L. Ibos, M. Fois, E. Gehin, and J. C. Majeste, “Thermophysical properties of polypropylene/aluminum composites,” Journal of Polymer Science Part B: Polymer Physics, vol. 42, no. 4, pp. 722–732, 2004.
3. Christensen and S. Graham, “Thermal effects in packaging high power light emitting diode arrays,” Applied Thermal Engineering, vol. 29, no. 2–3, pp. 364–371, 2009.
4. B. Mutnuri, “Thermal Conductivity Characterization of Composite Materials,” West Virginia University, Morgantown, W. Va., 2006.
5. B. Weidenfeller, M. Höfer, and F. R. Schilling, “Thermal conductivity, thermal diffusivity, and specific heat capacity of particle filled polypropylene,” Composites Part A: Applied Science and Manufacturing, vol. 35, no. 4, pp. 423–429, 2004.
6. J. Cremers and H. A. Fine, Thermal Conductivity. Springer, 1991.
7. L. Hsieh and W. H. Tuan, “Elastic properties of ceramic–metal particulate composites,” Materials Science and Engineering: A, vol. 393, no. 1–2, pp. 133–139, 2005.
8. P. Wong and R. S. Bollampally, “Thermal conductivity, elastic modulus, and coefficient of thermal expansion of polymer composites filled with ceramic particles for electronic packaging,” Journal of Applied Polymer Science, vol. 74, no. 14, pp. 3396–3403, Dec. 1999.
9. R. W. Macosko, Rheology: principles, measurements, and applications. VCH, 1994.
10. C. Moreira, L. A. Sphaier, J. M. L. Reis, and L. C. S. Nunes, “Experimental investigation of heat conduction in polyester–Al2O3 and polyester–CuO nanocomposites,” Experimental Thermal and Fluid Science, vol. 35, no. 7, pp. 1458–1462, 2011.
11. D. F. Heaney, “Handbook of Metal Injection Molding”, Woodhead Publishing Limited, Cambridge, UK, 2012.

12. D. T. Jamieson and G. Cartwright, Properties of Binary Liquid Mixtures: Heat Capacity. National Engineering Laboratory, 1978.
13. D. W. Sundstrom and Y.-D. Lee, “Thermal conductivity of polymers filled with particulate solids,” Journal of Applied Polymer Science, vol. 16, no. 12, pp. 3159–3167, 1972.
14. E. Logakis, C. Pandis, P. Pissis, J. Pionteck, and P. Pötschke, “Highly conducting poly(methyl methacrylate)/carbon nanotubes composites: Investigation on their thermal, dynamic-mechanical, electrical and dielectric properties,” Composites Science and Technology, vol. 71, no. 6, pp. 854–862, 2011.
15. F. Reynaud, T. Jouen, C. Gauthier, G. Vigier, and J. Varlet, “Nanofillers in polymeric matrix: a study on silica reinforced PA6,” Polymer, vol. 42, no. 21, pp. 8759–8768, 2001.
16. G. Dlubek, U. De, J. Pionteck, N. Y. Arutyunov, M. Edelmann, and R. Krause-Rehberg, “Temperature dependence of free volume in pure and silica-filled poly(dimethyl siloxane) from positron lifetime and PvT experiments,” Macromolecular Chemistry and Physics, vol. 206, no. 8, pp. 827–840, 2005.
17. G. Subodh, M. V. Manjusha, J. Philip, and M. T. Sebastian, “Thermal properties of polytetrafluoroethylene/$Sr_2Ce_2Ti5O_{16}$ polymer/ceramic composites,” Journal of Applied Polymer Science, vol. 108, no. 3, pp. 1716–1721, 2008.
18. W. Brassell and K. B. Wischmann, “Mechanical and thermal expansion properties of a participate filled polymer,” Journal of Materials Science, vol. 9, no. 2, pp. 307–314, 1974.
19. G. W. Lee, M. Park, J. Kim, J. I. Lee, and H. G. Yoon, “Enhanced thermal conductivity of polymer composites filled with hybrid filler,” Composites Part A: Applied Science and Manufacturing, vol. 37, no. 5, pp. 727–734, 2006.
20. H. Chiang, C. A. Hieber, and K. K. Wang, “A unified simulation of the filling and postfilling stages in injection molding. Part I: Formulation,” Polymer Engineering & Science, vol. 31, no. 2, pp. 116–124, 1991.

21. Ishida and S. Rimdusit, “Heat capacity measurement of boron nitride-filled polybenzoxazine: The composite structure-insensitive property,” Journal of Thermal Analysis and Calorimetry, vol. 58, no. 3, pp. 497–507, 1999.
22. H. S. Jaggi, Y. Kumar, B. K. Satapathy, A. R. Ray, and A. Patnaik, “Analytical interpretations of structural and mechanical response of high density polyethylene/hydroxyapatite bio-composites,” Materials & Design, vol. 36, no. 0, pp. 757–766, 2012.
23. S. Balać, M. Milovančević, C. Tang, P. S. Uskoković, and D. P. Uskoković, “ Estimation of elastic properties of a particulate polymer composite using a face-centered cubic FE model,” Materials Letters, vol. 58, no. 19, pp. 2437‑2441, 2004.
24. J. Spanoudakis, and R. J.Young, “Crack propagation in a glass particle-filled epoxy resin Part 1. Effect of particle volume fraction and size : Journal of Materials Science Vol 19 (1984) pp 473–486,” Composites, vol. 15, no. 3, p. 242, 1984.
25. J. Chen, J. G. Mi, and K. Y. Chan, “Comparison of different mixing rules for prediction of density and residual internal energy of binary and ternary Lennard–Jones mixtures,” Fluid Phase Equilibria, vol. 178, no. 1–2, pp. 87–95, Mar. 2001.
26. J. Lenz, R. K. Enneti, V. P. Onbattuvelli, K. Kate, R. Martin, and S. V. Atre, " Powder injection molding of ceramic engine components for transportation," JOM, vol. 64, pp. 388-392, 2012.
27. Z. Liang, “Viscoelastic properties and characterization of inorganic particulate-filled polymer composites,” Journal of Applied Polymer Science, vol. 114, no. 6, pp. 3955–3960, 2009.
28. C. Yung, B. L. Zhu, T. M. Yue, and C. S. Xie, “Preparation and properties of hollow glass microsphere-filled epoxy-matrix composites,” Composites Science and Technology, vol. 69, no. 2, pp. 260–264, 2009.
29. K. H. Kate, R. K. Enneti, S. J. Park, R. M. German, and Sundar V. Atre, “Predicting powder-polymer mixture properties for PIM design,” submitted to International Materials Reviews.

30. K. H. Kate, V. P. Onbattuvelli, R. K. Enneti, S. W. Lee, S.-J. Park, and S. V. Atre, “Measurements of powder–polymer mixture properties and their use in powder injection molding simulations for aluminum nitride,” JOM, vol. 64, no. 9, pp. 1048–1058, 2012.
31. K. PourAkbar Saffar, A. R. Arshi, N. JamilPour, A. R. Najafi, G. Rouhi, and L. Sudak, “A cross-linking model for estimating Young’s modulus of artificial bone tissue grown on carbon nanotube scaffold,” Journal of Biomedical Materials Research Part A, vol. 94A, no. 2, pp. 594–602, 2010.
32. K. Sanada, Y. Tada, and Y. Shindo, “Thermal conductivity of polymer composites with close-packed structure of nano and micro fillers,” Composites Part A: Applied Science and Manufacturing, vol. 40, no. 6–7, pp. 724–730, 2009.
33. K.H. Kate, V.P. Onbattuvelli, R.K. Enneti, S.W. Lee, S. J. Park, and S.V. Atre, “Measurements of powder–polymer mixture properties and their use in powder injection molding simulations for aluminum nitride,” Journal of the Minerals, Metals and Materials Society (JOM), Vol. 64, No. 9, pp. 1048-1058, 2012.
34. R. E. Nielsen, Predicting the properties of mixtures: mixture rules in science and engineering. M. Dekker, 1978.
35. M. McGrath, R. S. Parnas, S. H. King, J. L. Schroeder, D. A. Fischer, and J. L. Lenhart, “Investigation of the thermal, mechanical, and fracture properties of alumina–epoxy composites,” Polymer, vol. 49, no. 4, pp. 999–1014, 2008.
36. A. Osman and A. Atallah, “Interparticle and particle–matrix interactions in polyethylene reinforcement and viscoelasticity,” Polymer, vol. 46, no. 22, pp. 9476–9488, 2005.
37. A. Abu-Abdeen, “Static and dynamic mechanical properties of poly(vinyl chloride) loaded with aluminum oxide nanopowder,” Materials & Design, vol. 33, no. 0, pp. 523–528, 2012.
38. M. J. Edirisinghe and J. R. G. Evans, “Review: Fabrication of engineering ceramics by injection moulding. I. Materials selection,” International Journal of High Technology Ceramics, vol. 2, no. 1, pp. 1–31, 1986.

39. M. Wang, C. Berry, M. Braden, and W. Bonfield, “Young’s and shear moduli of ceramic particle filled polyethylene,” Journal of Materials Science and Materials in Medicine, vol. 9, no. 11, pp. 621–624, 1998.
40. S. Badrinarayanan and M. R. Kessler, “Zirconium tungstate/cyanate ester nanocomposites with tailored thermal expansivity,” Composites Science and Technology, vol. 71, no. 11, pp. 1385–1391, 2011.
41. G. Hiemenz and R. Rajagopalan, Principles of Colloid and Surface Chemistry. CRC Press, 1997.
42. J. Yoon, T. D. Fornes, and D. R. Paul, “Thermal expansion behavior of nylon 6 nanocomposites,” Polymer, vol. 43, no. 25, pp. 6727–6741, 2002.
43. D. Arefinia and A. Shojaei, “On the viscosity of composite suspensions of aluminum and ammonium perchlorate particles dispersed in hydroxyl terminated polybutadiene-New empirical model,” J Colloid Interface Sci, vol. 299, no. 2, pp. 962–971, 2006.
44. K. Enneti , S. J. Park , R. M. German, S. V.Atre, “Review: thermal debinding process in particulate materials processing”, Materials and Manufacturing Processes, 27: 103–118, 2012.
45. R. K. Enneti, S. J. Park, J. Palagi de Souza, and S. V. Atre, "Critical issues in manufacturing dental brackets by powder injection molding," International Journal of Powder Metallurgy, , vol. 48, no. 2, pp. 23-29, 2012.
46. R. K. Goyal, A. N. Tiwari, U. P. Mulik, and Y. S. Negi, “Novel high performance Al2O3/poly(ether ether ketone) nanocomposites for electronics applications,” Composites Science and Technology, vol. 67, no. 9, pp. 1802–1812, 2007.
47. R. K. Sinnott, J. M. Coulson, and J. F. Richardson, Chemical engineering design. Butterworth-Heinemann, 2005.
48. R. M. German and S. J. Park, Mathematical Relations in Particulate Materials Processing: Ceramics, Powder Metals, Cermets, Carbides, Hard Materials, and Minerals. John Wiley & Sons, 2008.
49. R. M. German, “Powder Metallurgy Science”, Metal Powder Industries Federation, 105 College Rd. E, Princeton, N. J. 08540, U. S. A, 1984.

50. R. M. German, Powder injection molding : design and applications. State College, PA: Innovative Material Solutions, 2003.
51. R. Urval, S. Lee, S. V. Atre, S.-J. Park, and R. M. German, “Optimisation of process conditions in powder injection moulding of microsystem components using a robust design method: Part I. primary design parameters,” Powder Metallurgy, vol. 51, no. 2, pp. 133–142, 2008.
52. R. Urval, S. Lee, S. V. Atre, S.-J. Park, and R. M. German, “Optimisation of process conditions in powder injection moulding of microsystem components using robust design method Part 2 – Secondary design parameters,” Powder Metallurgy, vol. 53, no. 1, pp. 71–81, 2010.
53. S. Ahn, S. J. Park, S. Lee, S. V. Atre, and R. M. German, “Effect of powders and binders on material properties and molding parameters in iron and stainless steel powder injection molding process,” Powder Technology, vol. 193, no. 2, pp. 162–169, 2009.
54. S. Areerat, Y. Hayata, R. Katsumoto, T. Kegasawa, H. Egami, and M. Ohshima, “Solubility of carbon dioxide in polyethylene/titanium dioxide composite under high pressure and temperature,” Journal of Applied Polymer Science, vol. 86, no. 2, pp. 282–288, 2002.
55. S. Elomari, R. Boukhili, and D. J. Lloyd, “Thermal expansion studies of prestrained Al2O3/Al metal matrix composite,” Acta Materialia, vol. 44, no. 5, pp. 1873–1882, 1996.
56. S. J. Feltham, B. Yates, and R. J. Martin, “The thermal expansion of particulate-reinforced composites,” Journal of Materials Science, vol. 17, no. 8, pp. 2309–2323, 1982.
57. S. J. Park, S. Ahn, T. G. Kang, S. T. Chung, Y. S. Kwon, S. H. Chung, S. G. Kim, S. Kim, S. V. Atre, S. Lee, and R. M. German, “A review of computer simulations in powder injection molding,” International Journal of Powder Metallurgy, vol. 46, no. 3, pp. 37–46, 2010.

58. S. McGee and R. L. McGullough, “Combining rules for predicting the thermoelastic properties of particulate filled polymers, polymers, polyblends, and foams,” Polymer Composites, vol. 2, no. 4, pp. 149–161, 1981.
59. S. Mishra, S. H. Sonawane, and R. P. Singh, “Studies on characterization of nano CaCO3 prepared by the in situ deposition technique and its application in PP-nano CaCO3 composites,” Journal of Polymer Science Part B: Polymer Physics, vol. 43, no. 1, pp. 107–113, 2005.
60. S. Rajesh, K. P. Murali, H. Jantunen, and R. Ratheesh, “The effect of filler on the temperature coefficient of the relative permittivity of PTFE/ceramic composites,” Physica B: Condensed Matter, vol. 406, no. 22, pp. 4312–4316, 2011.
61. S. Tognana, W. Salgueiro, A. Somoza, J. A. Pomarico, and H. F. Ranea-Sandoval, “Influence of the filler content on the thermal expansion behavior of an epoxy matrix particulate composite,” Materials Science and Engineering: B, vol. 157, no. 1–3, pp. 26–31, 2009.
62. S. V. Atre, S. J. Park, R. Zauner, and R. M. German, “Process simulation of powder injection moulding: identification of significant parameters during mould filling phase,” Powder Metallurgy, vol. 50, no. 1, pp. 76–85, 2007.
63. P. Fornes and D. R. Paul, “Modeling properties of nylon 6/clay nanocomposites using composite theories,” Polymer, vol. 44, no. 17, pp. 4993–5013, 2003.
64. T. J. Wooster, S. Abrol, J. M. Hey, and D. R. MacFarlane, “Thermal, mechanical, and conductivity properties of cyanate ester composites,” Composites Part A: Applied Science and Manufacturing, vol. 35, no. 1, pp. 75–82, 2004.
65. T. K. Dey and M. Tripathi, “Thermal properties of silicon powder filled high-density polyethylene composites,” Thermochimica Acta, vol. 502, no. 1–2, pp. 35–42, 2010.
66. T. Zhang and J. R. G. Evans, “Predicting the viscosity of ceramic injection moulding suspensions,” Journal of the European Ceramic Society, vol. 5, no. 3, pp. 165–172, 1989.

67. T. Zhang and J. R. G. Evans, “Thermal expansion and equation of state for ceramic injection moulding suspensions,” Journal of the European Ceramic Society, vol. 6, no. 1, pp. 15–21, 1990.
68. T. Zhang, J. R. G. Evans, and K. K. Dutta, “Thermal properties of ceramic injection moulding suspensions in the liquid and solid states,” Journal of the European Ceramic Society, vol. 5, no. 5, pp. 303–309, 1989.
69. L. Carrubba, M. Bulters, and W. Zoetelief, “Dependence of coefficient of volumetric thermal expansion (CVTE) of glass fiber reinforced (GFR) polymers on the glass fiber content,” Polymer Bulletin, vol. 59, no. 6, pp. 813–824, 2008.
70. V. P. Onbattuvelli, “The effects of nanoparticle addition on the processing, structure and properties of SiC and AlN,” Thesis/Dissertation, 2010.
71. V. P. Onbattuvelli, R. K. Enneti, and S. V. Atre, “The effects of nanoparticle addition on the sintering and properties of bimodal μ-n AlN”, Ceramics International, Volume 38, Issue 8, pp. 6495‑6499, 2012.
72. V. P. Onbattuvelli, R. K. Enneti, and S. V. Atre, “The effects of nanoparticle addition on the densification and properties of SiC”, Ceramics International, Volume 38, Issue 7, pp. 5393–5399, 2012.
73. V. P. Onbattuvelli, R. K. Enneti, S. J. Park, and S. V. Atre, “The effects of nanoparticle addition on SiC and AlN powder–polymer mixtures: Packing and flow behavior” Int. Journal of Refractory Metals and Hard Materials 36,77–84, 2013.
74. V. P. Onbattuvelli, S. Vallury, T. McCabe, S. J. Park, and S. Atre, “Properties of SiC and AlN feedstocks for the powder injection moulding of thermal management devices,” Powder Injection Moulding International, vol. 4, no. 3, pp. 64–70, 2010.
75. V. P. Onbattuvelli, S. Vallury, T. McCabe, S. J. Park, and S. Atre, “Properties of SiC and AlN feedstocks for the powder injection moulding of thermal management devices,” Powder Injection Moulding International, vol. 4, no. 3, pp. 64–70, 2010.
76. T. Wu, K. Sadeghipour, K. Boberick, and G. Baran, “Predictive modeling of elastic properties of particulate-reinforced composites,” Materials Science and Engineering: A, vol. 332, no. 1–2, pp. 362–370, 2002.

77. W. Zhou, C. Wang, Q. An, and H. Qu, “Thermal properties of heat conductive silicone rubber filled with hybrid fillers,” Journal of Composite Materials, vol. 42, no. 2, pp. 173–187, 2008.
78. Z. Shi, M. Huang, Z. F. Zhao, and C. Y. Shen, “Nonlinear Fitting Technology of 7-Parameter Cross-WLF Viscosity Model,” Advanced Materials Research, vol. 189–193, pp. 2103–2106, Feb. 2011.
79. P. Mamunya, “Electrical and thermal conductivity of polymers filled with metal powders,” European Polymer Journal, vol. 38, no. 9, p. 1887, Sep. 2002.
80. Y. Xu, D. D. Chung, and C. Mroz, “Thermally conducting aluminum nitride polymer-matrix composites,” Composites Part A: Applied Science and Manufacturing, vol. 32, no. 12, pp. 1749–1757, 2001.
81. Y. Zhang, Z. Shen, and Z. Tong, “Thermal Conductivity and Interfacial Thermal Barrier Resistance of the Particle Reinforced Metal Matrix Composites,” in Electronic Packaging Technology, 2007. ICEPT 2007. 8th International Conference on, 2007, pp. 1 –4.
82. K. Zhu, Y. Yang, J. Yin, and Z. N. Qi, “Preparation and properties of organosoluble polyimide/silica hybrid materials by sol–gel process,” Journal of Applied Polymer Science, vol. 73, no. 14, pp. 2977–2984, 1999.

Appendices

Appendix A1: Properties of Monomodal µ-AlN Feedstock

Table A.1 Feedstock composition of µ- AlN Feedstock.

Materials	Particle size	Weight (%)
AlN	1.1 µm	76
Y_2O_3	50 nm	4
Multi-component binder system	-	20

Client	Valmikanathan Onbattuvelli
Company	Oregon State University
Address	Hall
	Corvallis, OR
	United States
Sample Received	3/6/2009
Sample Source	Oregon State University
Report Prepared	3/11/2009
Prepared By	
Title	Engineer
Issued By	
Title	Operations Manager

DatapointLabs is accredited by the American Association for Laboratory Accreditation (A2LA Certificate # 1242.01), and maintains a quality system in accordance with ISO/IEC 17025. Any opinions or interpretations expressed in this report are outside the scope of the accreditation.

The results in this report relate only to the items tested. This report shall not be reproduced except in full without the written approval of DatapointLabs.

DatapointLabs cannot be held liable under any circumstances for damages arising out of the use of this information or for claims in excess of that originally paid for the testing. DatapointLabs disclaims all other warranties, either express or implied, including implied warranties of merchantability or fitness for a particular purpose.

DatapointLabs

http://www.datapointlabs.com

95 Brown Road, Ithaca, NY 14850
Phone: 607-266-0405 Fax: 607-266-0168
Toll-Free (U.S.): 1-888-328-2422

This data is available in True Digital format

dds matereality www.matereality.com

C-MOLD/Moldflow *TestPak™* Results

< 14922.21000.udb

Analysis	Property & T-CODE	Value	Units
Filling & Cooling	Cross/WLF Model (01313):		
	n	0.37760	
	τ^*	1.178E+02	Pa
	D1	8.777E+10	Pa•s
	D2	263	K
	D3	0	K/Pa
	A1	14.24	
	A2	51.60	K
	Juncture Loss Constants (01360):		
	C1		Pa^(1-C2)
	C2		
	Melt Density (01000)	1943	kg/m^3
	Melt Specific Heat (01100)	1201	J/kg•K
	Melt Thermal Conductivity (01200)	2.202	W/m•K
	Transition Temperature (01500)	326	K
	Specific Heat Table (01101)	See Page 7	
	Thermal Conductivity Table (01201)	See Page 8	
Post-Filling	Two-Domain Tait PVT Model (01004):		
	b5	3.310E+02	K
	b6	1.650E-07	K/Pa
	b1m	4.834E-04	m^3/kg
	b2m	2.998E-07	$m^3/kg•K$
	b3m	2.865E+08	Pa
	b4m	4.818E-03	1/K
	b1s	4.686E-04	m^3/kg
	b2s	9.700E-08	$m^3/kg•K$
	b3s	5.791E+08	Pa
	b4s	1.260E-03	1/K
	b7	1.485E-05	m^3/kg
	b8	1.101E-01	1/K
	b9	2.118E-08	1/Pa
Shrink / Warp - Uncorrected Stress	Anisotropic Mechanical Properties (01602)		
	Modulus E_1 (flow direction)		MPa
	Modulus E_2 (transverse direction)		MPa
	Poisson's ratio ν_{12}		
	Poisson's ratio ν_{23}		
	Shear Modulus G		MPa
	Anisotropic Thermal Expansion (01702)		
	CLTE α_1 (flow direction)		x 10E-6/°C
	CLTE α_2 (transverse direction)		x 10E-6/°C

Viscosity

Method	ASTM D 3835: 2008 Determination of Properties of Polymeric Materials by Means of a Capillary Rheometer	
Instrument	Goettfert Rheograph 2003 Capillary Rheometer	
Specimen	type	pellets
	drying	none
	other preparation	none
Parameters	initial pressure	0 MPa
	barrel diameter	12 mm
	die entry angle	180 °
	die inner diameter	1 mm
	die length	20 mm
	preheating time	6 min
Data Correction	Rabinowitsch	
Precision	temperature	+/- 0.1 °C
	die inner diameter	+/- 0.0069 mm
	die length	+/- 0.026 mm
Uncertainty	per standard	

Polymer rheology characterizes the complex flow behavior of plastics. A capillary rheometer measures viscosity as a function of temperature and shear rate. The Goettfert rheometer utilizes direct measurement of melt pressures through a side mounted pressure transducer.

Data are modeled using empirical or semi-empirical equations.

Viscosity Data

140 °C		*150 °C*		*160 °C*	
Shear Rate s^{-1}	**Viscosity Pa·s**	**Shear Rate s^{-1}**	**Viscosity Pa·s**	**Shear Rate s^{-1}**	**Viscosity Pa·s**
11	1186.94	11	1024.46	11	1050.63
30	599.80	31	498.11	29	578.00
77	331.05	69	308.43	76	311.42
153	199.41	145	197.27	173	165.99
311	129.61	332	110.43	300	116.03
689	80.68	747	65.39	745	69.71
1434	52.81	1335	47.10	1479	42.53
2932	33.11	2839	31.40	2766	30.47
6669	21.52	6868	18.85	6914	18.72
13113	14.90	13574	12.69	14453	11.49

Cross/WLF Model (C-MOLD, Moldflow)

$$\eta(T,\dot{\gamma}) = \frac{\eta_0(T)}{1+\left(\frac{\eta_0\dot{\gamma}}{\tau^*}\right)^{1-n}}, \text{where}$$

$$\eta_0(T) = D_1 \exp\left(-\frac{A_1(T-D_2)}{A_2+(T-D_2)}\right)$$

Coefficients (SI units)

n	0.37760
τ^*	117.773
D1	8.78E+10
D2	263
A1	14.24
A2	51.6

Viscosity vs Shear Rate

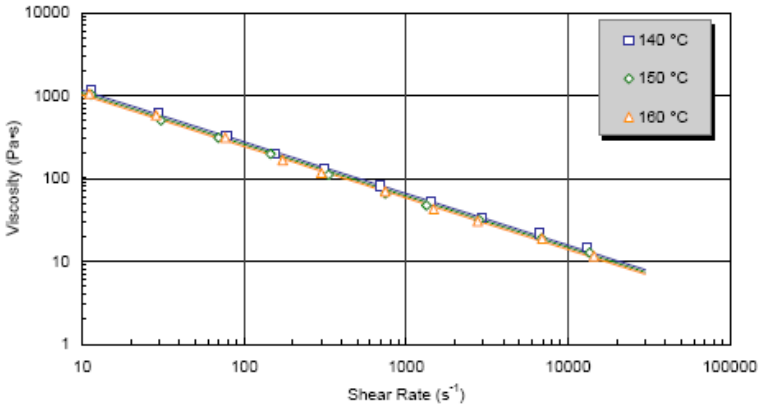

Viscosity vs Temperature

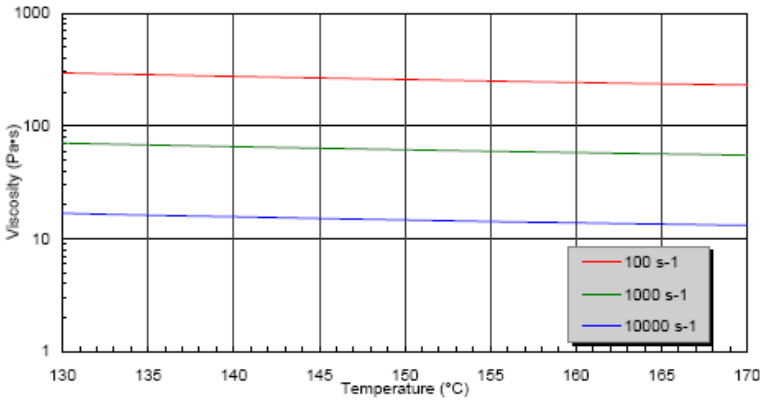

Specific Heat

Method	Based on ASTM E1269: 2005 Determining Specific Heat Capacity by Differential Scanning Calorimetry	
Instrument	Perkin Elmer DSC7	
Specimen	type	pellets
	drying	none
	other preparation	cut from pellet
Parameters	purge gas	N2
	purge gas purity	99.99 %
	purge gas rate	25 ml/min
	cooling rate	20 °C/min
	initial temperature	160 °C
	final temperature	0 °C
	equilibration times	4 min
	sample weight	10.57 mg
	sample pans	Al, volatile
Calibration Standards	temperature	In, Zn
	heat flow	In
	specific heat	sapphire

Notes: Two peaks were observed. Transition analysis temperatures and specific heat data are for larger peak.

Heat capacity is a thermodynamic quantity and is a measure of the amount of heat retained by the material. The DSC can measure this property over a range of temperatures and in both solid and melt states.

Transition Analysis

extrapolated onset	53 °C
peak	49 °C
extrapolated end	41 °C

Specific Heat Data

Temp °C	Cp J/kg•K
150	1210
101	1125
58	1090
49	2811
31	1377
25	1114
10	918

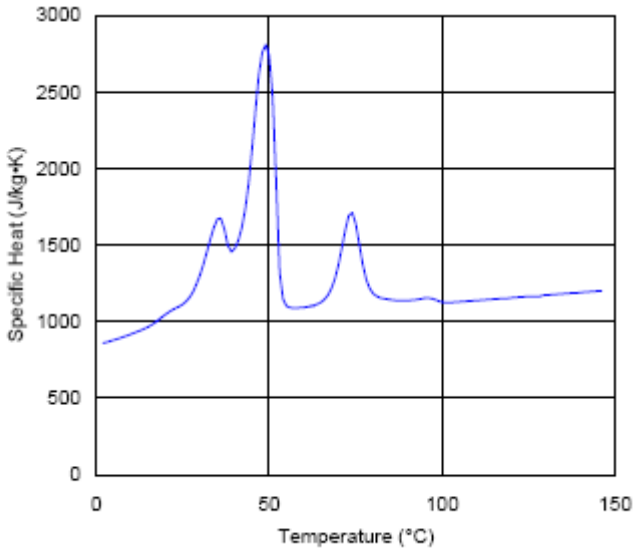

Thermal Conductivity

Method	ASTM D 5930: 2001 Thermal Conductivity of Plastics by Means of a Transient Line-Source Technique	
Instrument	K-System II Thermal Conductivity System	
Specimen	type	pellets
	drying	none
	other preparation	none
Parameters	calibration material	60,000 cstk PDMS
	probe constant	0.743
	probe length	50 mm
	loading temperature	150 °C
	initial temperature	160 °C
	final temperature	30 °C
	probe voltage	3.5 V
	acquisition time	45 s
Uncertainty	per standard	

Thermal conductivity is a measure of the rate of heat conduction of the material. It is a critical property for heat transfer calculations. The line-source method measures thermal conductivity in both melt and solid state.

Thermal Conductivity Data

Temp °C	k W/m•K
163	2.503
144	2.045
124	2.058
104	2.661
83	2.234
63	3.834
42	4.263

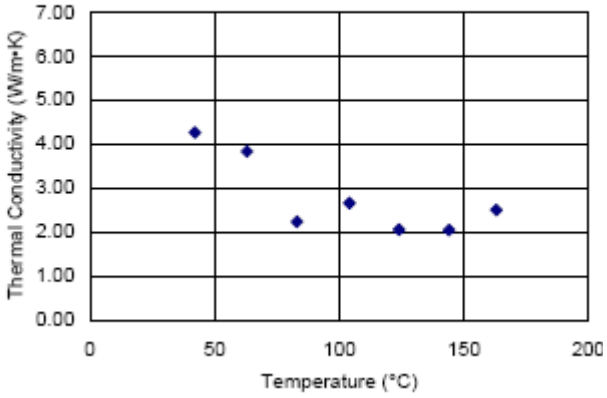

PVT

Method	Non-standard. Pressure-specific volume-temperature measurements using high-pressure dilatometry	
Instrument	Gnomix PVT apparatus	
Specimen	type	pellets
	drying	4 hrs, 50°C/vacuum
	other preparation	see note below
Parameters	solid density method	ASTM D792
	immersion liquid	water
	pvT confining fluid	mercury
	max temperature	160 °C
	measurement type	isothermal heating scan
	heating rate	approx. 3 °C/min

PVT data are equation-of-state thermodynamic properties that describe the compressibility and volumetric expansion of the material. Dilatometry measures the change in volume of a specimen subjected to different temperatures and pressures.

Notes: PVT specimen was cut from a plug that was manufactured by Datapoint Labs using pellets supplied by client.

Pressure-Volume-Temperature Data

Specific Volume cm3/g

Temp	Pressure MPa					
°C	0	40	80	120	160	200
23	0.4658	0.4623	0.4600	0.4577	0.4557	0.4539
32	0.4674	0.4634	0.4607	0.4582	0.4561	0.4542
41	0.4700	0.4652	0.4615	0.4591	0.4568	0.4549
52	0.4747	0.4692	0.4638	0.4603	0.4580	0.4557
56	0.4782	0.4716	0.4654	0.4613	0.4586	0.4562
72	0.4892	0.4825	0.4735	0.4670	0.4621	0.4585
86	0.4930	0.4855	0.4799	0.4754	0.4689	0.4636
101	0.4971	0.4887	0.4825	0.4778	0.4738	0.4705
116	0.5014	0.4924	0.4855	0.4805	0.4761	0.4726
132	0.5069	0.4964	0.4891	0.4832	0.4786	0.4749
147	0.5120	0.5009	0.4933	0.4875	0.4827	0.4786
162	0.5154	0.5033	0.4952	0.4894	0.4846	0.4806

Modified Two-Domain Tait Model (C-MOLD, Moldflow)

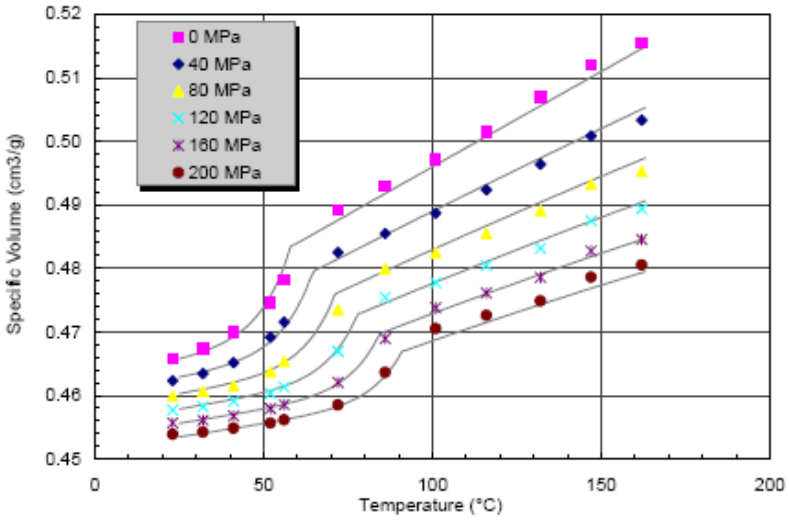

Coefficients	
b5	5.80E+01
b6	1.65E-01
b1m	4.834E-01
b2m	2.998E-04
b3m	2.865E+02
b4m	4.818E-03
b1s	4.686E-01
b2s	9.700E-05
b3s	5.791E+02
b4s	1.260E-03
b7	1.49E-02
b8	1.101E-01
b9	2.118E-02

Modified Two-Domain Tait Equation

$$v(T,p) = v_0(T)\left(1 - C\ln\left(1 + \frac{p}{B(T)}\right)\right) + v_t(T,p), T_t(p) = b_5 + b_6 p$$

for $T > T_t(p)$: $v_0(T) = b_{1m} + b_{2m}(T - b_5)$, $B(T) = b_{3m}\exp(-b_{4m}(T - b_5))$, $v_t(T,p) = 0$

for $T < T_t(p)$: $v_0(T) = b_{1s} + b_{2s}(T - b_5)$, $B(T) = b_{3s}\exp(-b_{4s}(T - b_5))$, $v_t(T,p) = b_7\exp(b_8(T - b_5) - b_9 p)$

Model Terms	Units
specific volume, v	cm3/g
pressure, P	MPa
temperature, T	°C

No-Flow Temperature

Method	non-standard Moldflow specification; no-flow temperature defined by extrudate flow < 2 mm/min	
Instrument	Goettfert Capillary Rheometer	
Specimen	type	pellets
	drying	none
	other preparation	none
Parameters	equivalent load	172 kg
	barrel diameter	12 mm
	initial pressure	0 MPa
	test temperature	140 °C
	dwell time	6 min
	die inner diameter	1 mm
	die length	20 mm
	die entry angle	180 °

The no-flow temperature provides a measure of the solidification temperature of the melt. During the test, a molten specimen is cooled under constant load; the no-flow temperature is one at which flow ceases to occur.

Results

No-Flow Temperature	61 °C

Appendix A2: Properties of Bimodal µ-n AlN Feedstock

Table A.2 Feedstock composition of µ-n AlN Feedstock

Materials	Particle size	Weight (%)
AlN	1.1 µm	70
	20 nm	10.75
Y_2O_3	50 nm	4.25
Multi-component binder system	-	15

Client	Valmikanathan Onbattuvelli
Company	Oregon State University
Address	Hall
	Corvallis, OR
	United States
Sample Received	6/11/2010
Sample Source	Oregon State University
Report Prepared	6/17/2010
Prepared By	
Title	Engineer
Issued By	
Title	Operations Manager

DatapointLabs is accredited by the American Association for Laboratory Accreditation (A2LA Certificate # 1242.01), and maintains a quality system in accordance with ISO/IEC 17025. Any opinions or interpretations expressed in this report are outside the scope of the accreditation.

The results in this report relate only to the items tested. This report shall not be reproduced except in full without the written approval of DatapointLabs.

DatapointLabs cannot be held liable under any circumstances for damages arising out of the use of this information or for claims in excess of that originally paid for the testing. DatapointLabs disclaims all other warranties, either express or implied, including implied warranties of merchantability or fitness for a particular purpose.

DatapointLabs

http://www.datapointlabs.com

95 Brown Road, Ithaca, NY 14850
Phone: 607-266-0405 Fax: 607-266-0168
Toll-Free (U.S.): 1-888-328-2422

This data is available in True Digital format

dds matereality
www.matereality.com

C-MOLD/Moldflow *TestPak*™ Results

16882.21000.udb

Analysis	Property & T-CODE	Value	Units
Filling & Cooling	Cross/WLF Model (01313):		
	n	0.05342	
	τ*	1.782E+05	Pa
	D1	9.133E+19	Pa•s
	D2	263	K
	D3	0	K/Pa
	A1	29.54	
	A2	51.60	K
	Juncture Loss Constants (01360):		
	C1		Pa^(1-C2)
	C2		
	Melt Density (01000)	2137	kg/m^3
	Melt Specific Heat (01100)	1411	J/kg•K
	Melt Thermal Conductivity (01200)	2.914	W/m•K
	Transition Temperature (01500)	326	K
	Specific Heat Table (01101)	See Page 7	
	Thermal Conductivity Table (01201)	See Page 8	
Post-Filling	Two-Domain Tait PVT Model (01004):		
	b5	3.360E+02	K
	b6	1.450E-07	K/Pa
	b1m	4.457E-04	m^3/kg
	b2m	1.861E-07	$m^3/kg•K$
	b3m	3.430E+08	Pa
	b4m	4.028E-03	1/K
	b1s	4.368E-04	m^3/kg
	b2s	1.494E-07	$m^3/kg•K$
	b3s	5.000E+08	Pa
	b4s	1.000E-02	1/K
	b7	8.936E-06	m^3/kg
	b8	1.306E-01	1/K
	b9	2.221E-08	1/Pa
Shrink / Warp - Uncorrected Stress	Anisotropic Mechanical Properties (01602)		
	Modulus E_1 (flow direction)		MPa
	Modulus E_2 (transverse direction)		MPa
	Poisson's ratio ν_{12}		
	Poisson's ratio ν_{23}		
	Shear Modulus G		MPa
	Anisotropic Thermal Expansion (01702)		
	CLTE α_1 (flow direction)		x 10E-6/°C
	CLTE α_2 (transverse direction)		x 10E-6/°C

Viscosity

Method	ASTM D 3835: 2008 Determination of Properties of Polymeric Materials by Means of a Capillary Rheometer	
Instrument	Goettfert Rheograph 2003 Capillary Rheometer	
Specimen	type	pellets
	drying	none
	other preparation	none
Parameters	initial pressure	0 MPa
	barrel diameter	12 mm
	die entry angle	180 °C
	die inner diameter	1 mm
	die length	20 mm
	preheating time	6 min
Data Correction		
Precision	temperature	+/- 0.1 °C
	die inner diameter	+/- 0.0069 mm
	die length	+/- 0.025 mm
Uncertainty	per standard	

Polymer rheology characterizes the complex flow behavior of plastics. A capillary rheometer measures viscosity as a function of temperature and shear rate. The Goettfert rheometer utilizes direct measurement of melt pressures through a side mounted pressure transducer.

Data are modeled using empirical or semi-empirical equations.

Notes: Pressures were unstable during all of this tesing.

Viscosity Data

140 °C		*160 °C*		*180 °C*	
Shear Rate s^{-1}	Viscosity Pa·s	Shear Rate s^{-1}	Viscosity Pa·s	Shear Rate s^{-1}	Viscosity Pa·s
10	26260.20	10	50997.10	10	32231.20
20	27539.70	20	25650.90	20	17456.00
50	11468.70	50	5471.77	50	9038.20
100	7126.74	100	3914.52	100	4574.06
200	2494.66	200	1795.43	200	1783.21
500	796.34	500	884.28	500	903.82
1000	398.12	1000	421.94	1000	612.45
2000	220.45	2000	169.46	2000	232.96
5000	102.10	5000	62.90	5000	68.51
10000	56.85	10000	44.21	10000	36.46

Cross/WLF Model (C-MOLD, Moldflow)

$$\eta(T,\dot{\gamma}) = \frac{\eta_0(T)}{1+\left(\frac{\eta_0\dot{\gamma}}{\tau^*}\right)^{1-n}}, where$$

$$\eta_0(T) = D_1 \exp\left[-\frac{A_1(T-D_2)}{A_2+(T-D_2)}\right]$$

Coefficients (SI units)

n	0.05342
τ*	178204.72
D1	9.133E+19
D2	263
A1	29.54
A2	51.6

Viscosity vs Shear Rate

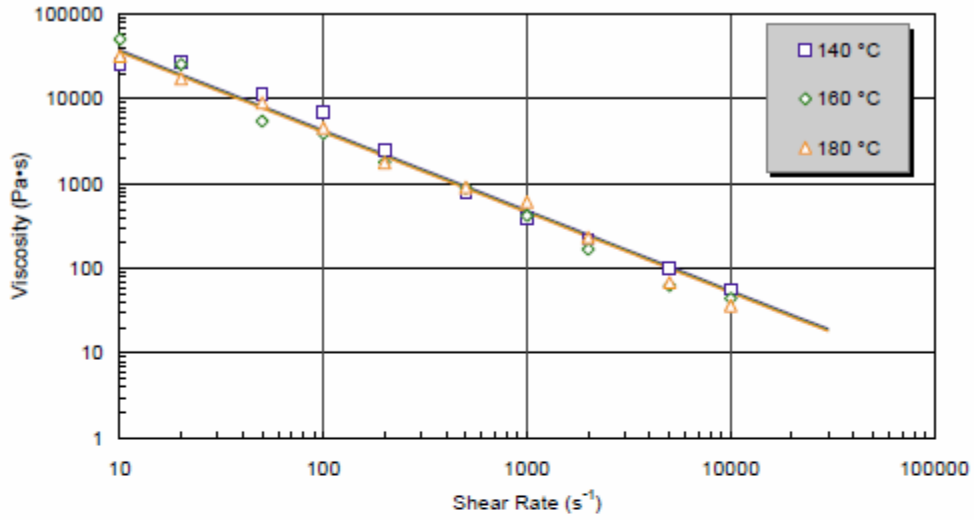

Viscosity vs Temperature

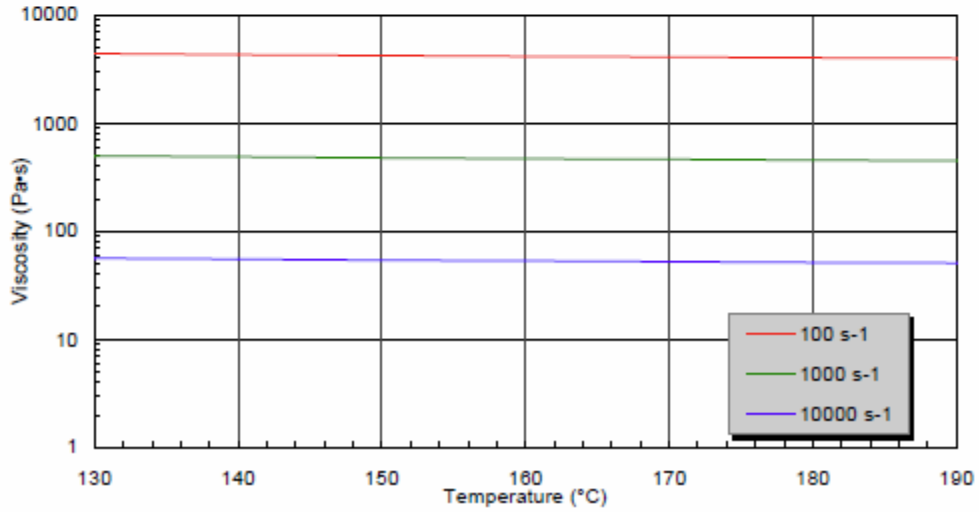

Specific Heat

Method	Based on ASTM E1269: 2005 Determining Specific Heat Capacity by Differential Scanning Calorimetry	
Instrument	Perkin Elmer DSC7	
Specimen	type	pellets
	drying	none
	other preparation	cut from pellet
Parameters	purge gas	N2
	purge gas purity	99.99 %
	purge gas rate	25 ml/min
	cooling rate	20 °C/min
	initial temperature	180 °C
	final temperature	-10 °C
	equilibration times	4 min
	sample weight	8.71 mg
	sample pans	Al, volatile
Calibration Standards	temperature	In, Zn
	heat flow	In
	specific heat	sapphire

Heat capacity is a thermodynamic quantity and is a measure of the amount of heat retained by the material. The DSC can measure this property over a range of temperatures and in both solid and melt states.

Notes: An additional peak was observed in the 60° to 90°C range.

Transition Analysis

extrapolated onset	53 °C
peak	49 °C
extrapolated end	40 °C

Specific Heat Data

Temp °C	Cp J/kg•K
170	1413
111	1315
58	1274
49	2915
30	1472
20	1186
0	998

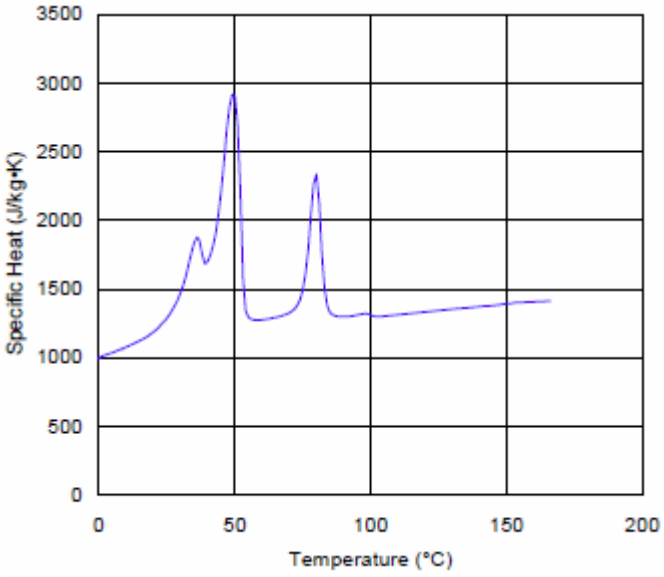

Thermal Conductivity

Method	ASTM D 5930: 2001 Thermal Conductivity of Plastics by Means of a Transient Line-Source Technique	
Instrument	K-System II Thermal Conductivity System	
Specimen	type	pellets
	drying	none
	other preparation	none
Parameters	calibration material	60,000 cstk PDMS
	probe constant	0.796
	probe length	50 mm
	loading temperature	180 °C
	initial temperature	180 °C
	final temperature	30 °C
	probe voltage	3.5 V
	acquisition time	45 s
Uncertainty	per standard	

Thermal conductivity is a measure of the rate of heat conduction of the material. It is a critical property for heat transfer calculations. The line-source method measures thermal conductivity in both melt and solid state.

Thermal Conductivity Data

Temp °C	k W/m•K
186	3.270
166	2.090
146	3.383
126	2.474
106	2.196
86	3.251
66	3.062
45	3.092

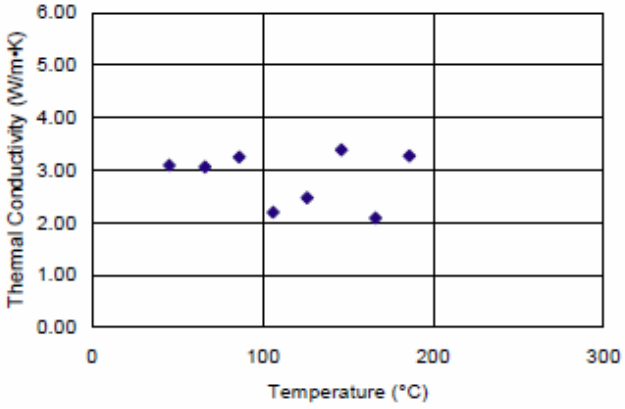

PVT

Method	Non-standard. Pressure-specific volume-temperature measurements using high-pressure dilatometry	
Instrument	Gnomix PVT apparatus	
Specimen	type	plaque
	drying	none
	other preparation	cut from plaque
Parameters	solid density method	ASTM D792
	immersion liquid	water
	PVT confining fluid	Mercury
	max temperature	180 °C
	measurement type	isothermal heating scan
	heating rate	approx. 3 °C/min

PVT data are equation-of-state thermodynamic properties that describe the compressibility and volumetric expansion of the material. Dilatometry measures the change in volume of a specimen subjected to different temperatures and pressures.

Pressure-Volume-Temperature Data

Specific Volume cm3/g

Temp	Pressure MPa					
°C	0	40	80	120	160	200
27	0.4326	0.4296	0.4274	0.4256	0.4237	0.4227
36	0.4329	0.4302	0.4279	0.4256	0.4241	0.4228
48	0.4360	0.4317	0.4287	0.4266	0.4246	0.4236
59	0.4411	0.4359	0.4310	0.4282	0.4256	0.4239
76	0.4484	0.4429	0.4377	0.4321	0.4287	0.4260
92	0.4503	0.4442	0.4402	0.4369	0.4344	0.4302
108	0.4536	0.4463	0.4417	0.4379	0.4354	0.4327
123	0.4565	0.4490	0.4439	0.4398	0.4369	0.4345
138	0.4609	0.4520	0.4463	0.4420	0.4385	0.4356
153	0.4638	0.4542	0.4486	0.4443	0.4411	0.4383
168	0.4654	0.4565	0.4502	0.4460	0.4423	0.4396
183	0.4687	0.4580	0.4519	0.4471	0.4437	0.4406

Modified Two-Domain Tait Model (C-MOLD, Moldflow)

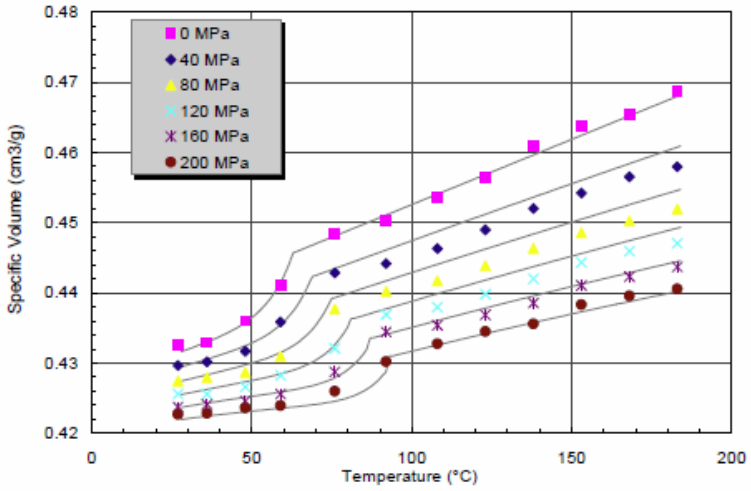

Coefficients	
b5	6.30E+01
b6	1.45E-01
b1m	4.457E-01
b2m	1.861E-04
b3m	3.430E+02
b4m	4.028E-03
b1s	4.368E-01
b2s	1.494E-04
b3s	5.000E+02
b4s	1.000E-02
b7	8.94E-03
b8	1.306E-01
b9	2.221E-02

Modified Two-Domain Tait Equation

$$v(T,p)=v_0(T)\left(1-C\ln\left(1+\frac{p}{B(T)}\right)\right)+v_t(T,p), T_t(p)=b_5+b_6p$$

for $T>T_t(p): v_0(T)=b_{1m}+b_{2m}(T-b_5),\ B(T)=b_{3m}\exp(-b_{4m}(T-b_5)),\ v_t(T,p)=0$

for $T<T_t(p): v_0(T)=b_{1s}+b_{2s}(T-b_5),\ B(T)=b_{3s}\exp(-b_{4s}(T-b_5)),\ v_t(T,p)=b_7\exp(b_8(T-b_5)-b_9p)$

Model Terms	Units
specific volume, v	cm3/g
pressure, P	MPa
temperature, T	°C

No-Flow Temperature

Method	non-standard Moldflow specification; no-flow temperature defined by extrudate flow < 2 mm/min	
Instrument	Goettfert Capillary Rheometer	
Specimen	type	pellets
	drying	none
	other preparation	none
Parameters	equivalent load	172 kg
	barrel diameter	12 mm
	initial pressure	0 MPa
	test temperature	140 °C
	dwell time	6 min
	die inner diameter	1 mm
	die length	20 mm
	die entry angle	180 °

The no-flow temperature provides a measure of the solidification temperature of the melt. During the test, a molten specimen is cooled under constant load; the no-flow temperature is one at which flow ceases to occur.

Results

No-Flow Temperature	58 °C

Appendix A3: Properties of Multi-Component Binder Mixture

Table A.3 Feedstock composition of µ-n AlN Feedstock

Materials	Weight (%)
Paraffin wax	50
Propylene	35
Stearic acid	5
Low density polyethylene – g – maleic anhydride	10

Client	Valmikanathan Onbattuvelli
Company	Oregon State University
Address	Hall□
	Corvallis, OR
	United States
Sample Received	3/26/2009
Sample Source	Oregon State University
Report Prepared	4/9/2009
Prepared By	
Title	Engineer
Issued By	
Title	Operations Manager

DatapointLabs is accredited by the American Association for Laboratory Accreditation (A2LA Certificate # 1242.01), and maintains a quality system in accordance with ISO/IEC 17025. Any opinions or interpretations expressed in this report are outside the scope of the accreditation.

The results in this report relate only to the items tested. This report shall not be reproduced except in full without the written approval of DatapointLabs.

DatapointLabs cannot be held liable under any circumstances for damages arising out of the use of this information or for claims in excess of that originally paid for the testing. DatapointLabs disclaims all other warranties, either express or implied, including implied warranties of merchantability or fitness for a particular purpose.

DatapointLabs

http://www.datapointlabs.com

95 Brown Road, Ithaca, NY 14850
Phone: 607-266-0405 Fax: 607-266-0168
Toll-Free (U.S.): 1-888-328-2422

This data is available in True Digital format

dds matereality
www.matereality.com

C-MOLD/Moldflow *TestPak*™ Results

< 14979.21000.udb

Analysis	Property & T-CODE	Value	Units
Filling & Cooling	Cross/WLF Model (01313):		
	n	0.40120	
	τ^*	7.935E+02	Pa
	D1	4.293E+23	Pa•s
	D2	333	K
	D3	0	K/Pa
	A1	78.13	
	A2	51.60	K
	Juncture Loss Constants (01360):		
	C1		Pa^(1-C2)
	C2		
	Melt Density (01000)	705	kg/m^3
	Melt Specific Heat (01100)	2589	J/kg•K
	Melt Thermal Conductivity (01200)	0.159	W/m•K
	Transition Temperature (01500)	372	K
	Specific Heat Table (01101)	See Page 7	
	Thermal Conductivity Table (01201)	See Page 8	
Post-Filling	Two-Domain Tait PVT Model (01004):		
	b5	3.360E+02	K
	b6	1.465E-07	K/Pa
	b1m	1.255E-03	m^3/kg
	b2m	1.344E-06	$m^3/kg•K$
	b3m	1.256E+08	Pa
	b4m	5.867E-03	1/K
	b1s	1.170E-03	m^3/kg
	b2s	8.568E-07	$m^3/kg•K$
	b3s	2.396E+08	Pa
	b4s	4.155E-03	1/K
	b7	8.458E-05	m^3/kg
	b8	6.688E-02	1/K
	b9	1.387E-08	1/Pa
Shrink / Warp - Uncorrected Stress	Anisotropic Mechanical Properties (01602)		
	Modulus E_1 (flow direction)		MPa
	Modulus E_2 (transverse direction)		MPa
	Poisson's ratio ν_{12}		
	Poisson's ratio ν_{23}		
	Shear Modulus G		MPa
	Anisotropic Thermal Expansion (01702)		
	CLTE α_1 (flow direction)		x 10E-6/°C
	CLTE α_2 (transverse direction)		x 10E-6/°C

Viscosity

Method	ASTM D 3835: 2008 Determination of Properties of Polymeric Materials by Means of a Capillary Rheometer	
Instrument	Instron 5582 Electomechanical UTM	
Specimen	type	powder
	drying	none
	other preparation	none
Parameters	initial pressure	0 MPa
	barrel diameter	12 mm
	die entry angle	180 °
	die inner diameter	1 mm
	die length	20 mm
	preheating time	6 min
Data Correction		
Precision	temperature	+/- 0.1 °C
	die inner diameter	+/- 0.0069 mm
	die length	+/- 0.025 mm
Uncertainty	per standard	

Notes: This material had totally unstable pressures throughout all testing.

Polymer rheology characterizes the complex flow behavior of plastics. A capillary rheometer measures viscosity as a function of temperature and shear rate. The Goettfert rheometer utilizes direct measurement of melt pressures through a side mounted pressure transducer.

Data are modeled using empirical or semi-empirical equations.

Viscosity Data

140 °C		*150 °C*		*160 °C*	
Shear Rate s^{-1}	**Viscosity Pa·s**	**Shear Rate s^{-1}**	**Viscosity Pa·s**	**Shear Rate s^{-1}**	**Viscosity Pa·s**
80	46.66	80	25.23	80	7.62
160	38.08	160	22.85	160	5.71
400	28.24	400	12.98	400	4.87
800	19.47	800	8.73	800	1.87
		1600	4.10		

Cross/WLF Model (C-MOLD, Moldflow)

$$\eta(T,\dot{\gamma}) = \frac{\eta_0(T)}{1+\left(\frac{\eta_0\dot{\gamma}}{\tau^*}\right)^{1-n}}, where$$

$$\eta_0(T) = D_1 \exp\left(-\frac{A_1(T-D_2)}{A_2+(T-D_2)}\right)$$

Coefficients (SI units)

n	0.40120
τ*	793.461
D1	4.29E+23
D2	333
A1	78.13
A2	51.6

Viscosity vs Shear Rate

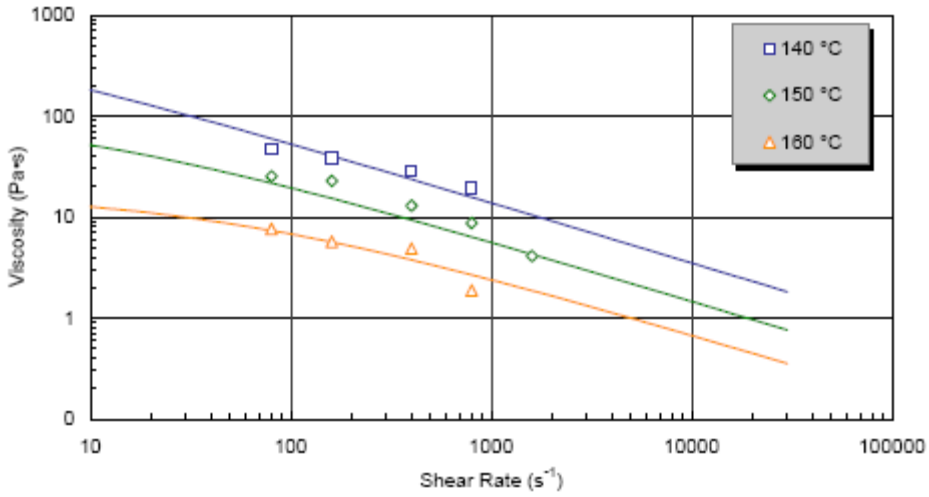

Viscosity vs Temperature

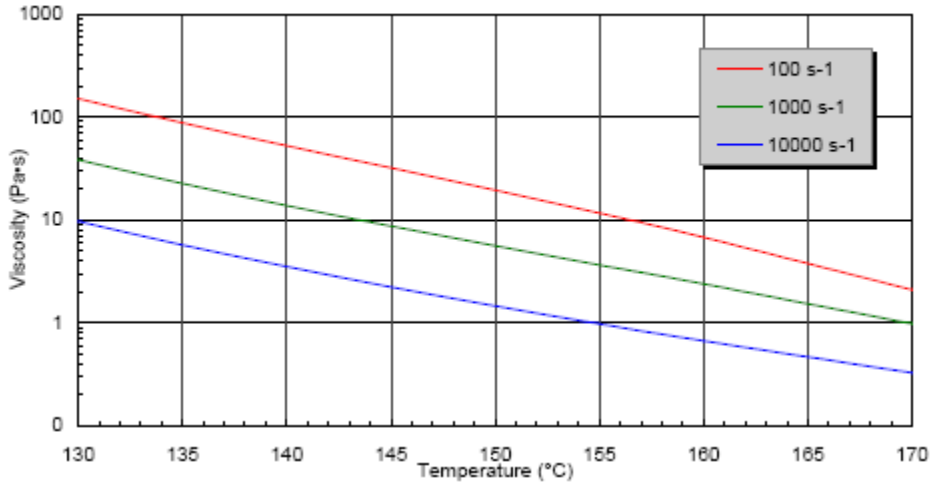

Specific Heat

Method	Based on ASTM E1269: 2005 Determining Specific Heat Capacity by Differential Scanning Calorimetry	
Instrument	Perkin Elmer DSC7	
Specimen	type	pellets
	drying	none
	other preparation	cut from pellet
Parameters	purge gas	N2
	purge gas purity	99.99 %
	purge gas rate	25 ml/min
	cooling rate	20 °C/min
	initial temperature	180 °C
	final temperature	0 °C
	equilibration times	4 min
	sample weight	5.63 mg
	sample pans	Al, volatile
Calibration Standards	temperature	In, Zn
	heat flow	In
	specific heat	sapphire

Heat capacity is a thermodynamic quantity and is a measure of the amount of heat retained by the material. The DSC can measure this property over a range of temperatures and in both solid and melt states.

Transition Analysis

extrapolated onset	99 °C
peak	95 °C
extrapolated end	89 °C

Specific Heat Data

Temp °C	Cp J/kg•K
170	2598
134	2473
104	2371
95	9286
79	3505
49	4894
10	2077

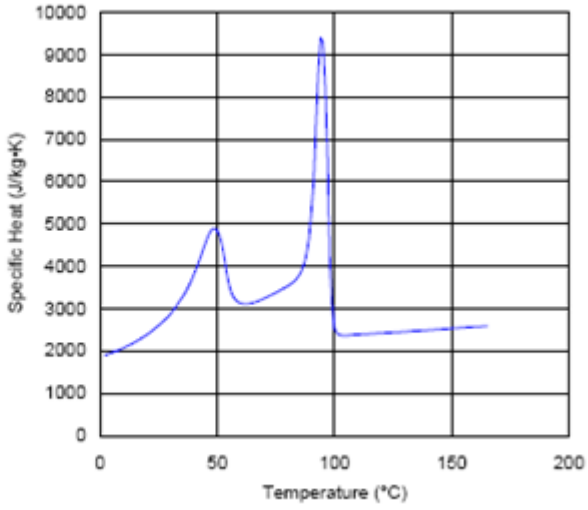

Thermal Conductivity

Method	ASTM D 5930: 2001 Thermal Conductivity of Plastics by Means of a Transient Line-Source Technique	
Instrument	Instron 8872 Servohydraulic UTM	
Specimen	type	powder
	drying	none
	other preparation	none
Parameters	calibration material	60,000 cstk PDMS
	probe constant	0.743
	probe length	50 mm
	loading temperature	160 °C
	initial temperature	180 °C
	final temperature	30 °C
	probe voltage	4 V
	acquisition time	45 s
Uncertainty	per standard	

Thermal conductivity is a measure of the rate of heat conduction of the material. It is a critical property for heat transfer calculations. The line-source method measures thermal conductivity in both melt and solid state.

Thermal Conductivity Data

Temp °C	k W/m•K
186	0.158
167	0.160
147	0.159
128	0.166
108	0.167
87	0.193
67	0.186
47	0.192
41	0.192

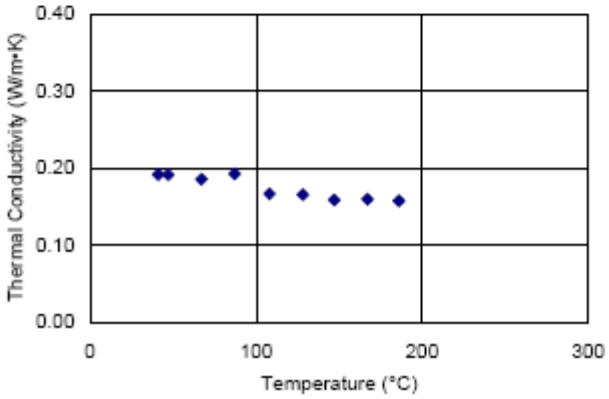

PVT

Method	Non-standard. Pressure-specific volume-temperature measurements using high-pressure dilatometry	
Instrument	Gnomix PVT apparatus	
Specimen	type	pellets
	drying	none
	other preparation	see note below
Parameters	solid density method	ASTM D792
	immersion liquid	water
	pvT confining fluid	mercury
	max temperature	180 °C
	measurement type	isothermal heating scan
	heating rate	approx. 3 °C/min

Notes: Specimen was cut from a plug that was manufactured by Datapoint Labs from pellets suplied by client.

PVT data are equation-of-state thermodynamic properties that describe the compressibility and volumetric expansion of the material. Dilatometry measures the change in volume of a specimen subjected to different temperatures and pressures.

Pressure-Volume-Temperature Data

Specific Volume cm3/g

Temp	Pressure MPa					
°C	0	40	80	120	160	200
33	1.1521	1.1346	1.1207	1.1084	1.0980	1.0890
42	1.1640	1.1428	1.1261	1.1136	1.1024	1.0934
53	1.1929	1.1678	1.1394	1.1221	1.1090	1.0979
61	1.2467	1.2011	1.1678	1.1415	1.1194	1.1049
77	1.2733	1.2418	1.2174	1.1819	1.1527	1.1301
92	1.2897	1.2549	1.2277	1.2074	1.1898	1.1645
107	1.3088	1.2682	1.2393	1.2169	1.1981	1.1817
122	1.3324	1.2861	1.2534	1.2283	1.2079	1.1911
137	1.3615	1.3101	1.2745	1.2456	1.2229	1.2025
152	1.3805	1.3251	1.2882	1.2607	1.2385	1.2194
168	1.3975	1.3378	1.2983	1.2693	1.2484	1.2270
184	1.4138	1.3497	1.3085	1.2783	1.2542	1.2336

Modified Two-Domain Tait Model (C-MOLD, Moldflow)

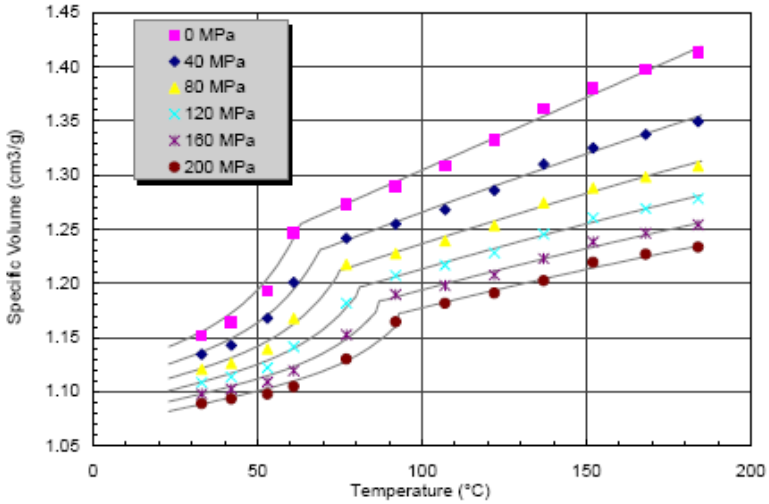

Coefficients	
b5	6.30E+01
b6	1.47E-01
b1m	1.255E+00
b2m	1.344E-03
b3m	1.256E+02
b4m	5.867E-03
b1s	1.170E+00
b2s	8.568E-04
b3s	2.396E+02
b4s	4.155E-03
b7	8.46E-02
b8	6.688E-02
b9	1.387E-02

Modified Two-Domain Tait Equation

$$v(T,p) = v_0(T)\left(1 - C\ln\left(1 + \frac{p}{B(T)}\right)\right) + v_t(T,p), T_t(p) = b_5 + b_6 p$$

for $T > T_t(p)$: $v_0(T) = b_{1m} + b_{2m}(T - b_5)$, $B(T) = b_{3m}\exp(-b_{4m}(T - b_5))$, $v_t(T,p) = 0$

for $T < T_t(p)$: $v_0(T) = b_{1s} + b_{2s}(T - b_5)$, $B(T) = b_{3s}\exp(-b_{4s}(T - b_5))$, $v_t(T,p) = b_7\exp(b_8(T - b_5) - b_9 p)$

Model Terms	Units
specific volume, v	cm3/g
pressure, P	MPa
temperature, T	°C

No-Flow Temperature

Method	non-standard Moldflow specification; no-flow temperature defined by extrudate flow < 2 mm/min	
Instrument	Goettfert Capillary Rheometer	
Specimen	type	pellets
	drying	none
	other preparation	none
Parameters	equivalent load	172 kg
	barrel diameter	12 mm
	initial pressure	0 MPa
	test temperature	140 °C
	dwell time	6 min
	die inner diameter	1 mm
	die length	20 mm
	die entry angle	180 °

The no-flow temperature provides a measure of the solidification temperature of the melt. During the test, a molten specimen is cooled under constant load; the no-flow temperature is one at which flow ceases to occur.

NOTE: No Flow temperature is taken from DSC data.

Results

No-Flow Temperature	47 °C

Appendix B: Procedures for Viscosity Calculations

The Cross-WLF model **Equation B.1** was used to calculate viscosity values at different shear rates and four different temperatures using the experimentally* available data for Cross-WLF coefficients (**Table B.1**) for matrix and 0.52 volume fractions AlN.

$$\eta = \frac{\eta_0}{1 + \left(\frac{\eta_0 \gamma}{\tau^*}\right)^{1-n}} \qquad \text{(B.1)}$$

where, η is the melt viscosity (Pa-s), η_0 is the zero shear viscosity, γ is the shear rate (1/s), τ^* is the critical stress level at the transition to shear thinning, and n is the power law index in the high shear rate regime.

Table B.1: Experimental values of Cross-WLF coefficients

	binder [b]	0.52 volume fraction of AlN [c]
n	0.40	0.38
tau	793.46	117.77
D1	4.29E+23	8.78E+10
D2	333.00	263.15
A1	78.13	14.24
A2	51.60	51.60
T*=D2		

Using the data given in **Table B.1** zero shear viscosity η_0 was calculated for both binder and 0.52 volume fraction of AlN at temperatures of 413, 419.5, 426 and 433 K. This was calculated using **Equation B.2**.

$$\eta_0 = D_1 exp\left[-\frac{A_1(T - T^*)}{A_2 + (T - T^*)}\right] \qquad \text{(B.2)}$$

where, T is the temperature (K). T^*, D_1 and A_1, are WLF coefficients. Using **Equation B.2** η_o values were calculated at 413, 419.5, 426, and 433 K at different shear rates for matrix and 0.52 volume fractions AlN. An illustration for this calculation is shown in **Table B.2:**

(Experimental data was extrapolated to reach zero shear viscosities)*

Table B.2: Calculation of zero shear viscosity for matrix and 0.52 volume fraction of AlN at different shear rates.

viscosity, Pa·s	binder [b]	0.52 volume fraction of AlN [c]
temperature, K	η_o, Pa·s	η_o, Pa·s
413	1013	2209728
419.5	239	1971689
426	64	1771490
433	18	1589698

This information was used to calculate viscosity values for binder and 0.52 volume fraction AlN at different shear rates ranging 1 x 10^{-10} to 7.5 x 10^{4}. This was done using **Equations B.1 and B.2.** Viscosity was calculated for four different temperatures 413, 426, 433, nd 433 K. An illustration for calculating viscosity at 413 K for different shear rates is shown in **Table B.3.**

Table B.3: Calculation of viscosity for matrix and 0.52 volume fraction of AlN for different shear rates and at 413 K.

shear rate, s^{-1}	viscosity, Pa·s	
	matrix [m]	0.52 volume fraction of AlN [c]
0.01	943.36	81855.52
0.02	911.30	53871.75
0.50	574.01	7422.34
0.70	523.40	6023.75
0.80	503.17	5544.56
0.90	485.32	5153.55
100.00	52.63	275.29
125.89	46.16	238.54
158.49	40.45	206.69
199.53	35.43	179.10
501.19	20.72	100.96
630.96	18.09	87.48
794.33	15.80	75.80
1000.00	13.79	65.68
1258.93	12.04	56.91
1584.89	10.50	49.31
1995.26	9.16	42.73
2511.89	7.99	37.02
10000.00	3.51	15.67

Further, the simplified Krieger Dougherty model, as given in **Equation B.1**, was used to calculate critical solids loading (ϕ_{max}) for each shear rate between 0.48 to 0.52 volume fractions AlN. A floating ϕ_{max} (maximum packing fraction of the powder) value corresponding to each shear rate given in **Table B.4** was calculated at 413, 419.5, 426, and 433 K.

Table B.4: Calculation of maximum volume fraction for each individual temperature at different shear rates.

shear rate, s^{-1}	**ϕ_{max} at temperature, 413 K**
0.01	0.58
0.02	0.60
0.03	0.61
0.04	0.62
0.05	0.62
0.06	0.63
0.07	0.63
0.08	0.64
0.09	0.64
0.10	0.65
0.20	0.68
0.30	0.70
0.40	0.71
0.50	0.72
1000.00	0.96
1258.93	0.96
1584.89	0.97
1995.26	0.97
2511.89	0.97
3162.28	0.97
3981.07	0.98
5011.87	0.98
6309.57	0.98
7943.28	0.98
10000.00	0.99

Using the floating ϕ_{max} values at different shear rates and temperatures, viscosity (η) values are calculated using **Equation B.3** for 0.48, 0.49, 0.5, 0.51 and 0.52 volume

fractions at the above mentioned temperatures. An illustration of η calculation at 413 K for 0.48 volume fractions AlN is shown in **Table B.5.**

Table B.5: Calculation of viscosity at different shear rates for 413 K using floating ϕ_{max} and **Equation B.1**

volume fraction powder	**0.48**
shear rate, s^{-1}	**viscosity, Pa·s**
0.10	11664.85
0.20	8311.55
0.30	6754.84
0.40	5808.88
0.50	5157.09
0.60	4673.52
0.70	4296.72
0.80	3992.66
0.90	3740.77
100.00	227.92
125.89	197.88
158.49	171.77
251.19	129.38
316.23	112.28
398.11	97.42
501.19	84.52
630.96	73.33
794.33	63.62
1000.00	55.19
1258.93	47.87
1584.89	41.52
1995.26	36.02
2511.89	31.24
3162.28	27.10
3981.07	23.50
5011.87	20.38
6309.57	17.68
7943.28	15.33
10000.00	13.30

In order to calculate Cross-WLF coefficients from the interpolated data as represented in **Table B.5**, a GRG nonlinear solver was used. To begin, viscosities at different shear rates were calculated from **Equation B.1** in an Excel spreadsheet. The zero shear viscosity value was taken as the constant value obtained from the interpolated data while an initial informed guess was done on the Cross-WLF coefficients n and τ*. A square of difference was calculated for viscosity values at each shear rate between the interpolated viscosity and viscosity calculated from **Equation B.1**. The sum of the square of the difference (SSD) was calculated and the GRG nonlinear solver was used to minimize SSD. It was observed that the data provided the best fit in the low shear rate region but deviated in the high shear rate region. To achieve a better fit between the experimental and the calculated data, SSD was calculated for high shear rate region and the solver was used to find the Cross-WLF coefficients n (power law index) and τ* (critical stress level). An illustration of the curve-fitted data is shown in **Figure B.1** and SSD calculation is shown in **Table B.6.**

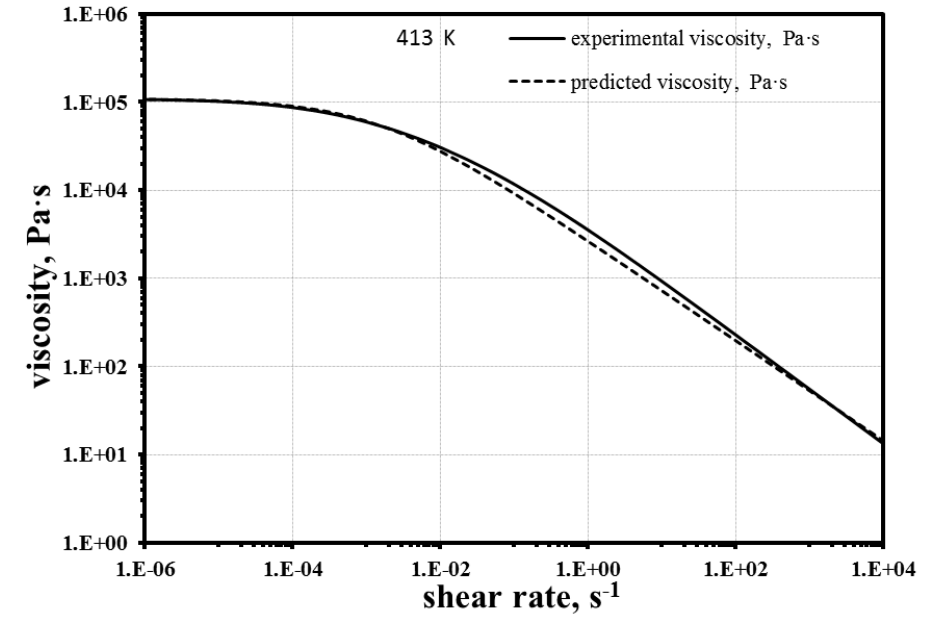

Figure B.1. Comparison of experimental* and predicted values of viscosity as a function of shear rate.

(Experimental data was extrapolated to reach zero shear viscosities)*

Table B.6. Sum of square of difference method for 0.48 volume fractions AlN at 413 K to calculate η_0, n, and τ^*

shear rate, s^{-1}	experimental viscosity, Pa·s	predicted viscosity, Pa·s	difference^2
1E-10	108323.17	108696.78	1.40E+05
2E-10	108319.86	108692.37	1.39E+05
3E-10	108317.15	108688.85	1.38E+05
4E-10	108314.77	108685.82	1.38E+05
5E-10	108312.60	108683.10	1.37E+05
6E-10	108310.60	108680.61	1.37E+05
7E-10	108308.71	108678.29	1.37E+05
8E-10	108306.93	108676.11	1.36E+05
9E-10	108305.23	108674.05	1.36E+05
1E-09	108303.60	108672.08	1.36E+05
2E-09	108289.76	108655.75	1.34E+05
3E-09	108278.42	108642.76	1.33E+05
4E-09	108268.46	108631.55	1.32E+05
7E-09	108243.16	108603.73	1.30E+05
8E-09	108235.71	108595.68	1.30E+05
9E-09	108228.61	108588.06	1.29E+05
1000.00	55.19	53.09	4.40E+00
1258.93	47.87	46.58	1.66E+00
1584.89	41.52	40.87	4.24E-01
1995.26	36.02	35.86	2.39E-02
2511.89	31.24	31.47	5.13E-02
3162.28	27.10	27.61	2.64E-01
3981.07	23.50	24.22	5.24E-01
5011.87	20.38	21.25	7.62E-01
6309.57	17.68	18.65	9.45E-01
7943.28	15.33	16.36	1.06E+00
10000.00	13.30	14.36	1.13E+00
η_0	108705.94	**SSD**	**2.59E+08**
n	0.43	**High shear SSD**	**1.91E+01**
τ^*	161.54		

Use of solver to calculate Cross-WLF coefficients n and τ* is illustrated in the following steps. The step-by-step illustration shown was performed in Microsoft Excel 2010 using a Windows-based computer.

Step 1: Open Microsoft Excel 2010 and click on the "*Data*" tab. In the "Data" tab click the "*Solver*" button. This will open a pop-up window called "*Solver Parameters*" as shown in **Figure B.2.**

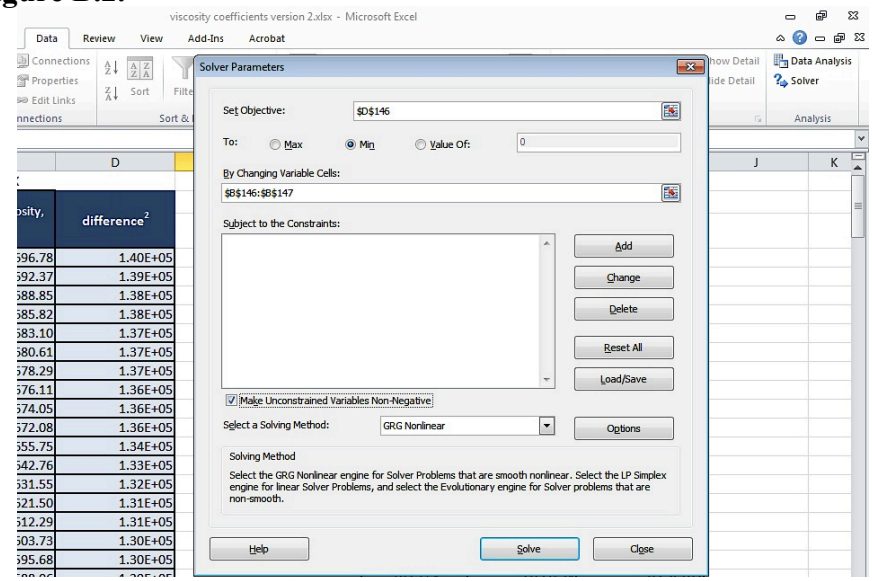

Figure B.2. Solver parameter window in Microsoft Excel 2010.

Step 2: Select the "*high shear SSD*" cell similar to the one given in **Table B.6** in the "*set objective*" space. As the goal is to minimize SSD, click on the circle beside "*Min*" as shown in **Figure B.3.** Select "*GRG Nonlinear*" as the solving method. Further, select the cells referring to Cross-WLF coefficients n and τ* in the "*changing variable cells*" space. n and τ* values are similar to the ones shown in **Table B.6**.

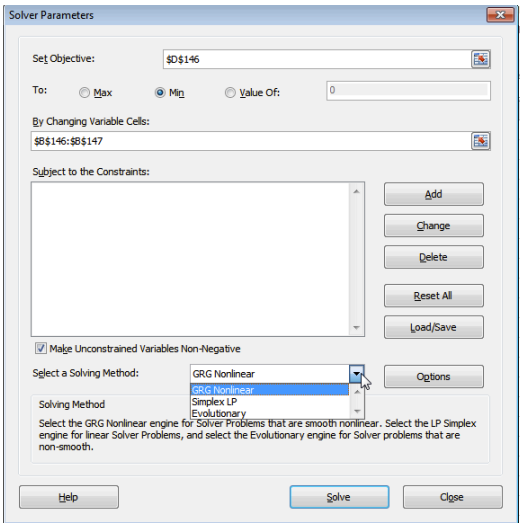

Figure B.3. Selection of solving method and input parameters for calculating n and τ*.

Step 3: In order to reach a suitable convergence value, click on the "*option*" button in the solver parameter window. This will open a small pop-up window as shown in **Figure B.4.** Click on the "*GRG Nonlinear*" tab and set the convergence value to ≥ 1 x 10^{-12}. Finally, click the "*OK*" button.

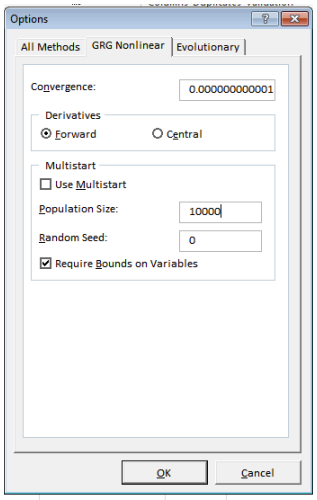

Figure B.4. Set convergence value for GRG Nonlinear method.

Step 4: Click on the "*Solve*" button to obtain new values for n and τ*.

In order to calculate rest of the Cross-WLF coefficients, the same method of minimizing the SSD was used as illustrated in **Steps 1-4.** In this case, the objective cell was taken as SSD and the changing variable cells were taken as D_1 A_1 and T*. For this, the zero shear viscosities were first predicted for four different temperatures 413 K, 419.5 K, 426 K and 433 K using **Equation B.1**. An illustration of the method used to calculate these coefficients is shown in **Table B.7.**

Table B.7. Sum of square of difference method for 0.48 volume fractions AlN at 413 K to calculate D1, A1 and T*

temperature, K	ηo, Pa.s	predicted ηo, Pa.s	difference^2
413	1.09E+05	1.09E+05	1.47E+04
419.5	3.17E+04	3.10E+04	4.37E+05
426	9.49E+03	1.04E+04	7.51E+05
433	2.78E+03	3.68E+03	8.09E+05
D_1	8.73E+10	**SSD**	2.01E+06
A_1	32.13		
T*	375.15		

Calculations represented in **Tables B.2** through **B.7** and **Figures B.1** through **B.4** were performed to calculate Cross-WLF coefficients for volume fractions 0.48, 0.49, 0.5, 0.51 and 0.52 of monomodal AlN-polymer mixtures and also for volume fractions 0.52, 0.54, 0.56, 0.58 and 0.6 of bimodal AlN-polymer mixtures.

Appendix C: Procedures for PVT Calculations

Specific volume was calculated for 0.48, 0.49, 0.5, 0.51 and 0.52 volume fractions AlN for the pressure values of 0, 50, 100, 150 and 200 MPa over a temperature range of 298 to 433 K. **Equation C.1** was used to calculate specific volume.

$$v_c = X_f v_f + v_m(1 - X_f) \qquad \text{(C.1)}$$

An illustration of the specific volume calculations is shown in **Table C.1** and a plot representing these values is as shown in **Figure C.1.**

Table C.1: Specific volume calculations for different solids loading at 50 MPa pressure.

volume fraction powder	0	0.48	0.49	0.5	0.51	0.52	1
temperature [K]	specific volume [m^3/kg]	specific volume [m^3/kg]	specific volume [m^3/kg]	specific volume [m^3/kg]	specific volume [m^3/kg]	specific volume [m^3/kg]	specific volume [m^3/kg]
	AlN (binder)	AlN	AlN	AlN	AlN	AlN	AlN (filler)
298.00	1.12E-03	4.82E-04	4.77E-04	4.72E-04	4.67E-04	4.62E-04	3.20E-04
300.76	1.13E-03	4.82E-04	4.77E-04	4.72E-04	4.67E-04	4.62E-04	3.19E-04
303.51	1.13E-03	4.83E-04	4.78E-04	4.73E-04	4.68E-04	4.63E-04	3.19E-04
306.27	1.13E-03	4.83E-04	4.78E-04	4.73E-04	4.68E-04	4.63E-04	3.18E-04
309.02	1.14E-03	4.84E-04	4.78E-04	4.73E-04	4.68E-04	4.64E-04	3.18E-04
333.82	1.20E-03	4.94E-04	4.89E-04	4.83E-04	4.78E-04	4.72E-04	3.15E-04
336.57	1.22E-03	4.97E-04	4.92E-04	4.86E-04	4.80E-04	4.75E-04	3.15E-04
339.33	1.23E-03	5.01E-04	4.95E-04	4.90E-04	4.84E-04	4.79E-04	3.17E-04
342.08	1.23E-03	5.02E-04	4.96E-04	4.90E-04	4.85E-04	4.79E-04	3.17E-04
344.84	1.23E-03	5.03E-04	4.97E-04	4.91E-04	4.86E-04	4.80E-04	3.18E-04
421.98	1.33E-03	5.24E-04	5.18E-04	5.12E-04	5.06E-04	5.00E-04	3.22E-04
424.74	1.33E-03	5.25E-04	5.19E-04	5.12E-04	5.06E-04	5.00E-04	3.22E-04
427.49	1.33E-03	5.26E-04	5.19E-04	5.13E-04	5.07E-04	5.01E-04	3.22E-04
430.25	1.34E-03	5.27E-04	5.20E-04	5.14E-04	5.08E-04	5.02E-04	3.22E-04
433.00	1.34E-03	5.27E-04	5.21E-04	5.15E-04	5.08E-04	5.02E-04	3.22E-04

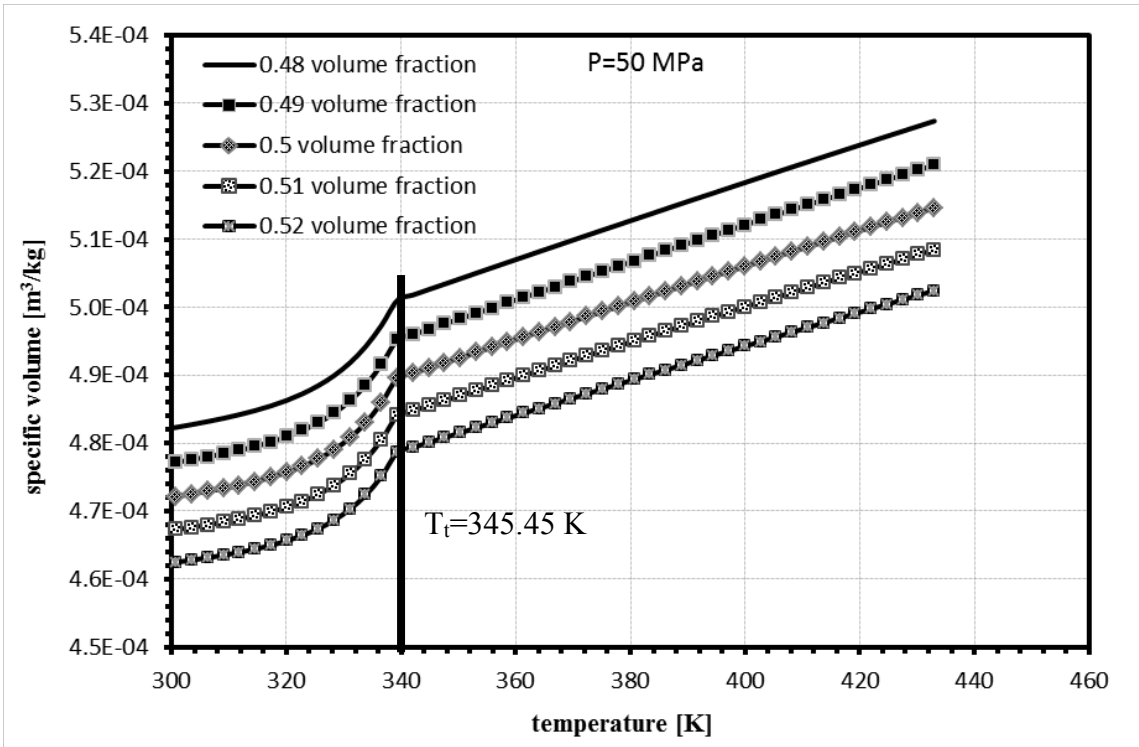

Figure C.1. Specific volume as a function of temperature at 50 MPa pressure.

In order to calculate the dual domain constants, the sum of the square of the difference (SSD) for specific volumes calculated for 0.48 to 0.52 volume fractions of AlN was calculated and a GRG nonlinear solver was used to minimize SSD value. The Dual-Domain Tait model used for predicting specific volumes is shown in **Equations C.2 - 6C.4.**

$$\upsilon(T,p) = \upsilon_o(T)\left[1 - Cln\left(1 + \frac{p}{B(T)}\right) + \upsilon_t(T,p)\right] \quad \text{(C.2)}$$

where, υ (T,p) is the specific volume at a given temperature and pressure, υ_o is the specific volume at zero gauge pressure, T is temperature in K, p is pressure in Pa, and C is a constant assumed as 0.0894. The parameter, B, accounts for the pressure sensitivity of the material and is separately defined for the solid and melt regions. For the upper bound [18] when $T > T_t$ (volumetric transition temperature), B is given by **Equation C.3:**

$$\upsilon_o = b_{1m} + b_{2m}(T - b_5)B(T) = b_{3m}e^{[-b_{4m}(T-b_5)]}\upsilon_t(T,p) = 0 \quad \text{(C.3)}$$

where, b_{1m}, b_{2m}, b_{3m}, b_{4m}, and b_5 are curve-fitted coefficients. For the lower bound, when $T < T_t$, the parameter, B, is given by **Equation C.4:**

$$\upsilon_o = b_{1s} + b_{2s}(T - b_5)B(T) = b_{2s}e^{[-b_{4s}(T-b_5]}\upsilon_t(T,p) = b_7 e^{[b_8(T-b_5)-(b_9 p)]} \quad \text{(C.4)}$$

where, b_{1s}, b_{2s}, b_{3s}, b_{4s}, b_5, b_7, b_8, and b_9 are curve-fitted coefficients. The dependence of the volumetric transition temperature, T_t, on pressure can be given by $T_t(p) = b_5 + b_6(p)$, where b_5 and b_6 are curve-fitted coefficients.

Calculation of Dual-Domain Tait constants was done in four stages. In the first stage, constants b_5 and b_6 were calculated by plotting a graph of transition temperature (T_t) as a function of pressure. T_t value is read off the plot as shown in **Figure C.2.** A linear curve-fitting step was done on intermediate T_t values and the values of b_5 and b_6 were determined. This is shown in **Figure 6.6.**

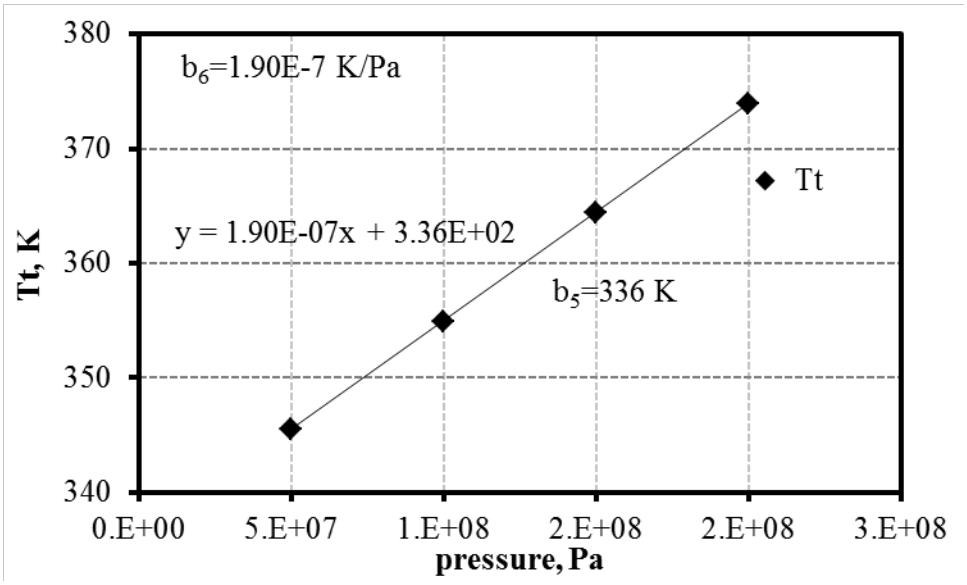

Figure C.2. Volumetric transition temperature as a function of pressure.

In stage two of the calculations, constants b_{1s}, b_{2s}, and b_{1m}, b_{2m}, were calculated by reading the values of the plot as shown in **Figure C.3.** Using informed guesses, the remaining set of Tait constants were assumed. Using **Equations C.4-C.6** in an Excel

spreadsheet, the specific volume was predicted for temperatures ranging from 298 to 433 K.

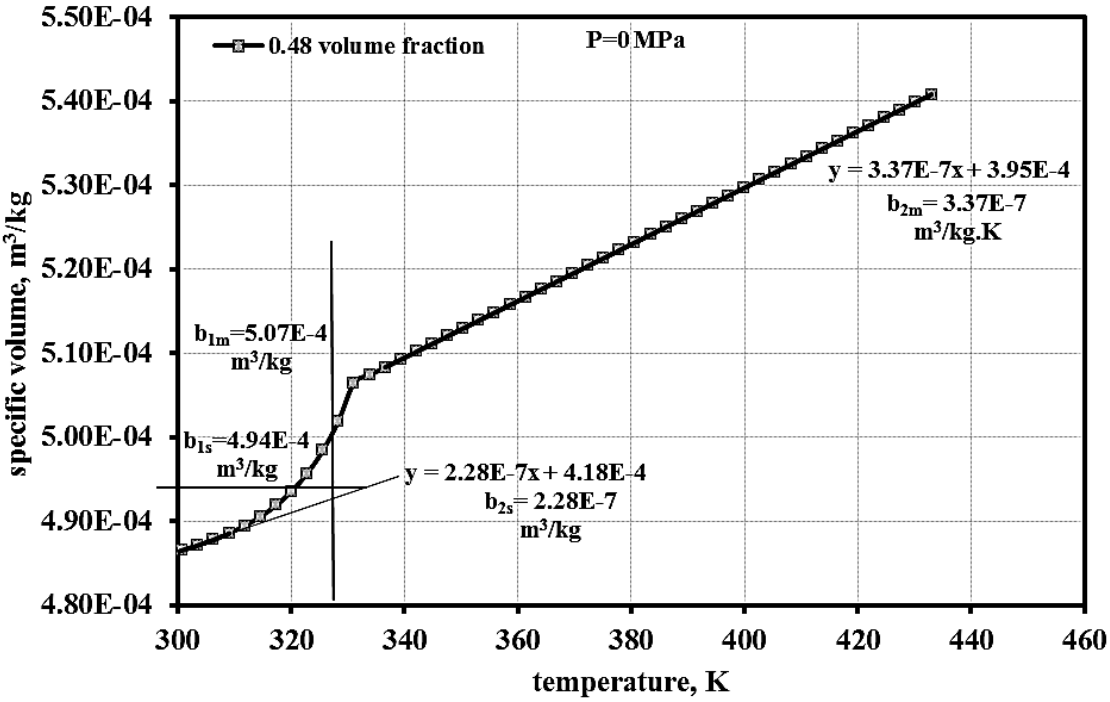

Figure C.3. Specific volume as a function of temperature for 0.48 volume fraction AlN at 0 MPa pressure.

In stage three of the calculations, the SSD that was calculated for the first domain was used to calculate Tait constants b_{3s}, b_{4s}, b_7, b_8, and b_9. In order to do this, the GRG nonlinear solver was used to minimize SSD and get a better fit. In the final stage of calculations, the Tait constants b_{3m} and b_{4m} pertaining to second domain were calculated using GRG nonlinear solver which minimized SSD to obtain a better fit of experimental and predicted values. An illustration of SSD calculation is as shown in **Table C.2.**

The use of the solver to calculate the Dual-Domain Tait constants b_{3m}, b_{4m}, b_{3s}, b_{4s}, b_5, b_7, b_8, and b_9 is illustrated in the following steps. The step-by-step illustration shown below was performed on Microsoft Excel 2010 using a Window-based computer.

Table C.2. Calculation of Tait constants with the use of SSD and a GRG nonlinear solver.

temperature, K	V(T,p), m^3/kg	V(T,p), m^3/kg predicted	$diff^2$	SSD	Tait constants	
298.00	4.86E-04	4.87E-04	5.09E-13	Zone 1	b_5	331
300.76	4.87E-04	4.87E-04	6.24E-13		b_6	1.65E-07
303.51	4.87E-04	4.88E-04	6.72E-13		b_{1m}	5.07E-04
306.27	4.88E-04	4.89E-04	6.18E-13		b_{2m}	3.37E-07
309.02	4.89E-04	4.89E-04	4.42E-13		b_{3m}	2.71E+08
311.78	4.89E-04	4.90E-04	1.77E-13		b_{4m}	4.88E-03
314.53	4.91E-04	4.91E-04	1.72E-16		b_{1s}	4.92E-04
317.29	4.92E-04	4.91E-04	3.87E-13		b_{2s}	1.82E-07
320.04	4.94E-04	4.92E-04	2.45E-12		b_{3s}	5.79E+08
				5.88E-12	b_{4s}	0.00126
336.57	5.08E-04	5.09E-04	3.16E-13	Zone 2	b_7	3.23E-06
339.33	5.09E-04	5.10E-04	3.17E-13		b_8	4.50E-02
342.08	5.10E-04	5.11E-04	3.17E-13		b_9	2.12E-08
344.84	5.11E-04	5.12E-04	3.17E-13			
347.59	5.12E-04	5.13E-04	3.18E-13			
350.35	5.13E-04	5.14E-04	3.19E-13			
413.71	5.34E-04	5.35E-04	3.27E-13			
416.47	5.35E-04	5.36E-04	3.27E-13			
419.22	5.36E-04	5.37E-04	3.28E-13			
421.98	5.37E-04	5.38E-04	3.28E-13			
424.74	5.38E-04	5.39E-04	3.28E-13			
427.49	5.39E-04	5.40E-04	3.29E-13			
430.25	5.40E-04	5.40E-04	3.29E-13			
433.00	5.41E-04	5.41E-04	3.29E-13			
				1.16E-11		

Step 1: Open Microsoft Excel 2010 and click on the "*Data*" tab. In the "Data" tab click the "*Solver*" button that will open a pop-up window called "*Solver Parameters*" as shown in **Figure C.4.**

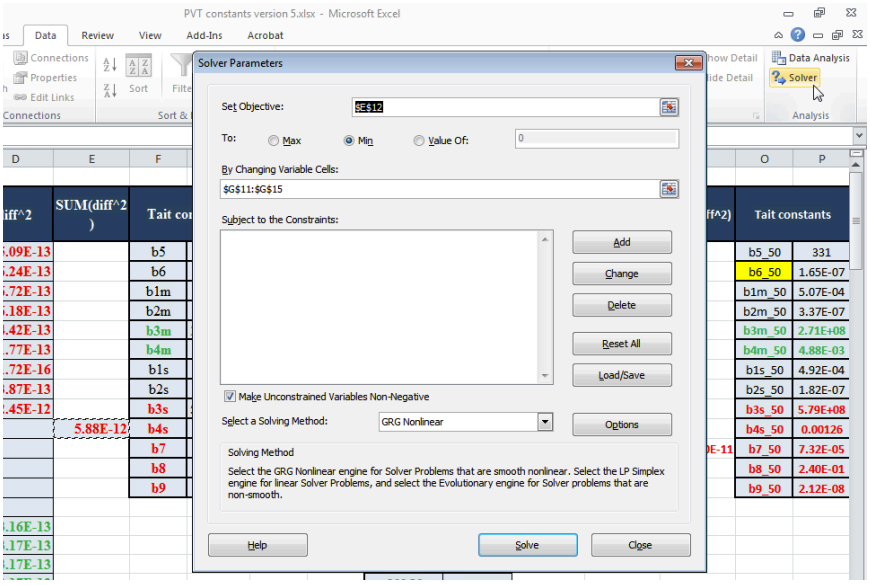

Figure C.4. Solver parameter window in Microsoft Excel 2010.

Step 2: Select the "*SSD*" cell for "Zone 1," similar to the one given in **Table C.3** in the "*set objective*" space, in order to solve for b_{3m}, b_{4m}. Since the goal is to minimize SSD, click on the circle beside "*Min*" as shown in **Figure C.5.** Select "*GRG Nonlinear*" as the solving method. Further select cells referring to Tait constants b_{3m} and b_{4m} in the "*changing variable cell*" space. b_{3m} and b_{4m} values are similar to the ones shown in **Table C.2**.

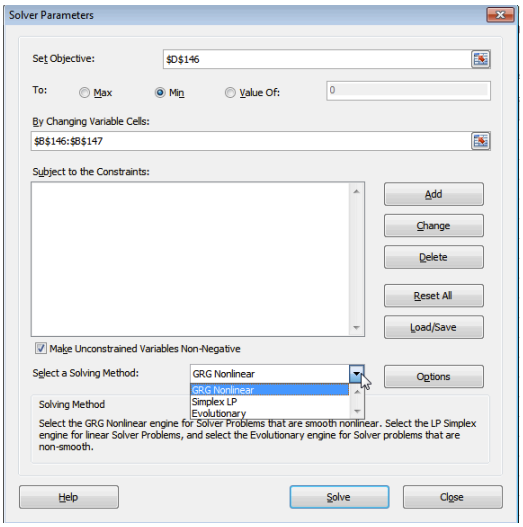

Figure C.5. Selection of solving method and input parameters for calculating b_{3m}, and b_{4m}.

Step 3: In order to reach a suitable convergence value, click on the "*option*" button in the solver parameter window. This will open a small pop-up window as shown in **Figure C.6.** Click on the "*GRG Nonlinear*" tab and set the convergence value to ≥ 1 x 10^{-12}. Finally, click the "*OK*" button.

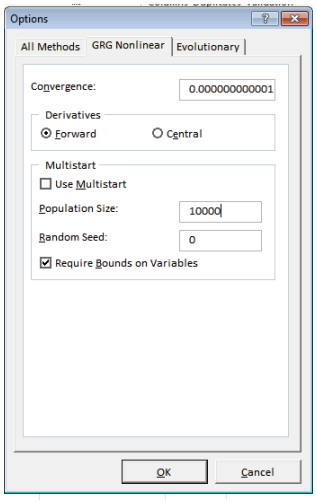

Figure C.6. Set convergence value for GRG Nonlinear method.

Step 4: Click on the "*Solve*" button to get new values for b_{3m}, and b_{4m}.

Step 5: Repeat **Steps 2 to 4** to minimize SSD corresponding to the "Zone 2" b_{3s}, b_{4s}, b_5, b_7, b_8, and b_9 cells as shown in **Table C.2**. These cells are selected in the "*changing variable cell*" space and the "*objective cell*" space is set as "Zone 2" SSD.

Calculations presented in this section were performed to calculate the Dual-Domain Tait constants for volume fractions 0.48, 0.49, 0.5, 0.51 and 0.52 of monomodal AlN-polymer mixtures and also for volume fractions 0.52, 0.54, 0.56, 0.58 and 0.6 of bimodal AlN-polymer mixtures.

Appendix D: Procedures for Calculations of Coefficient of Determination

Coefficient of determination (R^2) values were calculated for density, specific heat, thermal expansion coefficient, thermal conductivity, elastic modulus, viscosity, and specific volume properties. This was done in order to determine how well the experimental data fits with the rule of mixture (ROM) associated to it. ROM's are based on the values of filler and unfilled polymer properties data. In most cases, this data is either taken from handbook or from literature references. Further, when these values are used in ROM's to calculate a R^2 value, an error arises in the value due to prior approximation in the filler and unfilled polymer data. In order to minimize this error and to generate a better fit, a GRG nonlinear solver was used. An illustration to represent this is shown for density in which Rajesh et al [1] used a powder-polymer mixture of polytetrafluoroethylene (PTFE) and rutile (TiO_2). The value of density for PTFE was taken as 2.2 g/cm^3 and that of TiO2 was taken as 4.23 g/cm^3 as the initial estimate. R^2 calculation for density values for Rajesh et al [1] are shown in **Table D.1**

Rajesh et al [1]	density, g/cm^3					
Filler weight fraction Xp	**52**	**57**	**62**	**67**	**average**	
Experimental values Rutile	2.6	2.7	2.8	2.9	**2.75**	
Inverse rule of mixtures Rutile	2.60	2.69	2.79	2.9	**sum**	**R^2**
SSR	0.021	$2.85\text{x}10^{-3}$	$2.13\text{x}10^{-3}$	0.024	**$4.98\text{x}10^{-2}$**	**0.99**
SSE	-0.004	0.003	0.004	-0.003	**$-1.91\text{x}10^{-5}$**	
SSD	1.52E-05	1.15E-05	1.47E-05	1.12E-05	**$5.27\text{x}10^{-5}$**	

Table D.1. Calculation of R^2 for density values using experimental data from Rajesh et al [1]

SSE: Sum of squares of errors; SSR: Regression of sum of squares; SSD: Sum of square of differences.

The inverse rule of mixtures (**Equation D.1**) was used for predicting density values.

$$\frac{1}{\rho_c} = \frac{X_p}{\rho_p} + \frac{X_b}{\rho_b} \qquad \text{(D.1)}$$

where, ρ is the density, X is the mass fraction and the subscripts c, b and p stand for the composite, binder and powder, respectively.

In order to determine R^2, the following approach was used. For each observation, variation in experimental and predicted values can be explained using **Equation D.2:**

$$y = y' + \varepsilon \qquad \text{(D.2)}$$

where y is experimental value, y' is the predicted value and ε is the error associated with the predicted value. Further, a mean of experimental density values was calculated ($\overline{y}$). Then regression of sum of squares (SSR) was calculated at each weight fractions using **Equation D.3**.

$$SSR = \sum(y' - \bar{y})^2 \qquad \text{(D.3)}$$

Further, sum of square of errors (SSE) was calculated using **Equation D.4:**

$$SSE = y - y' \qquad \text{(D.4)}$$

Additionally, sum of square of difference (SSD) was calculated using **Equation D.5:**

$$SSD = \sum(y - y')^2 \qquad \text{(D.5)}$$

Finally, R^2 was calculated using **Equation D.6**:

$$R^2 = 1 - \frac{SSD}{SSR} \qquad \text{(D.6)}$$

Since the R^2 calculated is based upon the values assumed from handbook and literature, a GRG nonlinear solver was used to minimize the difference between experimental and predicted values of density. The step-by-step illustration that follows was performed on Microsoft Excel 2010 using a Windows based computer.

Step 1: Open Microsoft Excel 2010 and click on the "*Data*" tab. In the "Data" tab click the "*Solver*" button that will open a pop-up window called "*Solver Parameters*" as shown in **Figure D.1.**

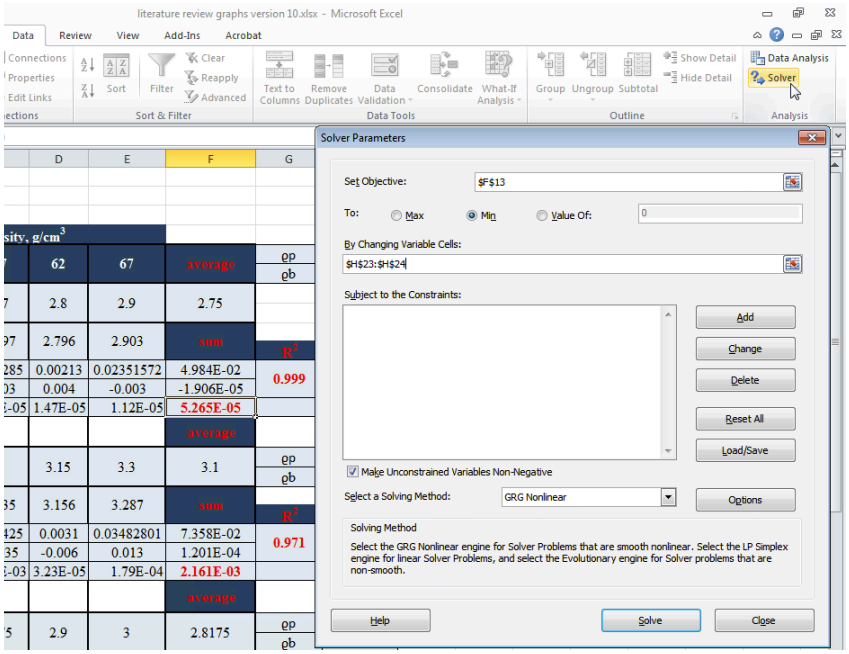

Figure D.1. Solver parameter window in Microsoft Excel 2010.

Step 2: Select the "*SSD*" cell similar to the one given in **Table D.1** in the "*set objective*" space in order to solve for ρ_p and ρ_b. Since the goal is to minimize SSD, click on the circle besides "*Min*" as shown in **Figure D.2.** Select "*GRG Nonlinear*" as the solving method. Further, select cells referring to filler and unfilled binder density, ρ_p and ρ_b, in the "*changing variable cell*" space.

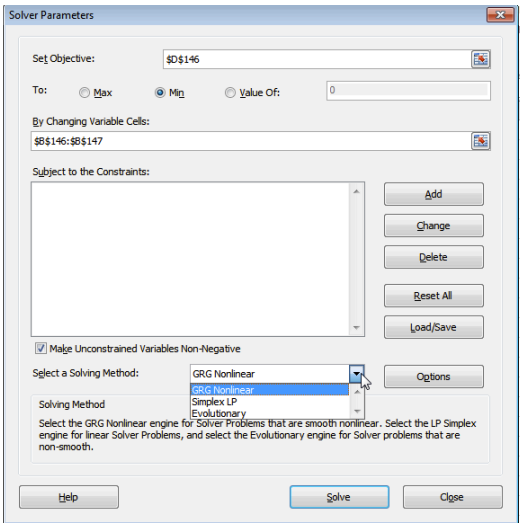

Figure D.2. Selection of solving method and input parameters for calculating ρ_p and ρ_b.

Step 3: In order to reach a suitable convergence value, click on "*option*" button in the solver parameter window. This will open a small pop-up window as shown in **Figure D.3.** Click on the "*GRG Nonlinear*" tab and set the convergence value to $\geq$ 1 x 10^{-12}. Finally click the "*OK*" button.

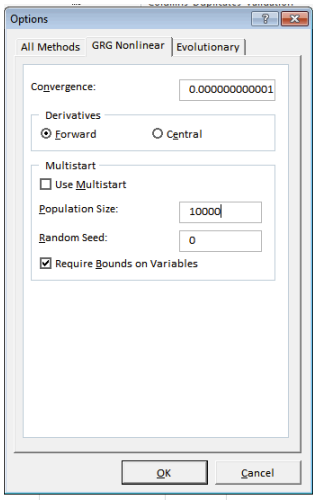

Figure D.3. Set convergence value for GRG Nonlinear method.

Step 4: Click on the "*Solve*" button to get new values for ρ_p and ρ_b.

Calculations presented in **Table D.1** and **Figures D.1** through **D.3** were performed to calculate ρ_p and ρ_b. Similarly **Steps 1** through **4** were used to calculate filler and unfilled binder properties for specific heat, thermal conductivity, thermal expansion coefficient, elastic modulus, viscosity and specific volume with the help of a solver.

Reference:

1. S. Rajesh, K. P. Murali, H. Jantunen, and R. Ratheesh, "The effect of filler on the temperature coefficient of the relative permittivity of PTFE/ceramic composites," Physica B: Condensed Matter, vol. 406, no. 22, pp. 4312–4316, 2011.

Appendix E Procedures for Mold Flow Simulations

Simple heat sink geometries were designed using SolidWorks 2010 software as shown in **Figure E.1.**

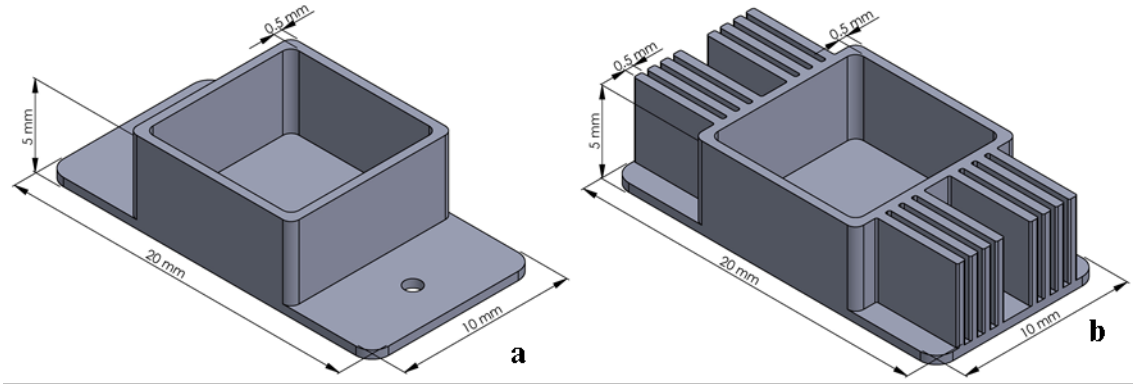

Figure E.1: Mold geometry used in injection molding simulations: a) simple heat-sink substrate without fins, and b) heat sink substrate with fins.

In order to do mold flow simulations on heat sink geometries shown in **Figure E.1**, the geometries were first imported into Autodesk Moldflow Insight 2010 software.

A step-by-step method shown below illustrates how the injection molding simulations were performed.

Step 1: Open Moldflow Insight 2010 software and click on the "*File*" tab. This will open a pop-up window in which the heat sink geometry created using SolidWorks is selected. **Figure E.2** illustrates the appearance of the popup window.

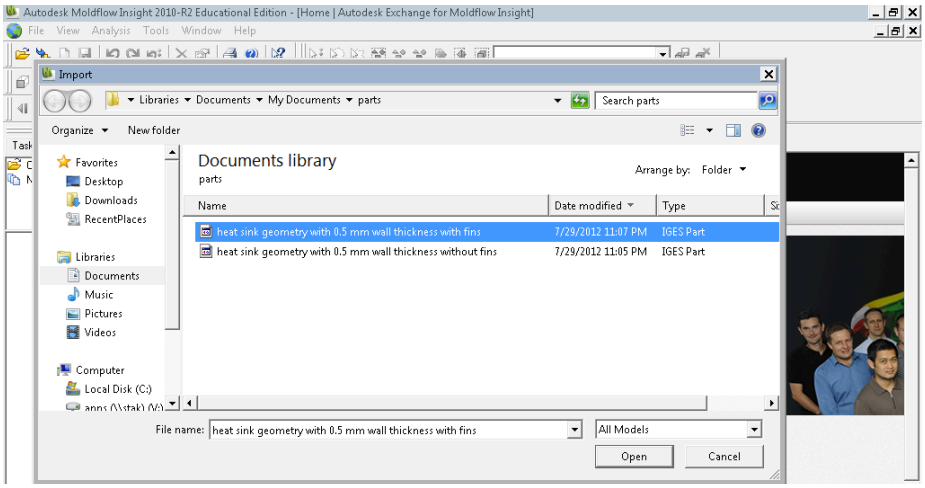

Figure E.2. Selecting heat sink geometry for injection molding simulation

Step 2: After selecting the desired geometry, another window will pop-up in which the meshing type is selected. **Figure E.3** illustrates selection of mesh type window.

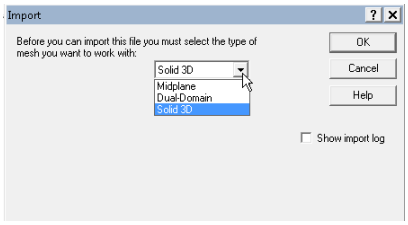

Figure E.3. Selection from the type of meshes types.

Select the "*Solid 3D*" mesh type as it gives the most accurate results and has the widest range of simulation result types. Then press Ok.

Step 3: On selecting "*Solid 3D*," a new widow will pop-up. In this window, select the circle next to "*create new project*"

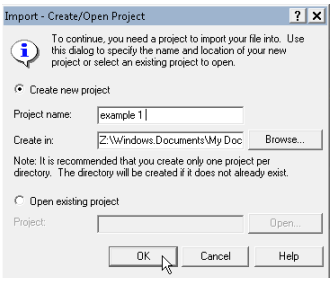

Figure E.4. Creating a new project.

Once a new project file is created, the screen will look like the one shown in **Figure E.5.**

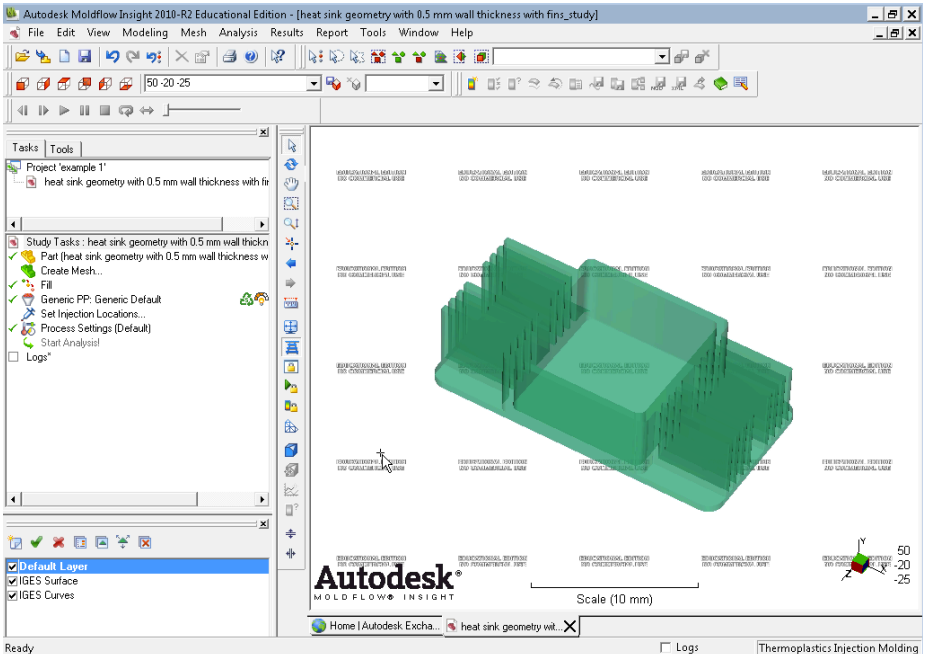

Figure E.5. Typical layout of Moldflow Insight software after creating a new project.

Step 4: In the task pane shown in the left side of **Figure E.5** double click on the "*create mesh*" tab to generate a mesh. An illustration of this is shown in **Figure E.6.**

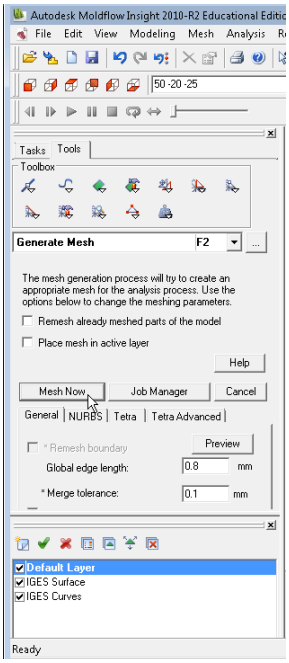

Figure E.6. Generating mesh wizard.

Click on the "*Mesh Now*" button, which will generate a solid 3D mesh on the imported heat sink geometry.

Step 5: Now that the mesh is created, a mesh repair wizard is used in order to remove any mesh errors. Click on the "*Mesh*" tab on the menu bar and then click on the "Mesh Repair Wizard" option. This will open a pop-up widow as shown in **Figure E.7.** Then click on the "*next*" button and in the process fix any errors in the mesh. Finally, press the "*finish*" button.

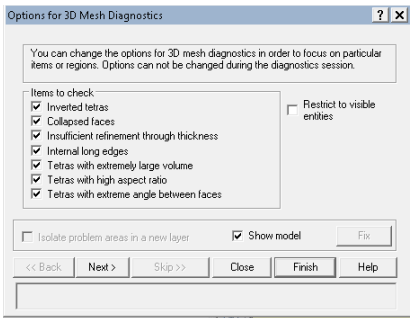

Figure E.7. Mesh repair wizard.

Step 6: Further, in the task pane double click on "*Fill*," which is the default injection molding condition. Then select the "*Fill + Pack*" option from the pop-up window that opens. The selection option for the injection molding condition is as shown in **Figure E.8.** Click Ok and proceed to the next step.

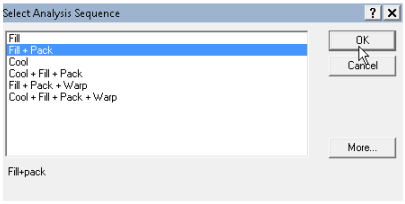

Figure E.8. Selection of analysis sequence.

Step 7: Then select the required material that has to be injection molded by double clicking on the "*Generic PP: Generic Default*" option in the task pane. A window will pop-up where manufacturer of the material needs to be selected and then a specific trade name of the material needs to be selected. An illustration of this selection process is shown in **Figure E.9.** Then click on the "*OK*" button.

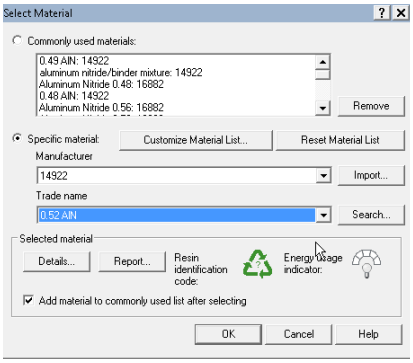

Figure E.9. Material selection process.

Step 8: Double click on "*Set injection location*" from the task pane and place the injection point on the heat sink geometry.

Step 9: Finally, set the process settings by double clicking on the "processing setting" tab on the task pane. This will open up a pop-up window where the mold surface temperature was set at 30 °C and melt temperature was set at 160 °C. Set the rest of the parameters as shown in **Figure E.10** and press the "*OK*" button.

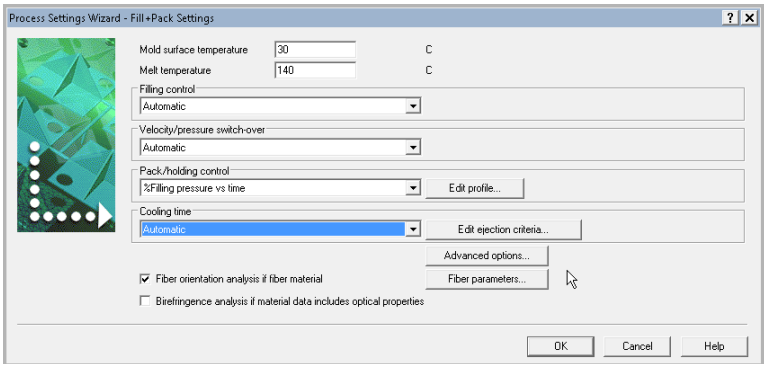

Figure E. 10. Process setting wizard.

Step 10: In the end, double click on the "*start analysis*" tab in the task pane to start the injection molding simulation.

Following steps 1 through 10, injection-molding simulations were performed for volume fractions 0.48, 0.49, 0.5, 0.51 and 0.52 of monomodal AlN-polymer mixtures and also for volume fractions 0.52, 0.54, 0.56, 0.58 and 0.6 of bimodal AlN-polymer mixtures.